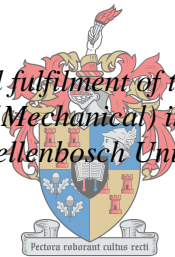


# Theoretical and experimental evaluation of a high temperature reactor (HTR) cavity cooling system (RCCS)

by  
Rikus Swart

*Thesis presented in partial fulfilment of the requirements for the degree of Master of Engineering (Mechanical) in the Faculty of Engineering at Stellenbosch University*



UNIVERSITEIT  
iYUNIVESITHI  
STELLENBOSCH  
UNIVERSITY

100  
1918 · 2018

Supervisor: R.T.D, Robert Thomas Dobson

December 2018

## **DECLARATION**

By submitting this thesis electronically, I declare that the entirety of the work contained therein is my own, original work, that I am the sole author thereof (save to the extent explicitly otherwise stated), that reproduction and publication thereof by Stellenbosch University will not infringe any third party rights and that I have not previously in its entirety or in part submitted it for obtaining any qualification.

R.Swart

Date: December2018

Copyright © 2018 Stellenbosch University  
All rights reserved

## Plagiaatverklaring / *Plagiarism Declaration*

- 1 Plagiaat is die oorneem en gebruik van die idees, materiaal en ander intellektuele eiendom van ander persone asof dit jou eie werk is.  
*Plagiarism is the use of ideas, material and other intellectual property of another's work and to present it as my own.*
- 2 Ek erken dat die pleeg van plagiaat 'n strafbare oortreding is aangesien dit 'n vorm van diefstal is.  
*I agree that plagiarism is a punishable offence because it constitutes theft.*
- 3 Ek verstaan ook dat direkte vertalings plagiaat is.  
I also understand that direct translations are plagiarism.
- 4 Dienooreenkomstig is alle aanhalings en bydraes vanuit enige bron (ingesluit die internet) volledig verwys (erken). Ek erken dat die woordelike aanhaal van teks sonder aanhalingstekens (selfs al word die bron volledig erken) plagiaat is.  
*Accordingly, all quotations and contributions from any source whatsoever (including the internet) have been cited fully. I understand that the reproduction of text without quotation marks (even when the source is cited) is plagiarism.*
- 5 Ek verklaar dat die werk in hierdie skryfstuk vervat, behalwe waar anders aangedui, my eie oorspronklike werk is en dat ek dit nie vantevore in die geheel of gedeeltelik ingehandig het vir bepunting in hierdie module/werkstuk of 'n ander module/werkstuk nie.  
*I declare that the work contained in this assignment, except otherwise stated, is my original work and that I have not previously (in its entirety or in part) submitted it for grading in this module/assignment or another module/assignment.*

R.Swart Voorletters en van / <i>Initials and surname</i>	December 2018 Datum / <i>Date</i>
---	--------------------------------------

## SUMMARY

The main focus of this project was an investigation into a full-scale, 27 m high, 6 m wide thermosyphon loop, which can be used as a fully passive high temperature reactor (HTR) cavity cooling system (RCCS). Thermosyphon loops are closed thermodynamic systems, in which the working fluid inside the loop is driven by a temperature induced density gradient. This density gradient causes the working fluid to be circulated naturally. The literature study that was conducted showed that extensive theoretical and experimental research has been done on thermosyphons. The literature study focused on understanding the safety, instabilities, control and mathematical modelling of these systems.

A 27 m high, 6 m wide water-filled thermosyphon loop was recommissioned. The heat input was simulated with 25 heating elements, which were evenly spaced and positioned on the left-hand side vertical pipe. The heat removal system relied on counter-current heat exchangers on the right-hand vertical and top horizontal pipe of the system. The thermosyphon loop was open to the atmosphere by means of an expansion tank connected at the bottom of the loop and positioned 30 m in the air. The expansion tank ensured that the working fluid did not experience any pressure buildup, and ensured that it remained at a constant pressure. Three transparent sections were inserted into the system to observe the working fluid flow regime inside the loop. These sections were positioned above the heat input section, after the horizontal condenser section and before the vertical condenser section.

The recommissioned thermosyphon was operated under different operating conditions. The different operating conditions were repeated, and they were observed to deliver almost the same result; thus showing that the experiments were repeatable. The flow pattern behaviours were established for the flow patterns observed in the transparent sections of the loop.

A time-dependent mathematical simulation thermal-hydraulic model of the thermosyphon loop was developed. The simulation model is based on a one-dimensional axially symmetrical control volume approach, where the loop is divided into a series of discrete control volumes. The three conservation equations, namely, mass, momentum and energy, were applied to these control volumes and solved with an explicit numerical method. The following main assumptions were made: The flow is quasi-static, implying that the mass flow rate changes over time, but at any instant in time, the mass flow rate is constant around the loop; and that the expansion tank does not have an effect on the system.

It was found that the Lockhart-Martinelli void fraction and Friedel frictional multiplier, compared to a number of correlations, predicted the separated two-phase flow regime of the working fluid the most accurately. The temperatures and mass flow rate of the theoretical model corresponded reasonably well with the experimental results.

The conclusion was reached that the exploratory study on thermosyphon loops is a viable option for an high temperature reactor (HTR) cavity cooling system (RCCS), and that a series of loops could be used. The theoretical simulation model is a viable simulation tool for predicting the working fluid temperatures and flow regimes of this system. Several recommendations are made regarding the theoretical model and the experimental setup. The most important recommendation is to reconstruct the thermosyphon loop in a more controlled environment (indoors) to increase the accuracy of the theoretical simulation.

## OPSOMMING

Die hoofokus van hierdie projek was die ondersoek van 'n volskaalse 27 m hoë, 6 m wye termohuwellus, wat gebruik kan word as 'n volledig-passiewe reaktorholte-verkoelingsstelsel (RCCS). Termohuwellusse is 'n geslote termodinamiese stelsel waarin die werkvloeistof in die lus gedryf word deur 'n temperatuurverskil digtheidsgradiënt wat veroorsaak dat die werkvloeistof natuurlik gesirkuleer word. 'n Literatuurstudie is uitgevoer en het getoon dat uitgebreide navorsing oor termosifone teoreties en eksperimenteel gedoen is. Die literatuur het gefokus op die begrip van veiligheid, onstabiliteit, beheer en die wiskundige modellering van hierdie stelsels.

'n 27 m hoë, 6 m wye watergevulde termohuwellus is weer in gebruik geneem. Die hitte-insette is gesimuleer met 25 verwarmingselemente, wat eweredig gespaseer en geplaas is aan die linkerkantse vertikale pyp. Die hitteverwyderingstelsel is deur teenstroom warmtewisselaars aan die regterkantse vertikale en boonste horisontale pyp van die stelsel gedoen. Die termohuwellus was bloot gestel aan die atmosfeer deur middel van 'n uitsettingstenk wat onderaan die lus verbind is en 30 m in die lug geplaas was. Die uitsettingsstenk het verseker dat die werkende vloeistof nie druk opgebou het nie en dat dit teen konstante druk bly. Drie deursigtige afdelings is in die stelsel geplaas om die werkvloeistroomregime binne die lus waar te neem. Hulle is bo die hitte-insetgedeelte geplaas, na die horisontale waterkoeler en voor die vertikale waterkoeler afdeling.

Die her inwerkstelling termohuwellus is onder verskillende bedryfstoeënde bedryf. Die verskillende bedryfsomstandighede is herhaal en daar is waargeneem dat byna dieselfde resultaat gelewer is, en sodoende bewys dat die eksperimente herhaalbaar was. Die vloeipatrone se gedrag is vasgestel soos waargeneem in die deursigtige dele van die lus.

'n Tydafhanklike wiskundige simulasiemodel van die termohuwellus is ontwikkel. Die simulasiemodel is gebaseer op 'n beheerde eendimensionele simmetriese volumebenadering, waar die lus in 'n reeks diskrete beheervolumes verdeel word. Die drie bewaringsvergelykings, massa, momentum en energie is toegepas op hierdie beheervolumes en opgelos met 'n eksplisiete numeriese metode. Die volgende hoofaannames is gemaak: die vloei is kwasi-stasies, wat impliseer dat die massa vloei-tempo oor tyd verander, maar op enige tydstep, die massastroming is konstant om die lus en dat die uitbreidingstenk nie 'n effek op die stelsel het nie.

Daar is bevind dat die Lockhart-Martinelli leemte fraksie en Friedel wrywingsvermenigvuldiging koëffisiënt, in vergelyking met 'n aantal korrelasies, die gesproke tweefase regime van die werkvloeistof die akkuraatste voorspel het. Die temperatuur en massa vloei van die teoretiese model het redelik goed met die eksperimentele resultate ooreen gestem.

Die gevolgtrekking is gemaak dat die verkennende studie oor termoeuwellusse 'n lewensvatbare opsie is vir 'n reaktorholte-verkoelingstelsel (RCCS) en dat 'n reeks lusse gebruik kan word. Die teoretiese simulasiemodel is 'n lewensvatbare simuleringsinstrument vir die voorspelling van die werkvloei-stowwe en vloei-stelsels van hierdie sisteem.

Verskeie aanbevelings is gemaak aangaande die teoretiese model en die eksperimentele opstelling. Die belangrikste aanbeveling is om die termoeuwellus in 'n meer beheerde omgewing (binnenshuis) te rekonstrueer om die akkuraatheid van die teoretiese simulatie te verhoog.

## **ACKNOWLEDGEMENTS**

The following people are thanked for their contribution toward this project, without which the completion of this project would not have been possible:

Mr. Robert Dobson, special thanks to you for your patience, support, guidance and giving me the opportunity to do my masters.

J.C Ruppertsberg for the construction, calibration and experimental data taken of the thermosyphon loop.

Cobus Zietsman and Juliun Stanfliet for helping with the recommissioning of the loop and sharing their practical knowledge with me.

My family for believing in me and giving me the opportunity to realise my ambitions.



## TABLE OF CONTENT

DECLARATION	i
PLAGIAATVERKLARING / PLAGIARISM DECLARATION	ii
SUMMARY	iii
OPSOMMING	v
ACKNOWLEDGEMENTS	vii
LIST OF TABLES	xi
LIST OF FIGURES	xii
NOMENCLATURE	xv
<b>1 INTRODUCTION</b>	<b>1-1</b>
1.1 Background	1-2
1.2 Motivation	1-5
1.3 Objective	1-5
1.4 Report layout	1-6
<b>2 LITERATURE REVIEW</b>	<b>2-1</b>
2.1 General thermosyphon loops	2-1
2.2 Mathematical model	2-7
2.2.1 Separated two-phase flow void fraction	2-7
2.2.2 Two-phase flow internal heat transfer coefficient	2-9
2.3 Instabilities	2-11
<b>3 TWO-PHASE FLOW AND HEAT TRANSFER THEORY</b>	<b>3-1</b>
3.1 Assumptions and equations of change	3-1
3.2 Separated two-phase flow model	3-4
3.2.1 Separated two-phase flow void fraction	3-4
3.2.2 Martinelli parameter	3-7
3.3 Two-phase friction multiplier	3-99
3.4 Minor losses	3-10
3.5 Heat transfer coefficient	3-11

3.5.1 Single-phase heat transfer coefficient	3-11
3.5.2 Evaporator heat transfer coefficient	3-12
3.5.3 Condenser vertical side heat transfer coefficient	3-14
3.5.4 Top horizontal pipe heat transfer coefficient	3-166
3.5.5 Condenser static and active cooling water	3-177
3.6 Heat transfer	3-199
3.7 Equations of change used numerically	3-277
3.7.1 Conservation of mass	3-277
3.7.2 Conservation of energy	3-277
3.7.3 Conservation of momentum	3-299
3.8 Property functions and external inputs	3-3131
3.9 Mathematical model procedure	3-322
<b>4 EXPERIMENTAL SETUP</b>	<b>4-1</b>
4.1 Geometry and materials	4-2
4.2 Recommissioning	4-3
4.3 Sensors	4-3
4.4 Data acquisition	4-4
4.5 Operational procedures	4-4
<b>5 OBSERVATIONS AND RESULTS</b>	<b>5-1</b>
5.1 Experimental sets 1 and 2	5-1
5.2 Theoretical modelling	5-7
5.2.1 Void fraction and frictional multiplier comparison	5-9
5.2.2 Comparison of theoretical and experimental models	5-14
5.2.3 Experimental and theoretical comparison of system pressure	5-19
5.2.4 Experimental and theoretical comparison of single phase region	5-190
5.3 Conclusion summary	5-22
<b>6 CONCLUSION</b>	<b>6-1</b>
<b>7 RECOMMENDATIONS FOR FUTURE WORK</b>	<b>7-1</b>
7.1 Condenser water	7-1

7.2 Environmental losses	7-1
7.3 Mass flow rate measurement	7-1
7.4 Mathematical model	7-1
<b>8 REFERENCES</b>	<b>8-1</b>
<b>APPENDIX A DERIVATION OF EQUATIONS</b>	<b>A-1</b>
A.1 Continuity equation	A-1
A.2 Momentum equation	A-2
A.3 Derivation of thermal energy equation	A-4
A.4 Heat conduction through a cylindrical shell	A-6
A.5 Internal energy of structure	A-8
A.6 CISE correlation	A-9
A.7 Friedel correlation for frictional two-phase multiplier	A-10
<b>APPENDIX B THEORETICAL PROGRAM ALGORITHM</b>	<b>B-1</b>
<b>APPENDIX C PROPERTY FUNCTIONS</b>	<b>C-1</b>
C.1 Properties of water	C-1
C.2 Properties of stainless	C-4
C.3 Properties of Nickel-chrome heating element	C-4
C.4 Properties of insulation material	C-4
<b>APPENDIX D CALIBRATIONS</b>	<b>D-1</b>

## LIST OF TABLES

Table 1 Separated void correlations and methods .....	2-9
Table 2 Correlation of constant C and Reynolds numbers for friction multiplier	3-10
Table 3 Minor loss components identified and their equivalent lengths .....	3-11
Table 4 Different void fraction and frictional multiplier cases used to determine the most appropriate theoretical prediction method for the performance of two-phase flow systems .....	5-10
Table C-1 Saturated liquid specific internal energy $u_f$ as a function of pressure.....	C-1
Table C-2 Saturated vapour specific internal energy $u_g$ as a function of pressure ..	C-1
Table C-3 Saturated liquid density $\rho_l$ as a function of pressure in kJ/kg if P in kPa .....	C-1
Table C-4 Saturated vapour density $\rho_g$ as a function of pressure in kJ/kg if P in kPa .....	C-2
Table C-5 Saturated temperature $T_{sat}$ as a function of pressure in kJ/kg if P in kPa .....	C-2
Table C-6 Subcooled liquid density $\rho$ as a function of specific internal energy and pressure in $\text{kg/m}^3$ if $u$ in kJ/kg and $P$ in kPa.....	C-2
Table C-7 Subcooled liquid temperature $T$ as a function of specific internal energy and pressure in $^{\circ}\text{C}$ if $u$ in kJ/kg and $P$ in kPa.....	C-3
Table C-8 Superheated vapour temperature $T$ as a function of specific internal energy and pressure in $^{\circ}\text{C}$ if $u$ in kJ/kg and $P$ in kPa .....	C-3
Table C-9 Saturated liquid viscosity $\mu_l$ as a function of temperature in kg/ms if $T$ in $^{\circ}\text{C}$ .....	C-3
Table C-10 Saturated vapour viscosity $\mu_g$ as a function of temperature in kg/ms if $T$ in $^{\circ}\text{C}$ .....	C-4
Table C-11 Liquid-vapour surface tension for water, SIGMA in N/m if $T$ in C.	C-4
Table D-1 Differential pressure transducer calibration .....	D-1
Table D-2 Static pressure transducer calibration.....	D-2
Table D-3 Working fluid thermocouple calibration .....	D-4

## LIST OF FIGURES

Figure 1 Simple illustration of experimental setup of the thermosyphon loop .....	1-1
Figure 2 Schematic presentation of the axially symmetrical RCCS (Dobson, 2006) .....	1-3
Figure 3 Image (a) top section of thermosyphon loop, (b) bottom section of thermosyphon loop, (c) full-scale rectangular thermosyphon loop .....	1-4
Figure 4 Idealised closed loop thermosyphon, re-sketched (Vincent & Kok, 1992)... .....	2-2
Figure 5 Semi-closed two-phase natural circulation loop (Lee & Kim, 1999).....	2-3
Figure 6 Theoretical model of the two-phase thermosyphon loop (Bieliński, 2016) .....	2-4
Figure 7 Schematic representation of a closed loop thermosyphon for a reactor cavity cooling system (Dobson & Ruppertsberg, 2007).....	2-5
Figure 8 Discretisation scheme of the thermosyphon loop.....	3-1
Figure 9 Conservation of mass (a), momentum (b), energy (c) as applied to a representative control volume with cross-sectional area $A$ , area in contact with the pipe $A_z$ and length $\Delta z$ .....	3-3
Figure 10 Illustration of an idealised one-dimensional model of separated “two- phase” flow inside a pipe .....	3-4
Figure 11 Flow regimes of the working gas-liquid flow inside the 27 m natural circulation loop observed through the top left sight glass .....	3-6
Figure 12 Right-hand side vertical pipe sight glass indicating annular flow.....	3-15
Figure 13 Top horizontal tube sight glass indicating stratified flow (vapour at top and liquid at the bottom).....	3-16
Figure 14 Heat transfer representation of the left-hand electric heating element side of the loop .....	3-19
Figure 15 Heat transfer representation of the right-hand condenser side of the loop .....	3-22
Figure 16 Heat transfer representation of the top condenser of the loop.....	3-23

Figure 17 Heat transfer representation of the bottom of the loop.....	3-24
Figure 18 Pressure-specific internal energy diagram showing a sub-cooled liquid 1, a two-phase vapour plus liquid 2 and a vapour 3 (Senda, 2018).....	3-31
Figure 19 The sequence of steps followed by the mathematical model to predict the flow of the working fluid.....	3-32
Figure 20 Illustration of the 27 x 6 m natural circulation loop with the cooling system.....	4-1
Figure 21 Experimental mass flow rate measurements over time and flow regimes as observed through vertical sight glass for set 1.....	5-2
Figure 22 Working fluid temperatures over time (a), and pressure over time (b), for set 1.....	5-4
Figure 23 Experimental mass flow rate measurements over time and flow regimes as observed through vertical sight glass for set 2.....	5-5
Figure 24 (a) Working fluid temperatures over time, (b) Pressure over time, for set 2.....	5-6
Figure 25 (a) Benchmark experimental mass flow rate over time (b) working fluid experimental temperatures over time.....	5-8
Figure 26 Benchmark heat input and heat removed from thermosyphon loop over time.....	5-9
Figure 27 CISE correlation with the Lockhart-Martinelli frictional multiplier. Predicted theoretical results of working fluid (a) mass flow rate (b) temperatures.....	5-10
Figure 28 CISE correlation with the Friedel frictional multiplier. Predicted theoretical results of working fluid (a) mass flow rate (b) temperatures.....	5-11
Figure 29 Lockhart-Martinelli model with Lockhart-Martinelli frictional multiplier. Predicted theoretical results of working fluid (a) mass flow rate (b) temperatures.....	5-11
Figure 30 Lockhart-Martinelli model with Friedel frictional multiplier. Predicted theoretical results of working fluid (a) mass flow rate (b) temperatures.....	5-12
Figure 31 Homogeneous model with homogeneous frictional multiplier. Predicted theoretical results of working fluid (a) mass flow rate (b) temperatures.....	5-12

Figure 32 Homogeneous model and Friedel frictional multiplier. Predicted theoretical results of working fluid (a) mass flow rate (b) temperatures.....	5-13
Figure 33 Homogeneous model and Lockhart-Martinelli frictional multiplier. Predicted theoretical results of working fluid (a) mass flow rate (b) temperatures.....	5-13
Figure 34 Comparison of experimental and theoretical mass flow rate over time .....	5-15
Figure 35 Comparison of benchmark experiment and theoretical working fluid temperatures over time.....	5-16
Figure 36 Comparison of experimental set 2 and theoretical mass flow rate over time .....	5-17
Figure 37 Comparison of experimental set 2 and theoretical working fluid temperatures over time.....	5-18
Figure 38 a) Theoretical mass flow rate of experimental set 2 over time, b) Experimental and theoretical pressure of experimental set 2 over time .....	5-20
Figure 39 a) Theoretical and experimental mass flow rate over time, b) theoretical and Experimental temperatures over time .....	5-21
Figure A-1 Region of volume $\Delta x \Delta y \Delta z$ fixed in space through which a fluid is flowing (in the x-direction).....	A-1
Figure A-2 Region of volume $\Delta x \Delta y \Delta z$ fixed in space through which a fluid is flowing (in the x-direction).....	A-3
Figure A-3 A cylindrical shell showing an elemental control volume for application of the energy conservation principle.....	A-7
Figure D-1 Orifice plate mass flow rate as a function of the differential pressure across the orifice calibration.....	D-3

**NOMENCLATURE**

$A$	Area, $m^2$
$A_x$	cross-sectional area, $m^2$
$A_z$	heat transfer area, $m^2$
$B$	constant
$c$	specific heat, $J/kg\ K$
$C$	constant
$C_f$	fanning friction factor
$D$	inner pipe diameter, $m$
$f$	frequency, $Hz$
$f$	Darcy friction factor
$g$	gravitational acceleration, $m/s^2$
$Gr$	Grashof number, $Gr = (g \beta \Delta T / (\mu / \rho)^2) L^3$
$l$	length, $m$
$L$	length of element, $m$
$h$	convection coefficient, $W/m^2\ K$
$h_{fg}$	enthalpy of vapourisation, $J/kg$
$h'_{fg}$	enthalpy of vapourisation plus subcooling correction, $J/kg$
$k$	thermal conduction coefficient, $W/mK$
$m$	mass, $kg$
$\dot{m}$	mass flow rate, $kg/s$
$n$	constant
$N$	number of control volumes
$Nu$	Nusselt number, $Nu = h d / k$
$P$	pressure, $Pa$
$\wp$	perimeter, $m$
$Pr$	Prandtl number, $Pr = \mu c_p / k$
$Q$	heat transfer, $J$
$\dot{Q}$	heat flow rate, $W$
$R$	thermal resistance, $K/W$
$Ra$	Rayleigh number, $Ra = Gr Pr$
$Re$	Reynolds number, $Re = \rho v d / \mu$



$S$	compression factor, slip factor
$St$	Strouhal number, $St = fL/V$
$T$	temperature, $C^\circ$
$u$	specific internal energy, J/kg
$t$	time, s
$V$	Volume, $m^3$
$\dot{V}$	Volumetric flow rate, $m^3/s$
$v$	velocity, m/s
$x$	quality of fluid
$X$	turbulent-turbulent Martinelli parameter

### Greek symbols

$\sigma$	interfacial tension, N/m
$\beta$	thermal expansion coefficient, 1/K.
$\mu$	dynamic viscosity, kg/m s
$\mu$	kinematic viscosity, $m^2/s$
$\tau$	shear stress, Pa
$\rho$	density, $kg/m^3$
$\phi$	frictional multiplier

### Subscripts

$amb$	ambient
$c$	convection/condenser/cooling
$ccw$	condenser cooling water
$ci$	condenser inner
$clad$	cladding
$co$	condenser outer
$conv$	convection
$cw$	condenser wall
$dc$	downcomer (return line)
$e$	heating element

<i>exp</i>	experimental
<i>eq</i>	equivalent
<i>f</i>	friction
<i>ft</i>	flash tube (riser)
<i>g</i>	gas
<i>h</i>	homogeneous
<i>i</i>	inner, the i'th control volume
<i>in</i>	variable into control volume
<i>ins</i>	insulation
<i>l</i>	liquid
<i>lo</i>	liquid only
<i>lv</i>	liquid-vapour
<i>mac</i>	macroscopic
<i>mic</i>	microscopic
<i>r</i>	reactor/radius/radiation
<i>rad</i>	radiation
<i>rc</i>	radiation and convection
<i>sat</i>	saturation
<i>s</i>	sleeve
<i>ss</i>	stainless steel
<i>surr</i>	surrounding
<i>th</i>	theoretical
<i>tot</i>	total
<i>tt</i>	turbulent-turbulent
<i>v</i>	vapour
<i>w</i>	wall/water
<i>r</i>	radiation
<i>sdl</i>	steam drum
<i>p</i>	pipe
<i>pw</i>	pipe wall
<i>o</i>	outer
<i>out</i>	variable out of control volume

$x$  x-axis

$z$  z-axis

## **Superscripts**

$t$  time

$\Delta t$  change in time (time step)

$\dot{\phantom{x}}$  (over dot) quantity per unit time

## **Abbreviations**

BC bottom cooling

BE bottom element

$F$  friction term

HTR high temperature reactor

$MF$  momentum flux

$MM$  momentum term

PVC polyvinyl chloride

RCCS reactor cavity cooling system

TC top cooling

TE top element

## 1 INTRODUCTION

A semi-closed thermosyphon loop is a heat removal system that does not use any mechanical, moving parts, such as pumps or active controls (Ruppersberg & Dobson, 2007). The absence of moving parts results in minimum downtime of a system, which renders the system very safe. Other advantages of a semi-closed thermosyphon is the increase of flow in as heat increases, and that the heat can be transferred over relatively large distances.

A thermosyphon loop is one of the best heat transfer methods available (Ruppersberg & Dobson, 2007). Many applications in different fields arose from the main characteristic of a thermosyphon loop, namely, that the fluid inside does not need a pump to be circulated, hence, it is a passive system. Some of these applications are used for cooling very small electronic devices (Bielński, 2016; Cao & Gao, 2002; Sundaram & Bhaskaran, 2011); for industrial applications, such as heating oil baths (Vincent & Kok, 1992), and for solar applications (Abreu & Colle, 2004; Yilmaz, 1991). Loop thermosyphons are not restricted to a square geometrical shape but can have multiple shapes and multiple bends (Venkata & Bhramara, 2017). Due to the reliability of thermosyphon cooling systems, Dobson and Ruppersberg (2007) suggest that a rectangular thermosyphon loop can be used for cooling a nuclear reactor cavity.

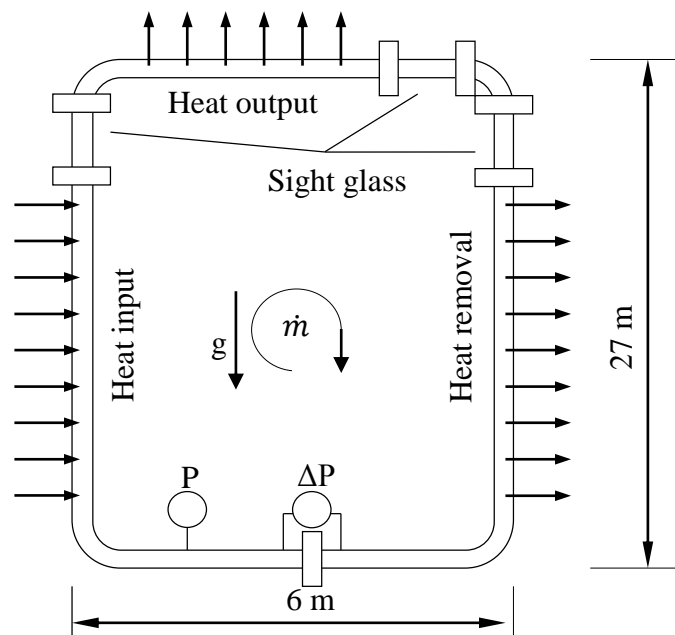


Figure 1 Simple illustration of experimental setup of the thermosyphon loop

A general rectangular thermosyphon loop consists of an evaporator section (heat gain), which is usually connected to the riser pipe in which the fluid moves upwards, and a condenser section (heat removal), which is usually connected to a downcomer, the line in which the working fluid returns to the evaporator section (see Figure 1).

Natural circulation is the phenomenon that occurs when the fluid inside the thermosyphon loop circulates by simply adding and removing heat, without an additional pump being used to drive the fluid. During natural circulation, the heat is transferred from the heating region (evaporator) to the cooling region (condenser). The fluid flow is caused by a net upward body force, which is called the buoyancy force. The buoyancy force is proportional to the density gradient, which is proportional to the temperature difference (heating and cooling section) at constant pressure. The buoyancy force pushes fluid upwards and the gravity force brings it back down, resulting in a fully passive cooling system (Bieliński, 2016).

## 1.1 Background

Major nuclear accidents, such as the Chernobyl (1986), Three Mile Island (1979) and Fukushima incidents (2011), have caused the public's view on nuclear energy to turn negative. The Chernobyl reactor was destroyed by a combination of factors, among which, safety violations, faulty design of control rods, and the lack of a reactor cavity. The main cause of the Chernobyl accident, however, was that experiments were being conducted, which was a gross violation of safety systems. Chernobyl was the second major nuclear accident to occur after the Three Mile Island accident. However it was the first nuclear reactor incident to release major reactivity into the surrounding area and seriously impact the public's opinion of nuclear energy. The Three Mile Island incident was caused by instrumentation failure and failure to diagnose the event. This accident led to a major shift in nuclear technology, towards highlighting the importance of passive safety systems. The last major incident, Fukushima, was caused by a tsunami, which occurred after an earthquake (Vikas *et al.*, 2013). The tsunami caused the Fukushima reactor to experience a prolonged blackout, which led to the failure of the transmission grid and drowned a diesel generator that was designed to deliver power in the event of failure. The reactor structure was not damaged and the reactor was shut down safely, but people within a 30 km radius had to be evacuated and radioactive elements leaked into the environment (Siegrist & Visschers, 2013). This incident could have been averted if the reactor was appropriately designed.

Goodfellow *et al.* (2015) conducted a study, including a survey, to investigate public concerns regarding the current design of nuclear reactors. The most important concerns identified are nuclear waste disposal, safety, radiation discharges, environmental impacts, the possibility of terrorism, cost and proliferation of nuclear weapons and waste. This study indicated that the safety of

a nuclear reactor plays a key role in the outlook that the public has on nuclear energy. Investigating the three major nuclear incidents makes it clear that human error was the result of these disasters. This project is focused on improving the public's view of nuclear energy, by improving the safety of reactors by implementing passive technology and reducing the active components used in nuclear reactors. In short, the project aims to investigate a thermosyphon loop that could make nuclear reactors inherently safer. Inherent safety characteristics are defined as, "Safety achieved by the elimination of a specified hazard by means of the choice of material and design concept" (IAEA, 1991).

Passive safety systems have considerable advantages over active systems, among which being simpler, having potential economic benefits, and increasing the reliability of essential safety functions. Some passive systems can eliminate the costs associated with installation, maintenance and operation of active systems, such as the control of pumps, valves and power supplies.

Natural circulation can address the drawbacks of traditional cooling systems (active systems), by reducing the biggest problem faced by nuclear reactors, which is human error. Dobson (2006), in a paper presented at the 8<sup>th</sup> International Heat Pipe Symposium in Kumamoto, proposed a closed loop thermosyphon cooling system for a high temperature reactor (HTR) cavity cooling system (RCCS). In this concept, a number of closed loop thermosyphon pipes are spaced around the periphery of the reactor cavity, with the heating section in the hot air cavity and the condenser section in a heat sink (see Figure 2).

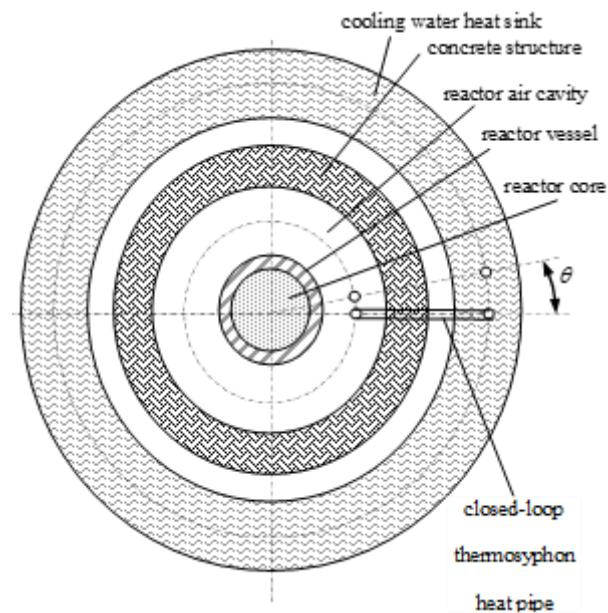


Figure 2 Schematic presentation of the axially symmetrical RCCS (Dobson, 2006)

Ruppersberg and Dobson (2007) built a small-scale test setup of the cavity cooling system proposed by Dobson (2006); this setup researched the thermosyphon technology and showed that the technology can be used on a small scale. Sittmann (2010) constructed and tested an 8 m wide, 7 m high thermosyphon loop based on Dobson's (2006) cavity cooling proposal. This loop was tested, simulated and, later, recommissioned and simulated by Senda (2018). In 2012 Ruppersberg constructed a full-scale model (27 m high and 6 m wide) of a reactor cavity cooling system. This full-scale model has yet to be tested and simulated, and this test and simulation is presented in this study (see Figure 3 full scale model built by Ruppersberg).

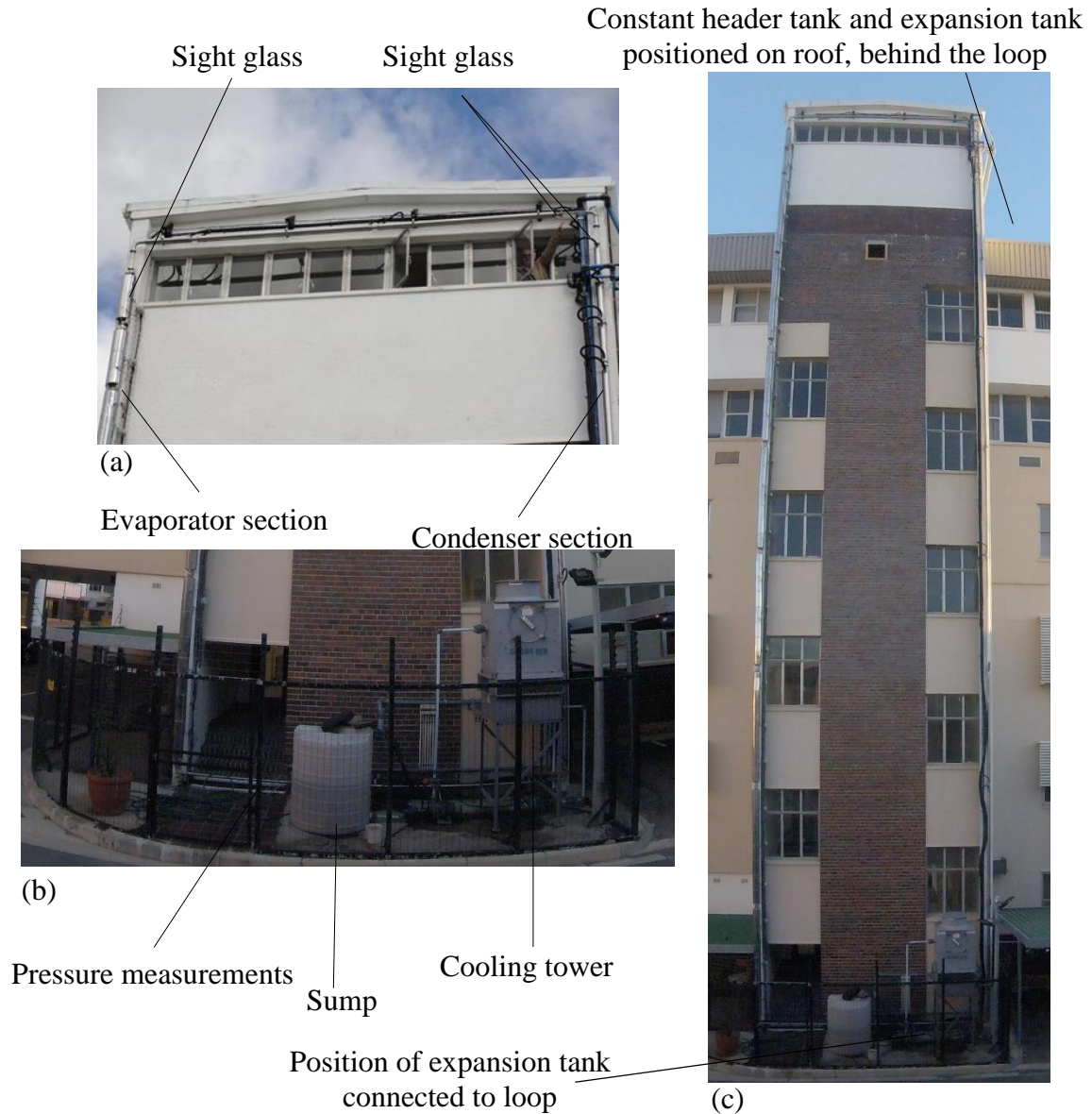


Figure 3 Image (a) top section of thermosyphon loop, (b) bottom section of thermosyphon loop, (c) full-scale rectangular thermosyphon loop

## 1.2 Motivation

The next generation (so-called Gen IV) reactors will tend to operate at higher temperatures than present-day pressurised and boiling water reactors, thus, the need for additional reactor cavity cooling equipment. An experimental loop was built to demonstrate suitable cooling systems, and initial results showed that adequate cooling could be claimed with such loops (Dobson & Ruppertsberg, 2007; Verwey, 2010). The theoretical simulation of these loops used a simple, homogeneous two-phase modelling technique, but the simulation was not able to accurately capture the detailed two-phase characteristic of the system; this inability led to the opportunity to investigate this matter in a thesis project, of which the goal was simply to recommission the system and develop a more advanced two-phase separated flow model of the system.

## 1.3 Objective

To achieve the overall goal of the study, the following objectives were identified:

- i) Conduct a literature study on existing thermosyphon technology, the different methods that numerically simulate a thermosyphon loop and experimental setups, and increase understanding of the transient effects of such a system.
- ii) Recommission the 27 m high, 6 m wide natural circulation reactor cavity cooling loop.
- iii) Operate the recommissioned loop under different heating and cooling conditions and determine its transient start-up and dynamic single- and two-phase flow characteristics in terms of the mass flow rate, important temperatures and pressures for different power inputs and condenser cooling flow rates and positions.
- iv) Develop the theoretical simulation of the thermosyphon loop using a separated two-phase flow model. This model was considered because the simple, homogeneous flow model does not appear to capture the separated transient flow behaviour in a thermosyphon loop accurately (Dobson & Ruppertsberg, 2007; Verwey, 2010; Yilmaz, 1991).
- v) Run the simulation program for various operating conditions to predict the characteristics of the thermosyphon loop.
- vi) Determine the temperature and pressure differences and fluctuations under different power inputs and cooling conditions experimentally. Furthermore, establish the flow pattern behaviour as seen in the transparent sections of the loop under different operating conditions.
- vii) Compare simulated data with experimental results to establish the ability of the theoretical simulation model to capture the experimental loop behaviours under various operating conditions.



## 1.4 Report layout

In this report, Section 1 is an introductory section that presents the objectives, motivation and background concerning this study. Section 2 will report on a literature study, done on the latest thermosyphon loop technology and different separated flow models that were used to create theoretical models for predicting the flow inside thermosyphon loops. The theory obtained from the literature study was used to develop a theoretical two-phase flow model of the thermosyphon loop – this model will be presented in Section 3. Section 4 will deal with the experimental setup on which the theoretical model is based, and the recommissioning of this experimental setup. The instrumentation, calibrations and operational procedures will also be presented in this section. The experimental measurements of the recommissioned loop with the identified transient start-up and dynamic single- and two-phase flow characteristics will be presented in Section 5. Section 5 will also include the results of the theoretical model. The theoretical flow model and experimental measurements will be compared and the ability of the theoretical model to simulate the thermosyphon loop will be discussed. Section 6 will present the final conclusion of the project, and Section 7 will offer recommendations for future work concerning thermosyphon loops.

## 2 LITERATURE REVIEW

The focus of this section is to develop a greater understanding of the safety, instabilities, control and mathematical modelling of thermosyphon loops. A broad investigation of different thermosyphon loops that were used in different scenarios, and the methods used to predict the flow in these systems, will be reported. The next section will investigate different methods of predicting the separated two-phase flow region of the working fluid. The last section will investigate the instabilities that have been identified in thermosyphon loops.

### 2.1 General thermosyphon loops

Yilmaz (1991) wrote a computer simulation program for a two-phase flow thermosyphon solar water heating system. In his research, he compared a homogeneous model and a separated flow (slug) model of a solar water heating system. The working fluid he used was refrigerant R-11. The working fluid enters the collector (heating section) in a subcooled state, and it is heated to saturation temperature. After the collector, the fluid is separated in a cyclone, where the liquid flows to the reservoir and the vapour goes to the condenser. In the condenser, the vapour transfers its latent heat to the surrounding heating water, and the vapour returns to the liquid phase. When Yilmaz compared the capability of the homogeneous model and separated-flow model to predict the flow inside the system using the mass fraction as indication (quality), he came to the conclusion that the homogeneous flow model is not sufficient to describe the two-phase flow in the collector (heating section).

Vincent and Kok (1992) investigated the overall transient performance of an industrial two-phase closed loop thermosyphon. These industrial thermosyphons can handle heat up to 250°C. A control volume approach using one-dimensional equations was used to investigate the predicted motion of the liquid and vapour phases inside a thermosyphon system. The physical system can be seen in Figure 4. The vapour and liquid are transported using a system of pipes, the evaporator section is heated using heating coils, and the condenser section is cooled using an interchangeable oil bath. The evaporator's cross-section is larger than the condensers, causing a large elevation in water level.

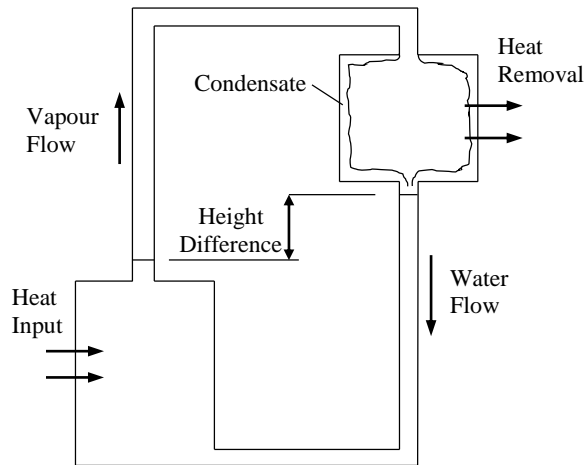


Figure 4 Idealised closed loop thermosyphon, re-sketched (Vincent & Kok, 1992)

Vincent and Kok (1992) verified that, for a well-insulated natural circulation loop, the system can be described by two temperature characteristics, the evaporator and condenser sections. They proved this characteristic by taking temperature measurements of three different industrial thermosyphons. For the one-dimensional model, the following assumptions were made: neglecting the heat capacitance of the system; heat losses to the environment; axial conduction and the viscous dissipation. The analysis was done using only two control volumes across the evaporator and the condenser, and applying the mass, energy, and momentum balances on these control volumes. Vincent and Kok (1992) concluded that response time, damping and oscillation frequency can be determined from the characteristics density ratio (vapour-liquid), dimensionless friction coefficient and water column length respectively.

Lee and Kim (1999) did an analytical investigation into the role of an expansion tank in a semi-closed two-phase natural circulation loop. In their research, they used a simple homogeneous flow model, with water as the working fluid, to investigate the effects that the flow has on the expansion tank. According to Lee and Kim (1999), using the simple homogenous flow model does not detract the meaningfulness of their analysis. The expansion tank allows the time-average system pressure to remain constant, because the excess liquid (volume expansion) is able to push outwards, into the expansion tank, where a constant pressure head is maintained. The changing factor that was investigated was the instantaneous system-pressure, which was influenced by inertia, due to the liquid inside the expansion tank line, and the friction resistance related to the fluid. The same pipe dimensions were used for all the different sections of the loop. Figure 5 illustrates the test setup.

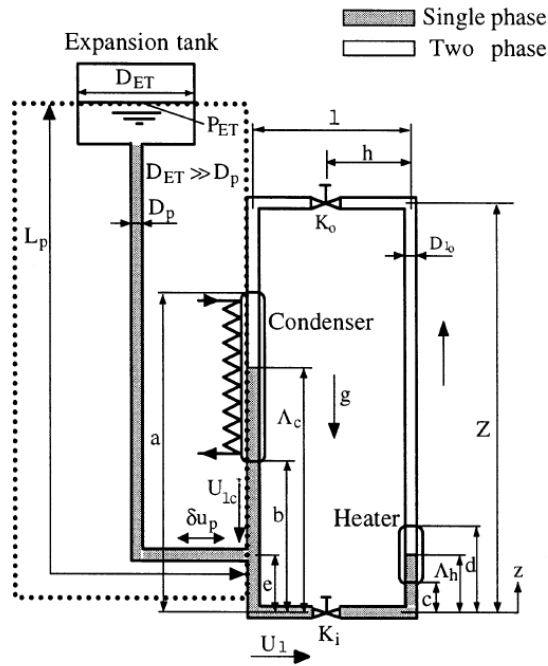


Figure 5 Semi-closed two-phase natural circulation loop (Lee & Kim, 1999)

Lee and Kim (1999) found that the flow becomes more stable with a longer expansion tank line, and vice versa. The frictional pressure drop and inertia inside the expansion tank line becomes very large with a longer line and does not react significantly to instantaneous pressure fluctuations inside the loop. Lee and Kim (1999) also found that an expansion tank line with a bigger diameter decreases the stability of the flow; the reason for this decrease is that viscous damping decreases as the diameter decreases. Thus, an expansion tank line that is long enough, with a diameter that is small enough, ensures that the time-average pressure inside the thermosyphon loop stays constant and does not affect the flow inside the loop.

Bieliński (2016) used experimental measurements of volumetric flow rate to validate a general model of a two-phase thermosyphon loop. The experimental setup consists of a rectangular thermosyphon loop with the evaporator on the bottom left of the riser, and the condenser on the top right of the downcomer (working fluid return line) (see Figure 6).

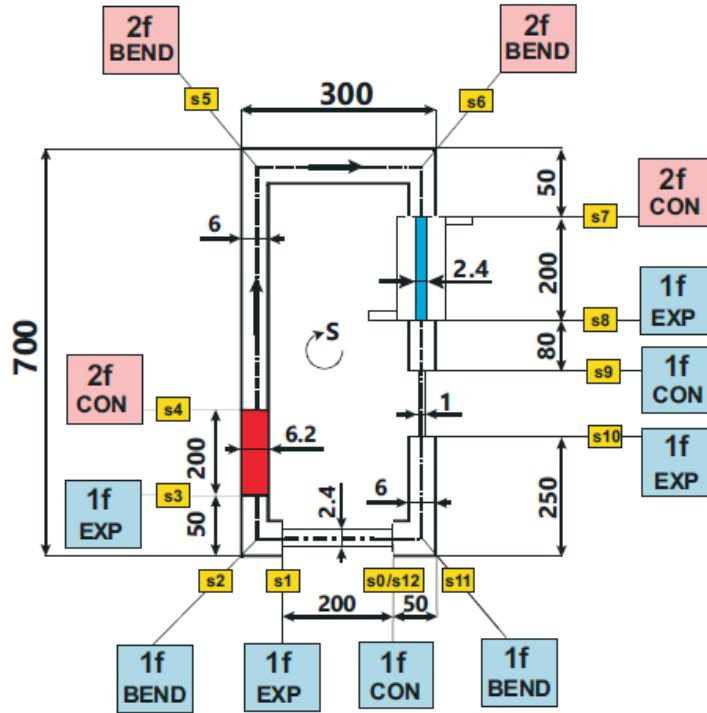


Figure 6 Theoretical model of the two-phase thermosyphon loop (Bieliński, 2016)

Bieliński assumed that a one-dimensional model could be applied to the system, because the diameter of the pipe, divided by the length of the riser, is smaller than 1,  $(D/L) \ll 1$ . He also assumed that the Boussinesq approximation was valid for the working fluid; then density is assumed to vary as  $\rho = \rho_0[1 - \beta(T - T_0)]$  in the gravity term, where  $\beta = \frac{1}{v} \left( \frac{\partial v}{\partial T} \right)_p$ , and  $v$  is specific volume and the subscript 0 is the reference steady state. Bieliński (2016) also used a friction factor multiplier to calculate the frictional pressure loss, and stated that a homogeneous or separated flow model can be used to evaluate the frictional pressure drop. These and more general assumptions, not mentioned here, were used with the governing equations to determine the volumetric flow in the thermosyphon loop. The momentum term in the conservation of momentum was integrated around the loop to eliminate it from the conservation of momentum equation, see equation 2.1.

$$\oint \left( \frac{dP}{dz} \right) dz = 0, P(0) = P(L) \quad (2.1)$$

A thermal imaging camera was used in the test setup to validate the negligibility of heat loss to the environment, and an ultrasonic flow meter was used to measure the experimental volumetric flow. The results show that the homogeneous flow model does not describe the nature of the flow accurately. The separated flow

model predictions were in good agreement with the volumetric flow rate at steady state.

Dobson and Ruppertsberg (2007) constructed a theoretical simulation model of a square thermosyphon loop. This thermosyphon loop is a downsized version of a loop, which the authors proposed for use as a residual heat removal system for a nuclear reactor cavity. The physical layout of the scaled thermosyphon loop can be seen in Figure 7. The loop consists of a heating side, where heating plates transfer heat through convection and radiation to fins attached to the thermosyphon loop. The heat is conducted through the fins, through the pipe, and the working fluid is heated inside the pipe through internal convection. On the condenser side, a water tank is used to remove the heat from the working fluid. The loop also has an expansion tank connected to the bottom-right corner of the loop, and the mass flow rate is measured using a differential pressure transducer across an orifice plate on the bottom pipe.

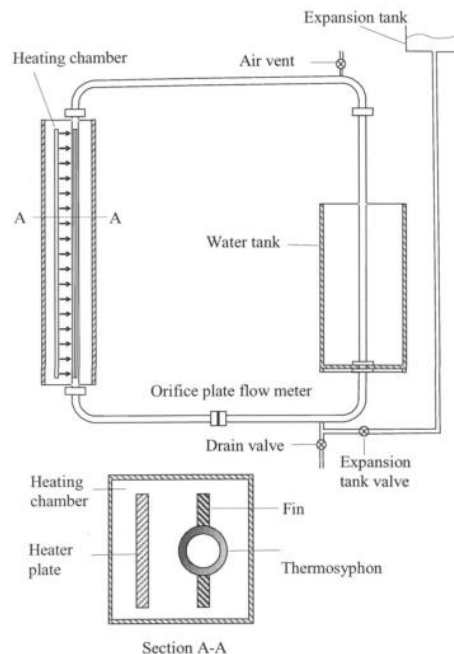


Figure 7 Schematic representation of a closed loop thermosyphon for a reactor cavity cooling system (Dobson & Ruppertsberg, 2007)

The simulation model was constructed by dividing the system into control volumes and applying the three conservation equations to them. Important assumptions are related to the Boussinesq approximation: The friction on the inner pipe wall is proportional to the instantaneous flow rate, the temperature of the vapour and fluid is equal across the cross-sectional area of the pipe, and the heat transfer rate between the fluid and the surrounding structure is determinable through the temperature difference. The Martinelli-Lockard void fraction was

used. Dobson and Ruppertsberg (2007) specifies three operating conditions for the loop, namely, a single phase, a two-phase flow, and an operating mode, which is referred to as a heat pipe mode, where the loop is only half-filled with working fluid.

Bird *et al.* (1960) used a shell balance approach to define the equations of change for the continuity equation (conservation of mass) given as

$$\left\{ \begin{array}{c} \text{Rate of} \\ \text{mass} \\ \text{accumulation} \end{array} \right\} = \left\{ \begin{array}{c} \text{Rate of} \\ \text{mass} \\ \text{in} \end{array} \right\} - \left\{ \begin{array}{c} \text{Rate of} \\ \text{mass} \\ \text{out} \end{array} \right\}$$

Applying this approach to a control volume and dividing by  $\Delta x \Delta y \Delta z$  gives (see Appendix A.1) for full derivation)

$$\frac{\partial \rho}{\partial t} = - \left( \frac{\partial}{\partial x} \rho v_x + \frac{\partial}{\partial y} \rho v_y + \frac{\partial}{\partial z} \rho v_z \right)$$

for the momentum equation, given that momentum balance equation is

$$\left\{ \begin{array}{c} \text{Rate of} \\ \text{momentum} \\ \text{accumulation} \end{array} \right\} = \left\{ \begin{array}{c} \text{Rate of} \\ \text{momentum} \\ \text{in} \end{array} \right\} - \left\{ \begin{array}{c} \text{Rate of} \\ \text{momentum} \\ \text{out} \end{array} \right\} + \left\{ \begin{array}{c} \text{Sum of forces} \\ \text{acting on} \\ \text{system} \end{array} \right\}$$

and applying it to the control volume and dividing by  $\Delta x \Delta y \Delta z$  gives (see Appendix A.2 for full derivation)

$$\begin{aligned} \frac{\partial}{\partial t} \rho v_x &= - \left( \frac{\partial}{\partial x} \rho v_x v_x + \frac{\partial}{\partial y} \rho v_y v_x + \frac{\partial}{\partial z} \rho v_z v_x \right) - \left( \frac{\partial}{\partial x} \tau_{xx} + \frac{\partial}{\partial y} \tau_{yx} + \frac{\partial}{\partial z} \tau_{zx} \right) \\ &\quad - \frac{\partial P}{\partial x} + \rho g_x \\ \frac{\partial}{\partial t} \rho v_y &= - \left( \frac{\partial}{\partial x} \rho v_x v_y + \frac{\partial}{\partial y} \rho v_y v_y + \frac{\partial}{\partial z} \rho v_z v_y \right) - \left( \frac{\partial}{\partial x} \tau_{xy} + \frac{\partial}{\partial y} \tau_{yy} + \frac{\partial}{\partial z} \tau_{zy} \right) \\ &\quad - \frac{\partial P}{\partial y} + \rho g_y \\ \frac{\partial}{\partial t} \rho v_z &= - \left( \frac{\partial}{\partial x} \rho v_x v_z + \frac{\partial}{\partial y} \rho v_y v_z + \frac{\partial}{\partial z} \rho v_z v_z \right) - \left( \frac{\partial}{\partial x} \tau_{xz} + \frac{\partial}{\partial y} \tau_{yz} + \frac{\partial}{\partial z} \tau_{zz} \right) \\ &\quad - \frac{\partial P}{\partial z} + \rho g_z \end{aligned}$$

for the total energy equation, given that the energy equation is

$$\left\{ \begin{array}{l} \text{Rate of} \\ \text{accumulation} \\ \text{of internal} \\ \text{and kinetic} \\ \text{energy} \end{array} \right\} = \left\{ \begin{array}{l} \text{rate of} \\ \text{internal and} \\ \text{kinetic energy} \\ \text{in} \\ \text{by convection} \end{array} \right\} - \left\{ \begin{array}{l} \text{rate of} \\ \text{internal and} \\ \text{kinetic energy} \\ \text{out} \\ \text{by convection} \end{array} \right\} +$$

$$\left\{ \begin{array}{l} \text{net rate of} \\ \text{heat addition} \\ \text{by conduction} \end{array} \right\} - \left\{ \begin{array}{l} \text{net rate of} \\ \text{work done by} \\ \text{system on} \\ \text{surroundings} \end{array} \right\}$$

Applying to a control volume and dividing by  $\Delta x \Delta y \Delta z$  gives the energy equation, in vector form for purposes of convenience, as (see Appendix A.3 for full derivation)

$$\frac{\partial}{\partial t} \rho (\hat{U} + 0.5v^2) = -(\Delta \cdot \rho \mathbf{v} (\hat{U} + 0.5v^2)) - (\nabla \cdot \mathbf{q}) + \rho (\mathbf{v} \cdot \mathbf{g}) - (\nabla \cdot p \mathbf{v})$$

$$- (\nabla \cdot [\boldsymbol{\tau} \cdot \mathbf{v}])$$

## 2.2 Mathematical model

This section will present the literature that contributed to the theoretical simulation model of the loop. The various authors and their methods will be discussed and considered.

Martinelli and co-workers did pioneering work in providing the first widely successful methods for predicting the frictional multiplier,  $\phi_l$  and the void fraction,  $\alpha$ . The methodology he used to develop these methods was based on a combination of semi-theoretical arguments and empirical evidence. Martinelli established a foundation on which modern, succeeding two-phase flow models have been built (Carey, 1992).

### 2.2.1 Separated two-phase flow void fraction

#### Homogeneous flow

The homogeneous flow model (friction factor model or fog flow model) is a special case of the separated flow analysis. The two-phase flow is treated as an equivalent single-phase flow, where the vapour and liquid phases are assumed to be perfectly mixed. The correlation between the quality of the fluid and the void fraction is given as



$$\alpha = \frac{x/\rho_v}{[(1-x)/\rho_l] + (x/\rho_v)} \quad (2.2)$$

The model also assumes the liquid and vapour velocities are equal over the cross-section (Carey, 1992). The friction for the flow can be determined by using a friction factor. Two common equations for the mean liquid viscosity are

$$\frac{1}{\bar{\mu}} = \frac{x}{\mu_v} + \frac{1-x}{\mu_l} \quad (2.3)$$

as proposed by McAdams *et al.* (1942), and

$$\bar{\mu} = x \mu_v + (1-x) \mu_l \quad (2.3)$$

as proposed by Cicchitti *et al.* (1960). The homogeneous density is defined as

$$\rho_h = \rho_g \alpha_h + \rho_l (1 - \alpha_h) \quad (2.4)$$

The homogeneous flow model is only accurate when  $\frac{\rho_l}{\rho_g} < 10$  (Whalley, 1897).

Separated flow model

Butterworth (1975) showed that several of the separated void fraction correlations can be related to a general form:

$$\alpha = \left[ 1 + B \left( \frac{1-x}{x} \right)^{n_1} \left( \frac{\rho_v}{\rho_l} \right)^{n_2} \left( \frac{\mu_l}{\mu_v} \right)^{n_3} \right]^{-1} \quad (2.5)$$

Table 1 shows the different correlation values or models and the different values for the constants B,  $n_1$ ,  $n_2$  and  $n_3$ .

Table 1 Separated void correlations and methods

Correlation or model	B	$n_1$	$n_2$	$n_3$
Homogeneous	1	1	1	0
Zivi (1964)	1	1	0.67	0
Wallis separate-cylinder model (Carey 1992)	1	0.72	0.4	0.08
Lockhart and Martinelli (1949)	0.28	0.64	0.36	0.07
Thom (1964)	1	1	0.89	0.18
Baroczy (1963)	1	0.74	0.65	0.13

Whalley (1897) suggests that the CISE correlation factor is the most accurate method for determining the void fraction (see Appendix A). Idsinga and Todreas (1977) did a study on 18 pressure drop and void fraction correlations and tested them on 2 200 experimental team-water measurements; they found that the correlations of Baroczy (1963) and Thom (1964) were the most accurate. Void fraction models are discussed in more detail in Section 3.2.1.

#### Frictional multiplier

Whalley (1897) suggests that the Friedel correlation is the most accurate for determining the frictional multiplier (see Appendix A). Idsinga and Todreas (1977) also concluded that the homogeneous model two-phase friction multiplier is the most accurate. Vijayan *et al.* (2000) assessed 14 pressure drop correlations and found that the Lockhart-Martinelli correlation was the most accurate. The frictional multiplier is discussed in more detail in Section 3.3.

#### 2.2.2 Two-phase flow internal heat transfer coefficient

The single-phase internal heat transfer convection coefficient can be determined as  $h_l = 3.66\left(\frac{k_l}{D}\right)$  for laminar flow and by applying the Dittus-Boelter equations  $h_l = 0.023Re^{0.8}Pr^{0.4}\left(\frac{k_l}{D}\right)$  for turbulent flow (Mills & Ganesan, 2015). Determining the single-phase internal heat transfer convection coefficient will be discussed in Section 3.5.1.

Saturated flow boiling occurs when the temperature of the working fluid becomes higher than the saturated temperature of the fluid at the corresponding pressure. When this happens, two heat transfer mechanisms are present in the working fluid inside the pipe, namely, nucleate boiling and liquid convection. When nucleate boiling is initiated, an abundance of active nucleation sites are present on the wall of the pipe. Because of this occurrence inside the pipe, the convection heat transfer cannot be used on its own to predict heat transfer from the wall of the

pipe to the working fluid. When the quality  $x$  of the fluid is low, the vapour void fraction  $\alpha$  is relatively low and the nucleate boiling mechanism dominates the convection heat transfer. The nucleate boiling mechanism must be taken into account when the working fluid separates into vapour and liquid phases. As the enthalpy increases, vapourisation occurs, resulting in the void fraction and pressure increasing, causing the mass flow rate to increase, resulting in a high convective heat transfer coefficient. The increase in heat transfer coefficient increases the working fluid temperature which increases the density gradient. When the fluid reaches annular flow and the liquid film becomes very thin, the nucleation is suppressed to convection heat transfer, which is, once again, the dominant mechanism (Carey, 1992).

Chen (1966) argues that two heat transfer coefficients need to be considered when determining the overall heat transfer coefficient for convective saturated boiling. These two heat transfer coefficients are the microscopic  $h_{mic}$  (nucleate boiling) and the macroscopic  $h_{mac}$  (bulk convective) coefficients need to be considered. Chen used a so-called compression factor  $S$  to correct the fully developed nucleate boiling prediction  $h_{mic}$  (see equations 2.6 and 2.7).

$$h_{mic} = 0.00122 \left[ \frac{k_l^{0.79} c_{pl}^{0.45} \rho_l^{0.4}}{\sigma^{0.5} \mu_l^{0.9} h_{lv}^{0.24} \rho_v^{0.24}} \right] [P_{sat}(T_{w,i}) - P_i]^{0.75} [T_{w,i} - T_{sat}(P_i)]^{0.24} S \quad (2.6)$$

$$h_{mac} = h_l F(X_{tt}) \quad (2.7)$$

Chen's correlation curves of the compression factor  $S$  and  $F(X_{tt})$  were later given empirical relations by Collier to Chen's original data (Carey, 1992). Equations (2.6) and (2.7) will be discussed in Section 3.5.2. Whalley (1897) suggests that the Chen correlation is more accurate than other correlations.

Shah (1984) used a different approach to Chen and calculated correlating values based on quality, mass flux and heat flux values. Shah's original correlating factors were presented in graph form, but was only given later as correlating equations. The problem with Shah's correlating factors is that they are limited to a small range of values and outside these values, the correlation can vary by 20%; furthermore, the correlation is limited to pipe diameter of 1.2 to 25.4 mm.

### Convective condensation

The Nusselt-type analytic approach can be adapted for convective condensation inside a round tube if the flow is downward and laminar, with no entrainment. Convective condensation occurs in many applications under annular flow conditions over much of the tube length (Carey, 1992). It will be shown in

Section 3.5.3 that the flow inside the downcomer is, in fact, annular flow, and when the cooling water is circulated through the condensers in the downcomer section of the pipe, the fluid succumbs to convective condensation. This occurs because the pipe wall temperature drops lower than the saturated temperature of the working fluid.

The Nusselt-type analytical approach needs a high level of computational effort, and accurate relations for the interfacial shear and entrainments of the system. There are more simple empirical solutions for calculating the convective heat transfer coefficient of the annular convective condensation. One of these relations, presented by Traviss *et al.* (1973), is similar to the Nusselt-type analytical approach and uses the Martinelli turbulent-turbulent parameter. Shah (1979) proposes a correlation based on empirical data for convective condensation in circular pipes. Soliman *et al.* (1968) proposes a correlation that includes the shear parameters for determining the transport. These correlations are all based on annular flow inside a horizontal pipe.

Chen *et al.* (1987) proposes a correlation equation for annular flow condensation in vertical tubes; this equation includes the effect of gravity, interfacial waves and interfacial shear, and is discussed in Section 3.5.3.

When the working fluid is in two-phase flow, the horizontal top pipe is assumed to have only stratified flow inside the pipe, due to the low mass flow rate of the working fluid. Carey (1992) proposes the work of Chanto, namely, a convective condensation equation for a horizontal plate, which Chanto adapted the equation for a horizontal pipe. This method is discussed in Section 3.5.4. Chanto's formula is also recommended by Mills and Ganesan (2015) and Whalley (1897).

## 2.3 Instabilities

This section will investigate the different instabilities of natural circulation loops reported by different authors, and discuss the conditions under which the instabilities occur.

Instabilities are undesirable in boiling, condensing and other two-phase flow processes. Instabilities can cause oscillations, which cause mechanical vibrations in the system; these vibrations can damage the physical structure and affects the control of the system. The oscillations also affect the heat transfer characteristics of the thermosyphon, which can cause burn-outs and dry-outs.

Boure *et al.* (1973) discussed, in detail, the different instabilities that can occur in a thermosyphon loop. There are two main types of instabilities, static and dynamic instabilities. Static instabilities involve a steady state system being disturbed, causing the system to return either to a different steady state condition, or to a periodic behaviour. Dynamic instabilities are instabilities that are caused by the inertia of the system and other feedback effects, which also cause oscillations.

The following static flow instabilities were identified by Boure *et al.* (1973). *Flow excursion* occurs when the flow rate reduces and the pressure in the system becomes lower than the pressure supplied to the system (in this case, the constant header tank pressure). *Fundamental relaxation* instability typically results in a periodic behaviour, usually when the flow is on the point of transition between flow regimes, usually the transition between bubbly flow and annular flow.

*Compound* relaxation instabilities involve bumping, geysering and chugging. Bumping occurs when the flow is in a region where the surface temperature fluctuates between natural convection and boiling, usually occurring when alkaline metals are boiled at low pressure and disappear at higher heat fluxes and pressures. Geysering occurs when the heat flux at the bottom of long vertical channels is very high, in a system with low pressure, where hydrostatic head changes and sudden vapour generation occurs, which leads to sudden vapour explosions from the channel. The liquid fills up again, the system returns to a sub-cooled, non-boiling state, and the cycle starts again. Chugging is the same as geysering and can go from small changes in flow rate to large busts of fluid.

Dynamic instabilities occur in the separated two-phase flow region, and can be divided into two categories: pressure (acoustic) and density (void) waves. *Acoustic* instabilities occur in a period of a pressure wave, which is the time it takes for the wave to travel through the system; these instabilities have been observed to oscillate at frequencies between 10 and 100 Hz and at flow regimes such as sub-cooled boiling, bulk boiling and film boiling. *Density* instability is oscillations with the period of the wave being the same as the time it takes a particle to travel through the system. This instability causes a disturbance in the heat transfer and pressure of the system.

### 3 TWO-PHASE FLOW AND HEAT TRANSFER THEORY

The theory used to develop the numerical model of the natural circulation cooling system will be discussed in this section. Figure 8 presents a simplified schematic drawing of the natural circulation loop and the discretisation of the loop into discrete control volumes. The three conservation laws (Section 3.7) were applied to these control volumes and are shown in Figure 9.

#### 3.1 Assumptions and equations of change

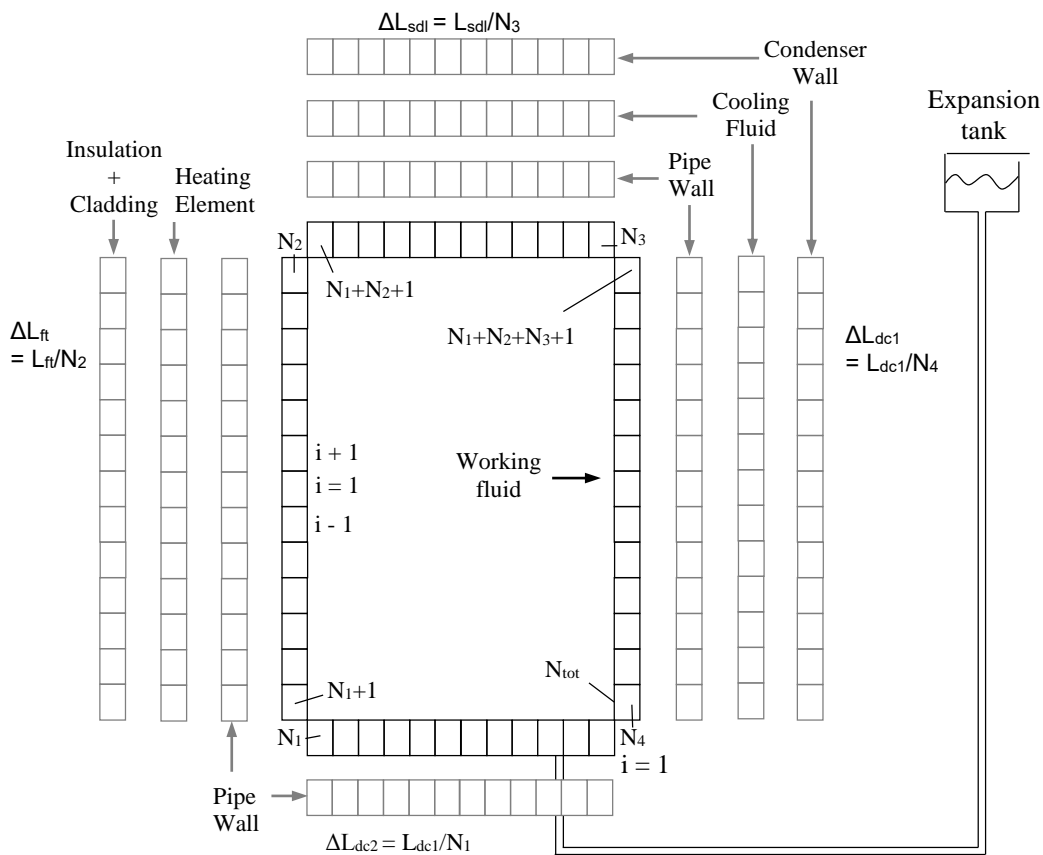


Figure 8 Discretisation scheme of the thermosyphon loop

The left-hand evaporator side of the loop was divided into four separated control volume sections: the working fluid; the pipe wall; the heating elements; and the cladding and insulation. The top and right-hand side condenser section was divided into four rows of control volumes: the working fluid; the pipe wall; the cooling fluid inside the condenser; and the wall of the condenser. The bottom horizontal pipe is open to the surroundings and is divided into control volumes for

the working fluid and the pipe wall. Each section was divided into a number of control volumes labelled from  $N_1$  to  $N_4$ . The size of the control volumes were determined by dividing the length of the section by the number of control volumes chosen. The numbering of the control volumes start at the right and corner and is labelled as the letter 'i'. (See Figure 8)

The following assumptions were made when the equations of change, conservation of mass, momentum and energy, were applied:

- The mass flow rate at any given point in the system can be calculated by  $\dot{m} = \rho v A$ ;  $v$  is the average velocity of the working fluid calculated from the volumetric flow  $v = \dot{V}/A$ ,  $A$  being the cross-sectional area, and  $\rho$  is density.
- The analysis of gas-liquid flow inside a tube is considered to be steadily one-dimensional and all dependent variables and properties are at ideal states and do not vary on the x-axis, but vary only on the z-axis.
- The system is assumed to be in quasi-static equilibrium, which implies that, at any instant in time, the flow in the circulation loop can be solved as steady. For a system to be quasi-static, the Strouhal number  $St = fL/V$  must be zero or smaller than one, where  $f$  is the characteristic frequency,  $L$  is the characteristic length, and  $V$  is the characteristic speed. The average fluid velocity must be considerably lower than the speed of sound for the system to be quasi-static, and  $\partial\dot{m}/\partial z = 0$  and  $\partial\dot{m}/\partial t \neq 0$  (Cengel & Cimbala, 2014).
- The liquid and gas phases are in thermal equilibrium at any point in the system on the cross-section; thus, both are at the same temperature (Carey, 1992).
- The expansion tank line with a diameter of 0.03 m and length of 27 m is small and long enough that it does not contribute to instantaneous pressure fluctuations inside the loop (Lee & Kim, 1999).
- A one-dimensional model is applied for heat transfer and fluid flow in both single- and two-phase regions, because of the ratio  $\left(\frac{D}{L}\right) < 1$  (Bieliński, 2016).
- Boussinesq approximation was valid for the working fluid; then, density is assumed to vary as  $\rho = \rho_0[1 - \beta(T - T_0)]$  in the gravity term (see Section 3.7.3) where  $\beta = \frac{1}{v} \left(\frac{\partial v}{\partial T}\right)_p$ , and  $v$  is specific volume and the subscript 0 is the reference steady state (Bieliński, 2016).

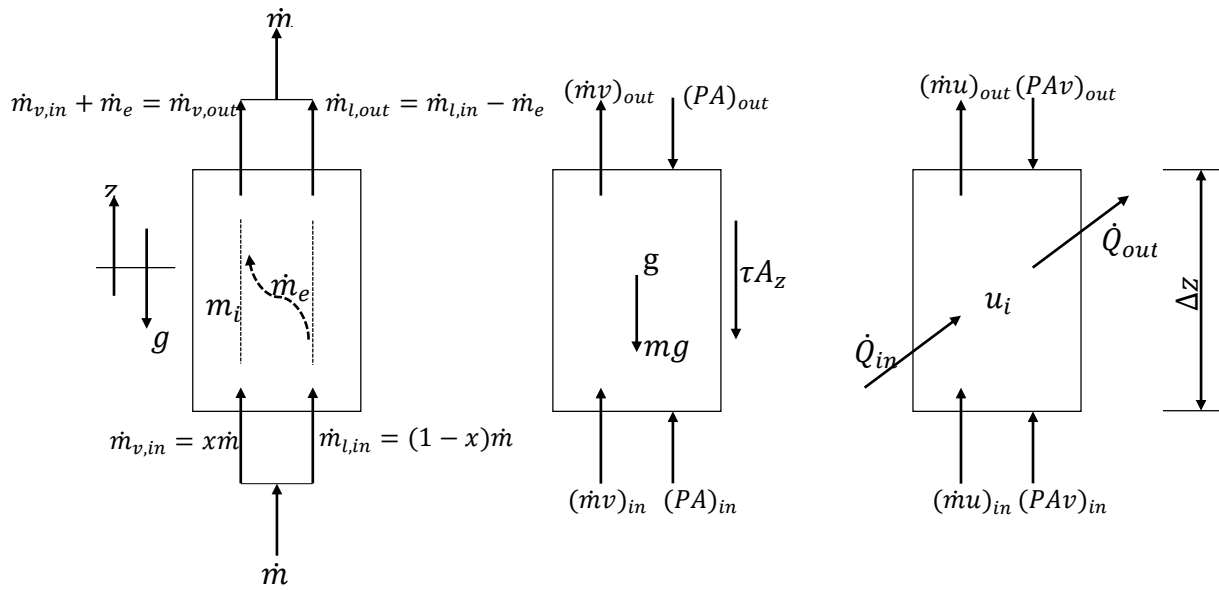


Figure 9 Conservation of mass (a), momentum (b), energy (c) as applied to a representative control volume with cross-sectional area  $A$ , area in contact with the pipe  $Az$  and length  $\Delta z$

The equations of change (conservation of mass, momentum and energy) and the property functions applied to the control volumes with the necessary assumption described in Section 3, as shown in equations 3.1, 3.2 and 3.3. These equations are derived in Appendix A.

$$\frac{\Delta m}{\Delta t} = \dot{m}_{in} - \dot{m}_{out} \quad (3.1)$$

$$\frac{\Delta}{\Delta t} (mu) = (\dot{m}u)_{in} - (\dot{m}u)_{out} + \dot{Q}_{in} - \dot{Q}_{out} + (PAv)_{in} - (PAv)_{out} - \tau_w A_z v \quad (3.2)$$

$$\frac{\Delta}{\Delta t} (mv) = (\dot{m}v)_{in} - (\dot{m}v)_{out} + (PA)_{in} - (PA)_{out} - m_i g \sin\theta - \tau_w A_z \quad (3.3)$$



## 3.2 Separated two-phase flow model

### 3.2.1 Separated two-phase flow Void fraction

When introducing separated flow, additional physical attributes, in addition to the single-phase attributes (viscosity, inertia and pressure forces), need to be taken into account. These attributes are interfacial tension forces, the wetting characteristic of the liquid on the tube wall, and the exchange of momentum between the liquid and vapour phases in the flow (Carey, 1992). Before describing the solution to these additional attributes, it helps to consider a simple two-phase flow, as shown in Figure 10.

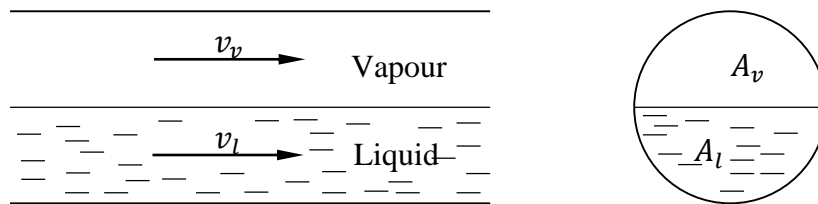


Figure 10 Illustration of an idealised one-dimensional model of separated “two-phase” flow inside a pipe

In this idealised example of a separated flow, the vapour and liquid phases are perfectly separated, vapour on top and liquid on the bottom. The total mass flow rate of this system is equal to the mass flow of the vapour  $\dot{m}_v$  and the mass flow of the liquid  $\dot{m}_l$ ,  $\dot{m} = \dot{m}_v + \dot{m}_l$ .

The ratio between the total flow of the system and the mass flow of vapour is called the quality, or the dryness factor, and is defined as

$$x = \frac{\dot{m}_v}{\dot{m}_v + \dot{m}_l} \quad (3.4)$$

The other portion of the ratio is known as the wetness factor:  $1 - x = \frac{\dot{m}_l}{\dot{m}}$ .

The specific internal energy  $u$  of the two-phase flow can be written in terms of the mass fraction (quality,  $x$ ), the specific internal energy of the vapour flow,  $u_v$  and the specific internal energy of the liquid flow,  $u_l$ , as

$u = xu_v + (1 - x)u_l$	(3.5)
-------------------------	-------

Similarly, for the specific heat (for homogeneous two-phase flow), at a constant volume and pressure, as

$$c = xc_v + (1 - x)c_l \quad (3.6)$$

where  $c_v$  is the specific heat of the vapour and  $c_l$  is the specific heat of the liquid.

The void fraction,  $\alpha$ , is defined as the ratio of the cross-sectional area that the vapour fills up to the total cross-sectional area, and is defined as

$$\alpha = \frac{A_v}{A_v + A_l} \quad (3.7)$$

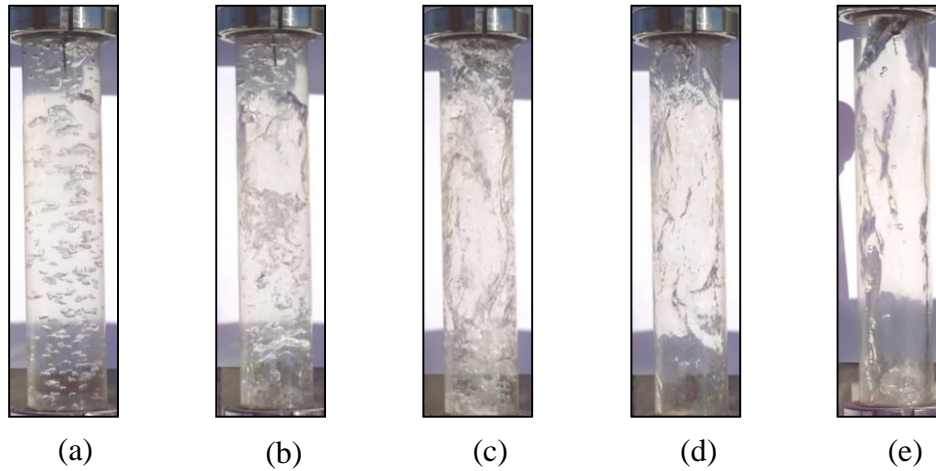
where  $A_v$  is the cross-sectional area of the vapour, and  $A_l$  is the cross-sectional area of the liquid. The void fraction can also be written in terms of the volumetric flow rates and in terms of the volumes, where

$$\alpha = \frac{V_v}{V_v + V_l} = \frac{\dot{V}_v}{\dot{V}_v + \dot{V}_l} \quad (3.8)$$

The density of the “two-phase” flow  $\rho$  can be written in terms of the void fraction, the density of the vapour,  $\rho_v$ , and the density of the liquid,  $\rho_l$ , as

$$\rho = \alpha\rho_v + (1 - \alpha)\rho_l \quad (3.9)$$

In Figure 10, the liquid and vapour phases are perfectly separated. This only happens in perfect conditions for a horizontal pipe. For a non-ideal co-current separated flow in a vertical pipe, the flow regime would be as illustrated in Figure 11, which is the flow regimes of the working fluid in the 27 m natural circulation loop, seen from the top left sight glass. The different flow patterns, shown from left to right, indicate the quality of the flow as it increases. The complexity of the flow regime causes problems for obtaining the void fraction of the fluid (Carey, 1992; Whalley, 1897).



(a) Bubbly flow, (b) Slug flow, (c) Churn flow, (d) Wispy-annular flow, (e) Annular flow

Figure 11 Flow regimes of the working gas-liquid flow inside the 27 m natural circulation loop observed through the top left sight glass

The void fraction for a non-idealised condition can be written as

$$\alpha = \left( 1 + \frac{v_v}{v_l} \frac{1-x}{x} \frac{\rho_v}{\rho_l} \right)^{-1} \quad (3.10)$$

For the homogeneous flow model, the two phases are seen as evenly mixed, where  $v_l = v_v$  and the slip factor,  $S = \frac{v_v}{v_l} = 1$  and the homogeneous void fraction is, thus,

$$\alpha = \left( 1 + \frac{1-x}{x} \frac{\rho_v}{\rho_l} \right)^{-1} \quad (3.11)$$

Butterworth (1975) shows that many of the void fraction models can be written in a general form, as

$$\alpha = \left[ 1 + B \left( \frac{1-x}{x} \right)^{n_1} \left( \frac{\rho_v}{\rho_l} \right)^{n_2} \left( \frac{\mu_l}{\mu_v} \right)^{n_3} \right]^{-1} \quad (3.12)$$

and the Lockhart-Martinelli void fraction can be written in terms of the Martinelli parameter,  $X_{tt}$ , as

$$\alpha = [1 + 0.28 X^{0.71}]^{-1} \quad (3.13)$$

which also contributes to Butterworth's notation. The Martinelli parameter,  $X_{tt}$ , will be discussed in Section 3.2.2.

The CISE correlation, given by Whalley (1897), uses the form of the void fraction in equation 3.5. The slip factor,  $S$ , is not taken to be 1 such as in the homogeneous model, but calculated using the Weber number and the Reynolds number, see Appendix A.6.

### 3.2.2 Martinelli parameter

Martinelli *et al.* (1949) defined a correlation factor called the Martinelli parameter, which is,

$$X = \left[ \frac{(dP/dz)_l}{(dP/dz)_v} \right]^{1/2} \quad (3.14)$$

where  $(dP/dz)_l$  is the pressure drop caused by friction for the liquid  $l$  phase flowing in the pipe and  $(dP/dz)_v$  is the pressure drop caused by friction for the vapour  $v$  phase flowing in the pipe. These terms derive from the conservation of momentum equation and are defined as

$$(dP/dz)_l = \frac{\tau_{rz} A_z}{A_x}; \quad (3.15)$$

$$(dP/dz)_v = \frac{\tau_{rz} A_z}{A_x} \quad (3.16)$$

where  $A_z$  is the shear area of the pipe for a dimensional cylindrical control volume with diameter  $d$  and length  $\Delta z$ , being  $\pi d \Delta z$ , and  $A_x$  is the cross-sectional area of the control volume defined as  $\pi d^2/4$ . The wall shear stress for liquid flow  $\tau_{rz}$  is defined as

$$(\tau_{rz})_l = (C_f)_l \rho_l \frac{(v_z^2)_l}{2} \quad (3.17)$$

and the shear stress for the vapour flow is defined as

$$\tau_{rz} = (C_f)_v \rho_v \frac{(v_z^2)_v}{2} \quad (3.18)$$

where  $C_f$  is the *fanning friction factor* and the *Darcy friction factor*,  $f = 4 C_f$  (Cengel & Cimbala, 2014). The fanning factor is defined as  $(C_f)_l =$

$B_l Re_l^{n_l}$ ;  $(C_f)_v = B_v Re_v^{n_v}$  where B is a Blasius-type coefficient of friction and  $B = 0.079$  and  $n = -0.25$  for both liquid and vapour at turbulent flow. The Reynolds number for the liquid is defined as

$$Re_l = \frac{(v_z)_l D_i \rho_l}{\mu_l} \quad (3.19)$$

and for the vapour phase

$$Re_v = \frac{(v_z)_v D_i \rho_v}{\mu_v} \quad (3.20)$$

where the velocity can be written in terms of the mass flow rate for convenience, which causes the velocity of the liquid-phase flow to be

$$(v_z)_l = \frac{(1-x)\dot{m}}{\rho_l \pi d^2/4} \quad (3.21)$$

and the velocity of the vapour-phase flow as

$$(v_z)_v = \frac{(1-x)\dot{m}}{\rho_v \pi d^2/4} \quad (3.22)$$

Substituting equation 3.17 into equation 3.15 gives

$$(dP/dz)_l = \frac{\tau_{rz} A_z}{A_x} = \frac{B \left( \frac{\left( \frac{(1-x)\dot{m}}{\rho_l \pi d^2/4} D_i \right) \rho_l}{\mu_l} \right)^n \frac{\left( \frac{(1-x)\dot{m}}{\rho_l \pi d^2/4} \right)^2}{2} \pi \rho_l D \Delta z}{\pi d^2/4} \quad (3.23)$$

and equation 3.18 into equation 3.16 gives

$$(dP/dz)_v = \frac{\tau_{rz} A_z}{A_x} = \frac{B \left( \frac{\left( \frac{(1-x)\dot{m}}{\rho_v \pi d^2/4} D_i \right) \rho_v}{\mu_v} \right)^n \frac{\left( \frac{(1-x)\dot{m}}{\rho_v \pi d^2/4} \right)^2}{2} \pi \rho_v D \Delta z}{\pi d^2/4} \quad (3.24)$$

Substituting equations 3.23 and 3.24 into equation 3.14 gives the Martinelli parameter for both phases flowing turbulently as

$$X_{tt} = \left(\frac{1-x}{x}\right)^{0.875} \left(\frac{\rho_v}{\rho_l}\right)^{0.5} \left(\frac{\mu_l}{\mu_v}\right)^{0.125} \quad (3.25)$$

The Martinelli parameter is used to statistically correlate experimental data and will be used in the next section (Carey, 1992).

### 3.3 Two-phase friction multiplier

Martinelli *et al.* (1949) suggest a correlation method for predicting the frictional pressure gradient in an adiabatic gas-liquid flow in a round tube. Their studies of adiabatic two-phase flow in horizontal tubes lead to the discovery of a two-phase multiplier,  $\Phi_l$  or  $\Phi_v$ .

Where the correlation is

$$\Phi_l = \left(1 + \frac{C}{X} + \frac{1}{X^2}\right)^{\frac{1}{2}} \quad (3.26)$$

And

$$\Phi_v = (1 + CX + X^2)^{\frac{1}{2}} \quad (3.27)$$

and  $X$  is the Martinelli parameter as discussed in Section 2.1. The Reynolds number is used to determine the constant,  $C$ , which depends on the flow regimes of the vapour and liquid respectively (see Table 2 2). Liquid flow in a round tube is laminar when  $Re_l < 2000$  and for turbulent  $Re_l > 2000$ ; similar values can be used for  $Re_v$ , where

$$Re_l = \frac{v(l-x)D_i\rho_l}{\mu_l} \quad (3.28)$$

And

$$Re_v = \frac{v(x)D_i\rho_v}{\mu_v} \quad (3.29)$$

Table 2 Correlation of constant C and Reynolds numbers for friction multiplier

Liquid	Gas	C
$Re_l > 2000$	$Re_v > 2000$	20
$Re_l < 2000$	$Re_v > 2000$	12
$Re_l > 2000$	$Re_v < 2000$	10
$Re_l < 2000$	$Re_v < 2000$	5

The two-phase wall shear stress,  $\tau_{rz}$ , may now be defined as

$$\tau_s = \tau_{rz} \Phi_{lo}^2 \quad (3.30)$$

where the two-phase flow liquid-only frictional multiplier is defined as

$$\Phi_{lo}^2 = \Phi_l^2 (1 - x)^{1.75}$$

The Friedel correlation, given by Whalley (1897), determines the frictional multiplier with the Weber, Froude and Reynolds numbers, and the formula is repeated for convenience below (see Appendix A.7 for full description).

$$\phi_{lo}^2 = E + \frac{3.24 F H}{Fr^{0.045} We^{0.035}} \quad (3.31)$$

The homogeneous flow model also has a simple version of the frictional multiplier, which is determined as

$$\phi_{lo}^2 = \frac{\rho_l}{\rho} \quad (3.32)$$

where  $\rho_l$  is the liquid-only density, and the combined density of the fluid and the liquid is  $\rho$ .

### 3.4 Minor losses

The thermosyphon loop has additional components that interrupt the flow and cause flow separation and mixing. Components, such as bends, elbows, tees, inlets, exits, expansions and contractions, can cause pressure losses additional to the straight pipe frictional loss. These losses are called minor losses, because they are very small compared to head loss (major losses). The minor losses could

become greater than the major losses in some systems, when there is an abundance of the components mentioned (Cengel & Cimbala, 2014).

Batty and Folkman (1983) give a method for determining the minor losses in which is calculated in the form of an equivalent pipe length; thus, the minor losses are equal to the loss incurred by adding an additional length of pipe to the system,  $L_{eq}$ . Table 3 summarises the different minor loss components that were identified in the system, their loss coefficients and their equivalent pipe lengths. The equivalent length is determined using the equivalent length over the diameter ratio,  $L_{eq}/D_i$ .

Table 3 Minor loss components identified and their equivalent lengths

Nature of resistance	Number of occurrences	$k$	$L_{eq}/D_i$	Equivalent length $L_{eq}$ [m]
Elbow	4	2.2	32	6.144
Tee (flow-over)	6	0.5	16	4.608
Sudden contraction	1	0.39	12	0.576
Sudden enlargement	1	0.83	12	0.576
Total				11.904 m

The total equivalent length of the minor losses was added to the total length of the system and divided by the number of control volumes, increasing each control volume's length slightly when calculating the frictional loss.

### 3.5 Heat transfer coefficient

#### 3.5.1 Single-phase heat transfer coefficient

The heat transfer from the working fluid to the pipe wall is calculated by determining heat transfer coefficient, which is calculated using a Nusselt number. Mills and Ganesan (2015) give the Nusselt number for laminar flow ( $Re < 3000$ ) inside a pipe as

$$Nu_D = 3.66 \quad (3.33)$$



Gnielinski (1976) proposes the following equation for determining the Nusselt number,  $Nu_d$ , for fully developed turbulent flow ( $Re > 3000$ ) inside a round tube as,

$$Nu_D = \frac{(f/8) (Re_D^{0.8} - 1000) Pr}{1 + 12.7 (f/8)^{0.5} (Pr^{\frac{2}{3}} - 1)} \quad (3.34)$$

where the Prandtl number  $Pr$  is given as

$$Pr = \frac{c_p \mu}{k} \quad (3.35)$$

where  $c_p$  is the specific heat,  $\mu$  is the dynamic viscosity of the fluid, and  $k$  is the thermal conductivity of the working fluid. The Reynolds number  $Re_D$  of the working fluid is given as

$$Re_D = \frac{v D_i \rho}{\mu} \quad (3.36)$$

where  $v$  is the working fluid velocity,  $D_i$  is the internal pipe diameter,  $\rho$  is the working fluid density and  $\mu$  is the working fluid dynamic viscosity. Petukhov (1970) gives the friction coefficient  $f$  for a smooth wall pipe as

$$f = (0.79 \ln Re_D - 1.64)^{-2} \quad (3.37)$$

where  $Re_D$  is the Reynolds number of the working fluid.

The Nusselt number  $Nu_D$ , thermal conductivity of the working fluid  $k$ , and internal diameter of the pipe  $D_i$ , can be used to determine the heat transfer coefficient of the working fluid given by Mills and Ganesan (2015) as

$$h_i = \frac{Nu_D k}{D_i} \quad (3.38)$$

### 3.5.2 Evaporator heat transfer coefficient

Saturated flow boiling occurs when the working fluids' temperature is higher than the saturation temperature of the corresponding working fluid pressure. When this happens, both vapour and liquid are present, hence, the term two-phase flow. The presence of the vapour changes the flow, from simple convection heat transfer to more complex heat transfer, which changes with the quality ( $x$ ) and void fraction ( $\alpha$ ) of the working fluid.

The flow development discussed above requires a heat transfer coefficient that accommodates nucleate-pool-boiling-like conditions, which occur at low quality of the working fluid and the transition to a higher quality when pure film evaporation occurs (Carey, 1992). Chen (1966) proposes a coefficient of heat transfer correlation that accounts for the transition from nucleate boiling to film evaporation effects in a system. He argues that the convection heat transfer coefficient is  $h_i = h_{mic} + h_{mac}$ , where  $h_{mic}$  is a “microscopic” heat transfer coefficient for nucleate boiling, and  $h_{mac}$  is a “macroscopic” heat transfer coefficient. The macroscopic heat transfer coefficient is taken as

$$h_{mac} = h_l F(X_{tt}) \quad (3.39)$$

where the liquid convection coefficient  $h_l$  is taken as the Dittus-Boeltler correlation, given as

$$h_l = 0.023 \left( \frac{k_l}{D_i} \right) Re_l^{0.8} Pr_l^{0.4} \quad (3.40)$$

where  $k_l$  is the conduction coefficient of the liquid-only working fluid,  $D_i$  is the diameter of the internal pipe,  $Pr_l$  is the Prandtl number of the liquid-only working fluid, and the liquid Reynolds number is,

$$Re_l = \frac{v(l-x)D_i\rho}{\mu_l} \quad (3.41)$$

where  $v$  is the velocity of the working fluid,  $D_i$  is the diameter of the inner pipe,  $\rho$  is the density of the working fluid,  $x$  is the quality of the bulk fluid and  $\mu$  is the dynamic viscosity. The function,  $F$ , is taken as the curvetted equation, which Collier (Carey, 1992) proposed from Chen’s (1966) original correlation curves, and is given as,

$$F(X_{tt}) = 2.35 \left( 0.213 + \frac{1}{X_{tt}} \right)^{0.736} \quad (3.42)$$

where  $X_{tt}$  is the Martenelli parameter defined as

$$X_{tt} = \left( \frac{1-x}{x} \right)^{0.9} \left( \frac{\rho_v}{\rho_l} \right)^{0.5} \left( \frac{\mu_l}{\mu_v} \right)^{0.1} \quad (3.43)$$

where  $x$  is the quality of the working fluid,  $\rho_l$  is the liquid-only density of the working fluid,  $\rho_v$  is the vapour-only density of the working fluid,  $\mu_l$  is the liquid-only dynamic viscosity of the working fluid, and  $\mu_v$  is the vapour-only dynamic viscosity of the working fluid.

The microscopic heat transfer coefficient is taken as

$$h_{mic} = 0.00122 \left[ \frac{k_l^{0.79} c_{pl}^{0.45} \rho_l^{0.4}}{\sigma^{0.5} \mu_l^{0.9} h_{lv}^{0.24} \rho_v^{0.24}} \right] [P_{sat}(T_{w,i}) - P_i]^{0.75} [T_{w,i} - T_{sat}(P_i)]^{0.24} S \quad (3.44)$$

where  $k_l$  is the conduction coefficient of the liquid,  $\mu_l$  is the dynamic viscosity of the liquid,  $\rho_v$  is the density of the vapour,  $\rho_l$  is the density of the liquid,  $Cp_l$  is the specific heat of the liquid,  $\sigma$  is the interfacial tension, and  $\sigma = F(T_i)$ . The saturation temperature for water is  $P_{sat}(T_{w,i})$  at the wall temperature of the pipe,  $P_i$  is the working fluid pressure,  $T_{sat}(P_i)$  is the saturation temperature of water at the pressure of the working fluid, and  $T_{w,i}$  is the wall temperature of the pipe.  $S$  is called the suppression factor and is also curve fitted by Collier (Carey, 1992) and is given as

$$S = (1 + 2.56 \cdot 10^{-6} Re_{tp}^{1.17})^{-1} \quad (3.45)$$

where the Reynolds number  $Re_{tp}$  is taken as

$$Re_{tp} = Re_l F^{1.25}$$

where  $Re_l$  is the liquid-only Reynolds number and is shown in equation 3.19, and the function  $F$  is shown in equation 3.42. The liquid-vapour convection coefficient  $h_{lv}$  is taken as

$$h_{lv} = 0.023 \left( \frac{k_l}{D_i} \right) Re_{lv}^{0.8} Pr_l^{0.4} \quad (3.46)$$

where  $k_l$  is the conduction coefficient of the liquid-only working fluid,  $D_i$  is the diameter of the internal pipe,  $Pr_l$  is the Prandtl number of the liquid-only working fluid, and  $Re_{lv}$  is the liquid-vapour Reynolds number taken as

$$Re_{lv} = \frac{v D_i \rho}{\mu} \quad (3.47)$$

where  $v$  is the velocity of the working fluid,  $D_i$  is the diameter of the inner pipe,  $\rho_i$  is the density of the working fluid, and  $\mu_i$  is the dynamic viscosity.

### 3.5.3 Condenser vertical side heat transfer coefficient

When the cooling fluid is activated inside one of the condensers along the vertical wall, condensation will be present, because of the temperature difference between

the pipe wall and the cooling fluid. The sight glass on the vertical condensation pipe shows that an annular flow is present inside the tube when the fluid is in the two-phase flow region (see Figure 12, where the liquid is flowing down the side of the pipe wall and collects at the bottom). Different heat transfer coefficients, which accommodate annular flow and condensation, are discussed in Section 2.2. A simple heat transfer model that does not need reliable closure relations of the interfacial shear and entrainment, was chosen to determine the convective heat transfer coefficient for the vertical pipe condenser section.



Figure 12 Right-hand side vertical pipe sight glass indicating annular flow

Traviss *et al.* (1973) propose the following annular-flow convective condensation heat transfer coefficient:

$$h = \frac{0.15 Pr_l Re_l^{0.9}}{FT} \left[ \frac{1}{X_{tt}} + \frac{2.85}{X_{tt}^{0.476}} \right] \quad (3.48)$$

where  $Pr_l$  is the liquid-only Prantl number, and the Martinelli parameter,  $X_{tt}$ , and the liquid-only Reynolds number,  $Re_l$ , are given by equation 2.11 and equation 2.9 respectively.  $FT$  is given by

$$FT = 5 Pr_l + 5 \ln\{1 + 5 Pr_l\} + 2.5 \ln(0.0031 Re_l^{0.812}) \quad (3.49)$$

for  $Re_l > 1125$  and

$$FT = 5 Pr_l + 5 \ln\{1 + Pr_l (0.0964 Re_l^{0.585} - 1)\} \quad (3.50)$$

for  $50 < Re_l < 1125$  and

$$FT = 0.707 Pr_l Re_l^{0.585} \quad (3.51)$$

or  $5 > Re_l$ .

### 3.5.4 Top horizontal pipe heat transfer coefficient

When observing the horizontal top pipe flow regime through the sight glass, it is clear that, for most of the time, the flow is stratified, see Figure 13. Stratified flow is observed when the liquid flows in the bottom of the pipe and the vapour is separated and flows on the top portion of the pipe. This usually occurs with low flow rates and high quality of the working fluid (Carey, 1992). When stratified flow occurs, a portion of the pipe is not covered in the liquid phase, and condensation will occur when the condenser's cooling fluid is switched on and the wall temperature of the pipe is below the saturated temperature of the working fluid. According to Carey (1992), the heat transfer in the liquid is negligible when convection condensation is present, and only the heat transfer through the condensation layer is calculated.

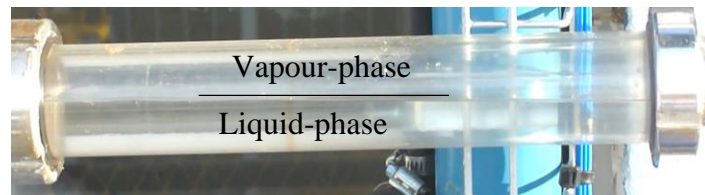


Figure 13 Top horizontal tube sight glass indicating stratified flow (vapour at top and liquid at the bottom)

Chato (Carey, 1992) gives a modified Nusselt analysis equation for a horizontal plate as

$$Nu = 0.728 Kc \left[ \frac{g \rho_l (\rho_l - \rho_v) D_i^3 h'_{fg}}{\mu_l k_l (T_{sat} - T_w)} \right]^{1/4} \quad (3.52)$$

where  $g$  is the gravitational acceleration,  $\rho_l$  is the density of the liquid,  $\rho_v$  is the density of the vapour,  $D_i$  is the inner diameter of the pipe,  $\mu_l$  is the viscosity of the liquid,  $k_l$  is the thermal conductivity of the liquid,  $(T_{sat} - T_w)$  is the temperature difference between the fluid saturation temperature and the pipe wall, and the enthalpy of vaporisation plus sub cooling correction is given as

$$h'_{fg} = h_{fg} + 0.5 c_v (T_w - T_{sat}) \quad (3.53)$$

where  $h_{fg}$  is the enthalpy of vaporisation,  $c_v$  is the specific heat and  $(T_w - T_{sat})$  the temperature difference between the wall and saturation temperature.

Jaster and Kosky (1976) suggest a simplified relation for predicting the void fraction and determining the Kc value as

$$Kc = \alpha^{-3/4} \quad (3.54)$$

with the void fraction,

$$\alpha = \left[ 1 + \left( \frac{1-x}{x} \right) \left( \frac{\rho_v}{\rho_l} \right) \right]^{-1} \quad (3.55)$$

with  $x$  being the quality.

### 3.5.5 Condenser static and active cooling water

There are multiple co-current heat exchangers (condensers) placed along the top horizontal and right vertical pipes of the thermosyphon loop. When these condensers are not in use, a body of water is still present inside the condenser that surrounds these pipes. The Raleigh number  $Ra_{ccw}$  is used to determine if the stationary cooling fluid is transferring heat by means of conduction or convection. Circulation occurs when the  $Ra_{ccw} > 0$ ; however, it is still seen as pure conduction when  $Ra_{ccw} < 1000$ ; for any value above 1000 a convection coefficient needs to be determined for the heat transfer. Natural convection is also present when aspect  $\frac{H}{L} > 10$ , where  $L$  is the distance between the succeeding vessel walls and  $H$  the height of the vessel. The Rayleigh number is given as,

$$Ra_{ccw} = \frac{g(T_{ccw} - T_{ccw})(t_{ws})^3 \rho_{ws}}{\mu_{ccw}} Pr_{ccw} \quad (3.56)$$

where  $(T_{ccw} - T_{ccw})$  is the temperature difference between the pipe wall and the condenser wall,  $t_{ws}$  is the distance between the succeeding vessel walls,  $\mu_{ccw}$  is the dynamic viscosity of the water in the water sleeve,  $\rho_{ccw}$  is the density of the water in the water sleeve,  $g$  is the gravitation acceleration, and  $Pr_{ccw}$  the Prantl number of the water (Mills & Ganesan, 2015).

The Nusselt number with equation 3.38 is used to determine the convective heat transfer coefficient. Cengel and Ghajar (2012) give the Nusselt number  $Nu_{ccw}$  for a vertical annulus as

$$Nu_{ccw} = 0.046 * Ra_{ccw}^{0.333} \quad (3.57)$$

and Mills and Ganesan (2015) give the Nusselt number for a horizontal annulus as

$$Nu_{ccw} = 0.069 * Ra_{ccw}^{0.333} * Pr_{ccw}^{0.074}. \quad (3.58)$$

When the condenser cooling water is activated the water is circulated by means of the constant header tank situated above the thermosyphon loop. The cooling water is cooled by means of a cooling tower and pumped back to the constant header tank. Because of the cooling tower the cooling fluid which enters the condenser was assumed to be the same temperature as the surrounding temperature. The thermal energy equation was used to determine the internal energy of the cooling water. It was assumed that reversible and irreversible work was negligible when determining the internal energy of the cooling water. Thus the thermal energy equation can be written explicitly as

$$u_i^{t+\Delta t} = [(mu)_i^t + \Delta t ((\dot{m}u)_{in} - (\dot{m}u)_{out} + \dot{Q}_{in} - \dot{Q}_{out})_i^t] / m_i^{t+\Delta t} \quad (3.59)$$

The condensers are tube-in-tube counter current heat exchanger, so the cooling fluid circulates in the opposite direction as the working fluid.

### 3.6 Heat transfer

In this section, the heat transfer from the elements to the working fluid will be discussed. The heat loss of the system will also be shown. A sectional view of the left-hand side vertical pipe and its thermal resistance diagram is presented in Figure 14. The sectional view of the vertical section shows the working fluid, pipe wall, electrical heating element, insulation and cladding.

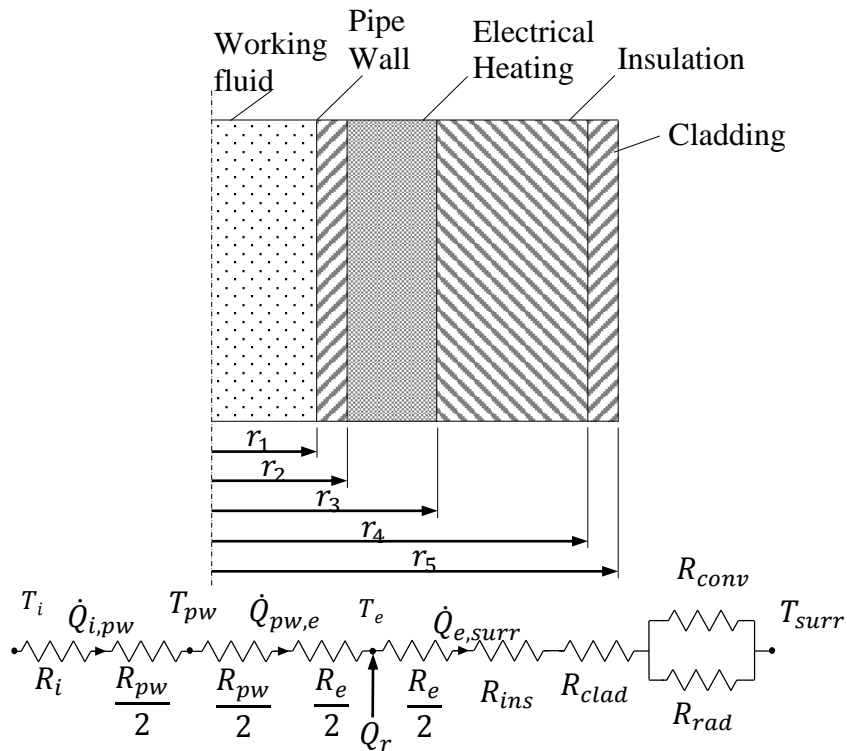


Figure 14 Heat transfer representation of the left-hand electric heating element side of the loop

The heat transfer rate  $\dot{Q}_{i,pw}$  from the internal circulation fluid to the pipe wall as depicted in Figure 14 is,

$$\dot{Q}_{i,pw} = \frac{T_i - T_{pw}}{\left(R_i + \frac{R_{pw}}{2}\right)} \quad (3.60)$$



where  $(T_i - T_{pw})$  is the temperature difference between the working fluid and the pipe wall, and  $R_{pw}$  is the thermal resistance of the pipe wall, which is conduction across a cylindrical shell (Mills & Ganesan, 2015),

$$R_{pw} = \frac{\log \frac{r_2}{r_1}}{k_{pw} * L * \pi * 2} \quad (3.61)$$

where  $\log \frac{r_2}{r_1}$  is the natural logarithm of the inner and outer radius of the pipe wall,  $k_{pw}$  is the thermal conductivity of the pipe wall, and  $L$  the length of the pipe wall.

Mills and Ganesan (2015) give the thermal resistance of the internal circulation fluid as

$$R_{piwc} = \frac{1}{h_i * AZ_{ipw}} \quad (3.62)$$

where  $AZ_{ipw}$  is the inner pipe wall area, and  $h_i$  is the heat transfer coefficient of the working fluid as described in Section 3.5.3.

The heat transfer rate  $\dot{Q}_{pw,e}$  from the wall to the electrical heating element, as depicted in Figure 14, is,

$$\dot{Q}_{pw,e} = \frac{T_e - T_{pw}}{\left(\frac{R_e}{2} + \frac{R_{pw}}{2}\right)} \quad (3.63)$$

where  $(T_i - T_{pw})$  is the temperature difference between the pipe wall and the electrical heating element, and  $R_{pw}$  is the same thermal resistance as in equation 2.60. The thermal resistance of the heating element  $R_e$  is conduction across a cylindrical shell and is derived in Appendix A.4 and given for convenience as,

$$R_e = \frac{\log \frac{r_3}{r_2}}{k_e * L * \pi * 2} \quad (3.64)$$

where  $\log \frac{r_3}{r_2}$  is the natural logarithm of the inner and outer radius of the heating element,  $k_e$  is the thermal conductivity of the electrical heating element, and  $L$  is the length of the heating element.

The heat transfer rate  $\dot{Q}_{e,surr}$  from the electrical heating element to the surroundings, as depicted in Figure 15, is,

$$\dot{Q}_{e,surr} = \frac{T_{amb} - T_e}{(R_{ins} + R_{clad} + \frac{R_e}{2} + R_{eq,rc})} \quad (3.65)$$

where  $(T_{surr} - T_e)$  is the temperature difference between the electrical heating elements and the surrounding temperature, and  $R_e$  is the same thermal resistance as in equation 3.64. The thermal resistances for the insulation  $R_{ins}$  and the cladding  $R_{clad}$  are both conduction across a cylindrical shell,

$$R_{clad} = \frac{\log \frac{r_5}{r_4}}{k_{clad} * L * \pi * 2} \quad (3.66)$$

where  $\log \frac{r_5}{r_4}$  is the natural logarithm of the inner and outer radius of the cladding material,  $k_{clad}$  is the thermal conductivity of the cladding material, and  $L$  the length of the cladding. The thermal resistance of the insulation  $R_{ins}$  is given as,

$$R_{ins} = \frac{\log \frac{r_4}{r_3}}{k_{ins} * L * \pi * 2} \quad (3.67)$$

where  $\log \frac{r_4}{r_3}$  is the natural logarithm of the inner and outer radius of the insulation material,  $k_{ins}$  is the thermal conductivity of the insulation material, and  $L$  the length of the insulation.

$R_{eq,rc}$  from equation 3.65 is the equivalent thermal resistance of the convection on the outer cladding wall and the radiation on the outer cladding wall,

$$R_{eq,rc} = \frac{1}{\frac{1}{R_{rad}} + \frac{1}{R_{conv}}} \quad (3.68)$$

where the thermal resistance for the air is,

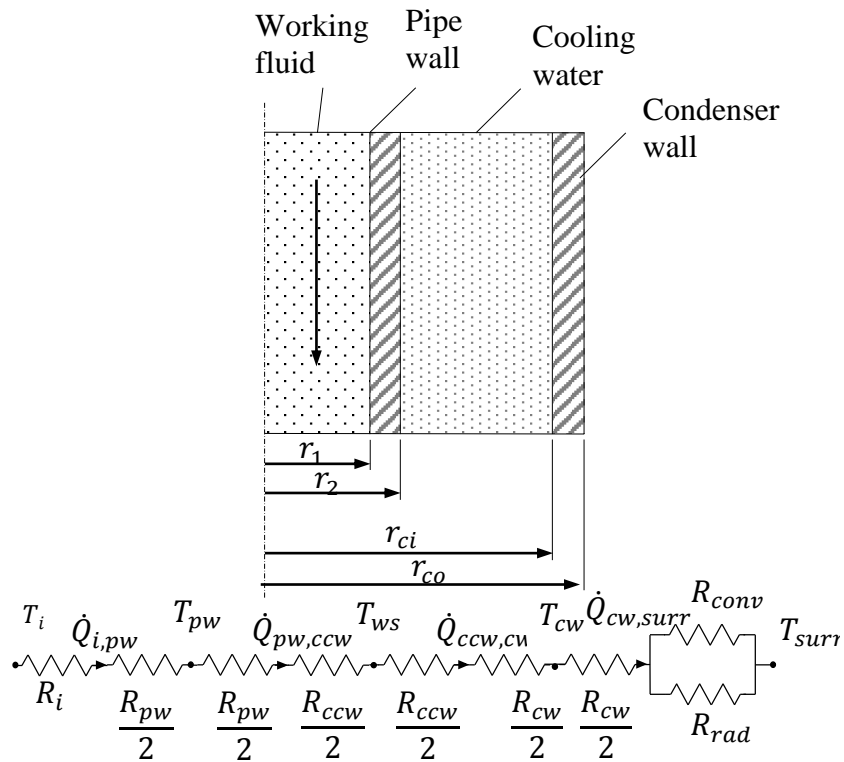
$$R_{rad} = \frac{1}{h_{oc} * Az_{clad}} \quad (3.69)$$

and the thermal resistance for the radiation is,

$$R_{conv} = \frac{1}{h_{or} * Az_{clad}} \tag{3.70}$$

where  $Az_{clad}$  is the outside area of the cladding wall and  $h_{oc}$  is the convection coefficient of air and equivalent convection coefficient for the heat transfer from radiation is given by Mills and Ganesan (2015) as  $h_{or} = 0.53h_{oc}$ .

A sectional view of the top and right-hand side section and its thermal resistance diagram is presented in Figures 15 and 16. The sectional view of these sections includes the working fluid, pipe wall, condenser cooling water and the condenser wall. In the top section of the loop, the fluid moves horizontally and, on the right-



hand side, the fluid moves vertically.

Figure 15 Heat transfer representation of the right-hand condenser side of the loop

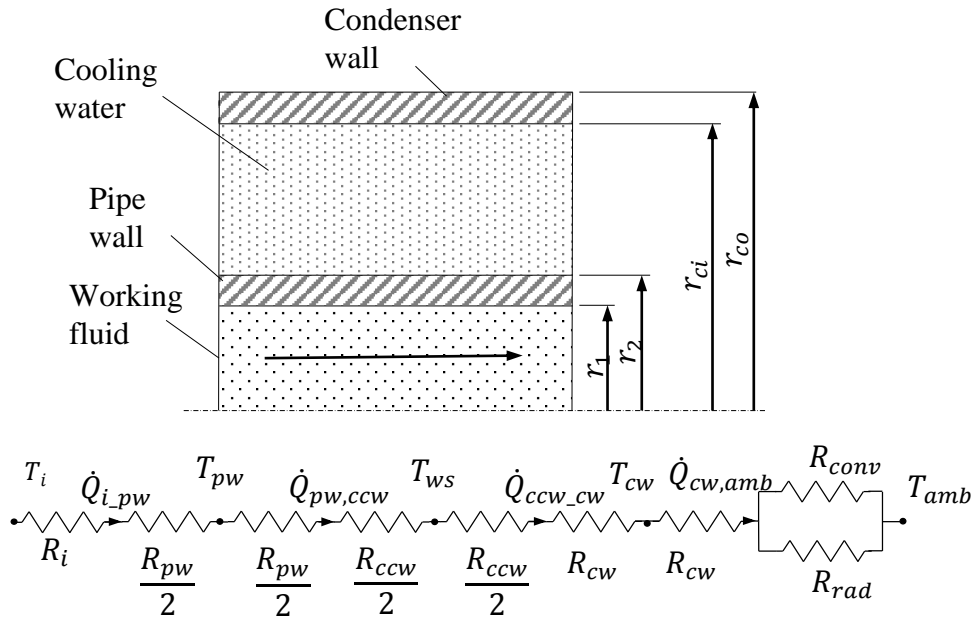


Figure 16 Heat transfer representation of the top condenser of the loop

The heat transfer rate,  $\dot{Q}_{i,pw}$ , from the internal circulation fluid to the pipe wall as depicted in Figure 15 and Figure 16 is determined using equation 3.59.

The heat transfer rate,  $\dot{Q}_{pw,ccw}$ , from the pipe wall to the condenser cooling water, as depicted in Figure 15 and Figure 16 is determined using,

$$\dot{Q}_{pw,ccw} = \frac{T_{ccw} - T_{pw}}{\left(\frac{R_{ccw}}{2} + \frac{R_{pw}}{2}\right)} \quad (3.71)$$

where  $(T_{ccw} - T_{pw})$  is the temperature difference between the pipe wall and the condenser cooling water.  $R_{pw}$  is determined using equation 3.60. The thermal resistance of the condenser cooling water is determined using,

$$R_{ccw} = \frac{1}{h_{ccw} * AZ_{ccw}} \quad (3.72)$$

where  $AZ_{ws}$  is the area of the pipe wall and the heat transfer coefficient,  $h_{ws}$  (this is described in Section 3.5).

The heat transfer rate,  $\dot{Q}_{ccw,cw}$ , from the pipe wall to the condenser cooling water, as depicted in Figure 15 and Figure 16 is determined as,

$$\dot{Q}_{ccw,cw} = \frac{T_{cw} - T_{ccw}}{\left(\frac{R_{ws}}{2} + \frac{R_{cw}}{2}\right)} \quad (3.73)$$

where  $(T_{cw} - T_{ccw})$  is the temperature difference between the water sleeve and the condenser wall, and  $R_{ccw}$  is determined using equation 3.72. The thermal resistance of the condenser wall is conduction across a cylindrical shell, and is determined using,

$$R_{cw} = \frac{\log \frac{r_{co}}{r_{ci}}}{k_{cw} * L * \pi * 2} \quad (3.74)$$

where  $\log r_{co}/r_{ci}$  is the natural logarithm of the inner and outer radius of the insulation material,  $k_{cw}$  is the thermal conductivity of the condenser wall, and  $L$  is the length of the condenser wall.

The heat transfer rate,  $\dot{Q}_{cw,surr}$ , from the condenser wall to the surroundings as depicted in Figure 15 and Figure 16 is determined using,

$$\dot{Q}_{cw,surr} = \frac{T_{surr} - T_{cw}}{\left(\frac{R_{cw}}{2} + R_{eq,rc}\right)} \quad (3.75)$$

where  $(T_{surr} - T_{cw})$  is the temperature difference between the condenser wall and the surrounding temperature. The thermal resistance of the condenser wall,  $R_{cw}$ , is determined using equation 3.74, and  $R_{eq,rc}$  is determined using equation 3.68.

A sectional view of the bottom section of the thermosyphon loops and its thermal resistance diagram is presented in Figure 17. The sectional view shows the working fluid and the pipe wall.

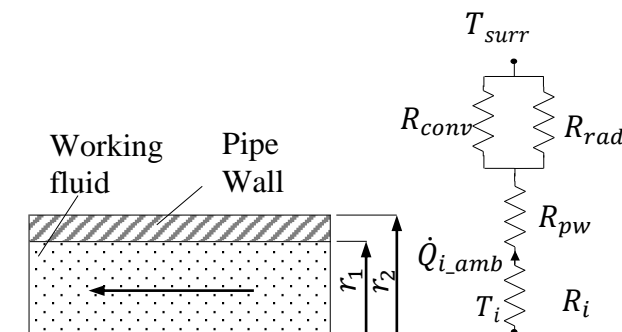


Figure 17 Heat transfer representation of the bottom of the loop

The heat transfer rate,  $\dot{Q}_{i,pw}$ , from the circulation fluid to the surrounding, as depicted in Figure 17 is determined using equation 3.59, and  $\dot{Q}_{pw,surr}$  is calculated as

$$\dot{Q}_{pw,surr} = \frac{T_{pw} - T_{surr}}{\left(\frac{R_{pw}}{2} + R_{eq,rc}\right)} \quad (3.76)$$

where  $T_{pw}$  is the temperature of the pipe wall,  $T_{surr}$  the temperature of the surroundings,  $R_{pw}$  is calculated using equation 3.60 and  $R_{eq,rc}$  is calculated using equation 3.68.

Thermal capacity of structure

The physical structure of the thermosyphon loop has a big effect on the working fluid. When the heating elements are turned on, the heat is transferred to the working fluid, but heat is also transferred into the rigid structure of the thermosyphon loop before it is lost to the environment. The heat that the structure of the natural circulation loop attains is called the *thermal capacity* of the system. The thermal capacity is calculated for the following parts of the system: the stainless steel piping, the heating elements, the stationary condenser cooling fluid, and the condenser wall. The heat capacity is written in terms of specific internal energy,  $u$ ; the equation is derived in Appendix A.4 and is shown here for convenience:

$$u^{t+\Delta t} = u^t + \Delta t (\dot{Q}_{in} - \dot{Q}_{out})/m \quad (3.77)$$

where  $u^{t+\Delta t}$  is the new specific internal energy,  $u^t$  is the current specific internal energy,  $(\dot{Q}_{in} - \dot{Q}_{out})$ , is the difference between the heat transfer entering the control volume and the heat transfer leaving the control volume,  $\Delta t$  is the time step, and  $m$  is the mass of the material.

The pipe wall specific internal energy,  $u_{pw}$ , in the evaporator section (see Figure 14), is calculated as,

$$u_{pw}^{t+\Delta t} = u_{pw}^t + \Delta t (\dot{Q}_{pw,e} - \dot{Q}_{i,pw})/m_{pw} \quad (3.78)$$

where  $m_{pw}$  is the mass of the pipe wall,  $\dot{Q}_{i,pw}$  is the heat transfer from the pipe wall to the working fluid (equation 3.59) and  $\dot{Q}_{pw,e}$  is the heat transfer from the electrical element to the pipe wall (equation 3.62).

The pipe wall specific internal energy,  $u_{pw}$ , in the condenser sections (see Figures 15 and 16) is calculated as,

$$u_{pw}^{t+\Delta t} = u_{pw}^t + \Delta t (\dot{Q}_{i,pw} - \dot{Q}_{pw,ccw})/m_{pw} \quad (3.79)$$

where  $m_{pw}$  is the mass of the pipe wall,  $\dot{Q}_{pw,ccw}$  is the heat transfer from the pipe wall to the condenser cooling fluid (equation 3.71) and  $\dot{Q}_{i,pw}$  is the heat transfer from the working fluid to the pipe wall (equation 2.59).

The pipe wall specific internal energy,  $u_{pw}$ , in the horizontal bottom section where the pipe is open to the surroundings (see Figure 17), is calculated as,

$$u_{pw}^{t+\Delta t} = u_{pw}^t + \Delta t (\dot{Q}_{i,pw} - \dot{Q}_{pw,surr})/m_{pw} \quad (3.80)$$

where  $m_{pw}$  is the mass of the pipe wall,  $\dot{Q}_{pw,surr}$  is the heat transfer from the pipe wall to the surroundings (equation 3.76) and  $\dot{Q}_{i,pw}$  is the heat transfer from the working fluid to the pipe wall (equation 3.59).

The heating element's internal specific energy,  $u_e$ , is calculated as

$$u_e^{t+\Delta t} = u_e^t + \Delta t (\dot{Q}_{pw,e} - \dot{Q}_{e,surr} + \dot{Q}_r)/m_e \quad (3.81)$$

where  $m_e$  is the mass of the electrical element,  $\dot{Q}_{e,surr}$  is the heat transfer from the heating element to the surroundings (equation 3.65) and  $\dot{Q}_{pw,e}$  is the heat transfer from the pipe wall to heating element (equation 3.62), and  $\dot{Q}_r$  is the internally generated heat from the heating element that is switched on.

The condenser static cooling water's internal energy,  $u_{ccw}$ , is calculated as

$$u_{ccw}^{t+\Delta t} = u_{ccw}^t + \Delta t (\dot{Q}_{pw,ccw} - \dot{Q}_{ccw,cw})/m_{ccw} \quad (3.82)$$

where  $m_{ccw}$  is the mass of the static condenser cooling water,  $\dot{Q}_{pw,ccw}$  is the heat transfer from the pipe wall to the static condenser cooling water (equation 3.71), and  $\dot{Q}_{ccw,cw}$  is the heat transfer from the static condenser cooling water to the condenser wall (equation 3.73).

The specific internal energy of the condenser wall,  $u_{cw}$  is calculated as

$$u_{cw}^{t+\Delta t} = u_{cw}^t + \Delta t (\dot{Q}_{ccw,cw} - \dot{Q}_{cw,surr})/m_{cw} \quad (3.83)$$

where  $m_{cw}$  is the mass of the condenser wall,  $\dot{Q}_{ccw,cw}$  is the heat transfer from the condenser cooling water to the condenser wall (equation 3.73) and  $\dot{Q}_{cw,surr}$  is the heat transfer from the condenser wall to the surroundings (equation 3.75).

### 3.7 Equations of change used numerically

#### 3.7.1 Conservation of mass

The conservation of mass equation with the quality is given as

$$\frac{\Delta m}{\Delta t} = \dot{m}_{in} - \dot{m}_{out} \quad (3.84)$$

where the two-phase mass and mass flow rate can be written as

$$m = m_v + m_l = xm + (1 - x)m \quad (3.85)$$

And

$$\dot{m} = \dot{m}_v + \dot{m}_l = x\dot{m} + (1 - x)\dot{m} \quad (3.86)$$

respectively.

The density of the liquid can be written in terms of the void fractions, as

$$\rho = \alpha\rho_v + (1 - \alpha)\rho_l. \quad (3.87)$$

The conservation of mass equation can be written explicitly as

$$m_i^{t+\Delta t} = m_i^t + \Delta t(\dot{m}_{in} - \dot{m}_{out})_i^t \quad (3.88)$$

#### 3.7.2 Conservation of energy

The thermal energy equation was derived from the conservation of energy equation in Appendix A.3, and is given as

$$\frac{\Delta}{\Delta t}(mu) = (\dot{m}u)_{in} - (\dot{m}u)_{out} + \dot{Q}_{in} - \dot{Q}_{out} + (PAv)_{in} - (PAv)_{out} - \tau_w A_z v \quad (3.89)$$



The thermal energy equation can be written explicitly as

$$\begin{aligned}
 u_i^{t+\Delta t} = & [(mu)_i^t \\
 & + (\dot{m}u)_{in} - (\dot{m}u)_{out} + \dot{Q}_{in} - \dot{Q}_{out} + (PA v)_{in} \\
 & - (PA v)_{out} - \tau_w A_z v]_{i^{t+\Delta t}} // m_i^{t+\Delta t}
 \end{aligned} \tag{3.90}$$

For a separated flow model, where the quality, void fraction and frictional multiplier are introduced, the equations are somewhat more elaborate. The left-hand term in equation 3.89 becomes,

$$\begin{aligned}
 \frac{\Delta}{\Delta t} (mu) &= \frac{\Delta}{\Delta t} (m_v u_v + m_l u_l) \\
 &= \frac{\Delta}{\Delta t} (m(xu_v + (1-x)u_l))
 \end{aligned} \tag{3.91}$$

where  $u = xu_v + (1-x)u_l$

The reversible work terms on the right-hand side of equation 3.89 become,

$$\begin{aligned}
 (PA v)_{in} - (PA v)_{out} &= (P(A_v v_v + A_l v_l))_{in} - (P(A_v v_v + A_l v_l))_{out} \\
 &= \left[ P \left( \alpha A \frac{x\dot{m}}{\rho_v \alpha A} + (1-\alpha) A \frac{(1-x)\dot{m}}{\rho_l (1-\alpha) A} \right) \right]_{in} \\
 &\quad - \left[ P \left( A_v \frac{x\dot{m}}{\rho_v \alpha A} + A_l \frac{(1-x)\dot{m}}{\rho_l (1-\alpha) A} \right) \right]_{out} \\
 &= \dot{m} \left[ \left( P \left( \frac{x}{\rho_v} + \frac{1-x}{\rho_l} \right) \right)_{in} - \left( P \left( \frac{x}{\rho_v} + \frac{1-x}{\rho_l} \right) \right)_{out} \right] \\
 &= \dot{m} \left[ (P/\rho_h)_{in} - (P/\rho_h)_{out} \right]
 \end{aligned} \tag{3.92}$$

where  $\rho_h = (x/\rho_v + (1-x)/\rho_l)^{-1}$ .

The convective energy flow terms on the right-hand side become,

$$\begin{aligned}
 &(\dot{m}u)_{in} - (\dot{m}u)_{out} \\
 &= x\dot{m}u_{v,in} + (1-x)\dot{m}u_{l,in} - x\dot{m}u_{v,out} - (1-x)\dot{m}u_{l,out} \\
 &= \dot{m}(u_{in} - u_{out})
 \end{aligned} \tag{3.93}$$

The irreversible work done on the fluid as a result of the friction term on the right-hand side may be given as

$$-\tau_w A_z v = -\tau_{lo} \phi_{lo}^2 A_z v \quad (3.94)$$

The friction  $\tau_w$  and the liquid-only frictional multiplier  $\phi_{lo}^2$  are discussed in Sections 3.2.2 and 3.3. The heat transfer into and out of the control volume,  $(\dot{Q}_{in} - \dot{Q}_{out})$ , is discussed in Section 3.5.

### 3.7.3 Conservation of momentum

To simplify the equation, the momentum equation (equation 2.3) was divided by the cross-sectional area of the control volume. This results in all the pressure interfaces cancelling out. The equation was also written in terms of the mass flow rate ( $v = \dot{m}/\rho A$ ), rather than velocity, which is beneficial when using it to sum the momentums over a number of adjacent control volumes. The equation then becomes,

$$\begin{aligned} \frac{\Delta}{\Delta t} \left( \frac{m\dot{m}}{A\rho} \right) &= \left( \frac{\dot{m}^2}{A\rho} \right)_{in,i} - \left( \frac{\dot{m}^2}{A\rho} \right)_{out,i} + (P)_{in,i} - (P)_{out,i} \\ &\quad - \rho_i g \sin \theta_i - \frac{\tau A_z}{A} \end{aligned} \quad (3.95)$$

The mass of each control volume can be written as  $m = \rho A \Delta z = (\alpha \rho_v + (1 - \alpha) \rho_l) A \Delta z$ , and inserting the frictional multiplier,  $\phi^2$ , the momentum equation becomes,

$$\begin{aligned} \frac{\Delta}{\Delta t} \left[ \frac{m\dot{m}}{A^2} \left( \frac{x^2}{\alpha \rho_v} + \frac{(1-x)^2}{(1-\alpha) \rho_l} \right) \right]_i \\ = \frac{\dot{m}^2}{A} \left[ \left( \frac{x^2}{\alpha A \rho_v} + \frac{(1-x)^2}{(1-\alpha) A \rho_l} \right)_{in} - \left( \frac{x^2}{\alpha A \rho_v} + \frac{(1-x)^2}{(1-\alpha) A \rho_l} \right)_{out} \right] \\ + [P_{in} - P_{out}]_i - [(\alpha \rho_v + (\alpha - 1) \rho_l) g \Delta z \sin \theta]_i - \left[ \frac{\tau_{lo} \Phi_{lo}^2 A_z}{A} \right]_i \end{aligned} \quad (3.96)$$

The first term on the right-hand side (momentum flux term), in accordance with the upwind differencing method, the “in” =  $i - 1$ , when the mass flow rate is positive (clockwise), “in” =  $i + 1$ , when the mass flow is negative (counterclockwise). The “out” will always be equal to “out” =  $i$ . The sign of the gravity term (second term from left) is accounted for by multiplying  $g$  by  $\sin \theta$ , where  $\theta$  is the angle the control volume makes with the horizontal axis. The top and bottom control volumes  $\theta = 0$ , for the left-hand side control volumes  $\theta = -\pi/2$  and for the right-hand side control volumes  $\theta = \pi/2$ . The mass flow rate of the system is then calculated by summing all the control volumes, from  $N = 1$  to  $N_{tot}$  at time step  $t$ . The pressure terms of the momentum equation cancel out, because of the static pressure head and the symmetry of the loop. The momentum equation can be written explicitly as,

$$\begin{aligned}
\dot{m}^{t+\Delta t} &= \dot{m}^t \sum_{i=1}^{N_{tot}+1} \left[ \frac{m_i^t}{A_i^2} \left( \left( \frac{x^2}{\alpha \rho_v} \right)_i + \left( \frac{(1-x)^2}{(1-\alpha)\rho_l} \right)_i \right) \right] \\
&+ \Delta t \left( \dot{m}^2 \sum_{i=1}^{N_{tot}+1} \left[ \frac{1}{A_i} \left( \left( \frac{x^2}{\alpha A \rho_v} + \frac{(1-x)^2}{(1-\alpha)A \rho_l} \right)_{in} - \left( \frac{x^2}{\alpha A \rho_v} + \frac{(1-x)^2}{(1-\alpha)A \rho_l} \right)_{out} \right) \right]_i \right. \\
&- \sum_{i=1}^{N_{tot}+1} [(\alpha \rho_v + (1-\alpha)\rho_l)g \sin \theta \Delta z]_i^t - \sum_{i=1}^{N_{tot}+1} \left[ \frac{\tau_{lo} \phi_{lo}^2 \rho (\Delta z + \Delta z_{minor})}{A} \right]_i \\
&\left. / \sum_{i=1}^{N_{tot}+1} \left[ \frac{m_i^{t+\Delta t}}{A_i^2} \left( \left( \frac{x^2}{\alpha \rho_v} \right)_i^{t+\Delta t} + \left( \frac{(1-x)^2}{(1-\alpha)\rho_l} \right)_i^{t+\Delta t} \right) \right] \right) \quad (3.97)
\end{aligned}$$

where  $\Delta z_{minor}$  is the equivalent length of pipe for the minor losses, which is discussed in Section 3.4.

In the instance where boussinesq approximation is not used the pressure is calculated after the mass flow rate. Rearranging equation 3.96, the control volume pressure may now be determined at the  $t + \Delta t$  as

$$\begin{aligned}
P_{out,i} &= P_{in,i} + \frac{\dot{m}^2}{A} \left[ \left( \frac{x^2}{\alpha A \rho_v} + \frac{(1-x)^2}{(1-\alpha)A \rho_l} \right)_{in,i} - \left( \frac{x^2}{\alpha A \rho_v} + \frac{(1-x)^2}{(1-\alpha)A \rho_l} \right)_{out,i} \right] \\
&- [(\alpha \rho_v + (1-\alpha)\rho_l)g \sin \theta \Delta z]_i - \left[ \frac{\tau_{lo} \phi_{lo}^2 \rho (\Delta z + \Delta z_{minor})}{A} \right]_i \\
&- \frac{1}{\Delta t} \left[ \left[ \frac{m}{A^2} \left( \frac{x^2}{\alpha \rho_v} + \frac{(1-x)^2}{(1-\alpha)\rho_l} \right) \right]_i^{t+\Delta t} - \left[ \frac{m}{A^2} \left( \frac{x^2}{\alpha \rho_v} + \frac{(1-x)^2}{(1-\alpha)\rho_l} \right) \right]_i^t \right] \quad (3.98)
\end{aligned}$$

### 3.8 Property functions and external inputs

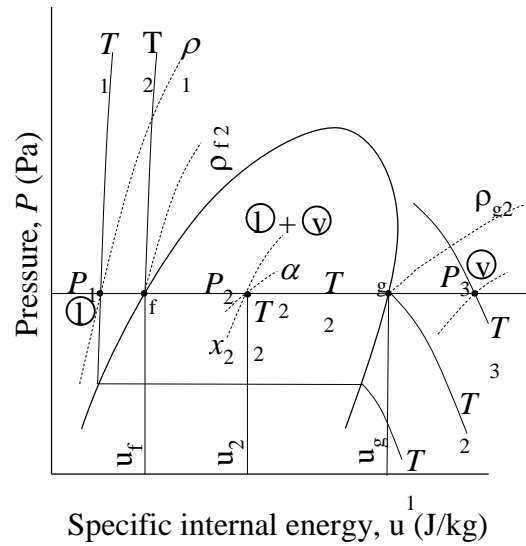


Figure 18 Pressure-specific internal energy diagram showing a sub-cooled liquid 1, a two-phase vapour plus liquid 2 and a vapour 3 (Senda, 2018)

The properties functions used for the numerical algorithm are shown in Appendix C.1 and were determined in terms of the specific internal energy  $u$  and the pressure of the control volume  $P$ , as seen in Figure 18. The properties could be divided into three regions, subcooled, two-phase and superheated. For the subcooled region, where  $x \leq 0$  and  $\alpha = 0$ , where  $x$  is defined as,

$$x = \frac{u - u_f}{u_g - u_f} \text{ and void fraction, } \alpha, \text{ is determined by equation 3.13,}$$

$$u = f(T), T = f(u, P), \rho = f(u, P)$$

For the subcooled region where  $0 < x < 1$  and  $0 < \alpha < 1$  the properties are,

$$u_f = f(P), u_g = f(P), T_{sat} = f(P), \rho_f = f(P), \rho_g = f(P)$$

the property functions for the superheated region where  $x \geq 1$  and  $\alpha \geq 1$  is,

$$T = f(u, P), \rho = f(u, P)$$

The Stellenbosch weather station was used to collect the surrounding temperature,  $T_{surr} = f(t)$  data for each of the days and times the experiments were conducted. This temperature was used to give real time temperature changes to the theoretical simulation model, to ensure more accurate results. (Journée & Meijers, 2018)

### 3.9 Mathematical model procedure

Figure 19 shows the sequence of steps that was followed by the mathematical simulation model. The main steps include the input of the initial conditions values, determining the specific internal energy, and calculating the mass flow rate. The mathematical program uses an upwind differencing scheme, where the mass of the control volumes is predicted by using the gradient of the current at the previous time steps, see appendix B for the full simulation program.

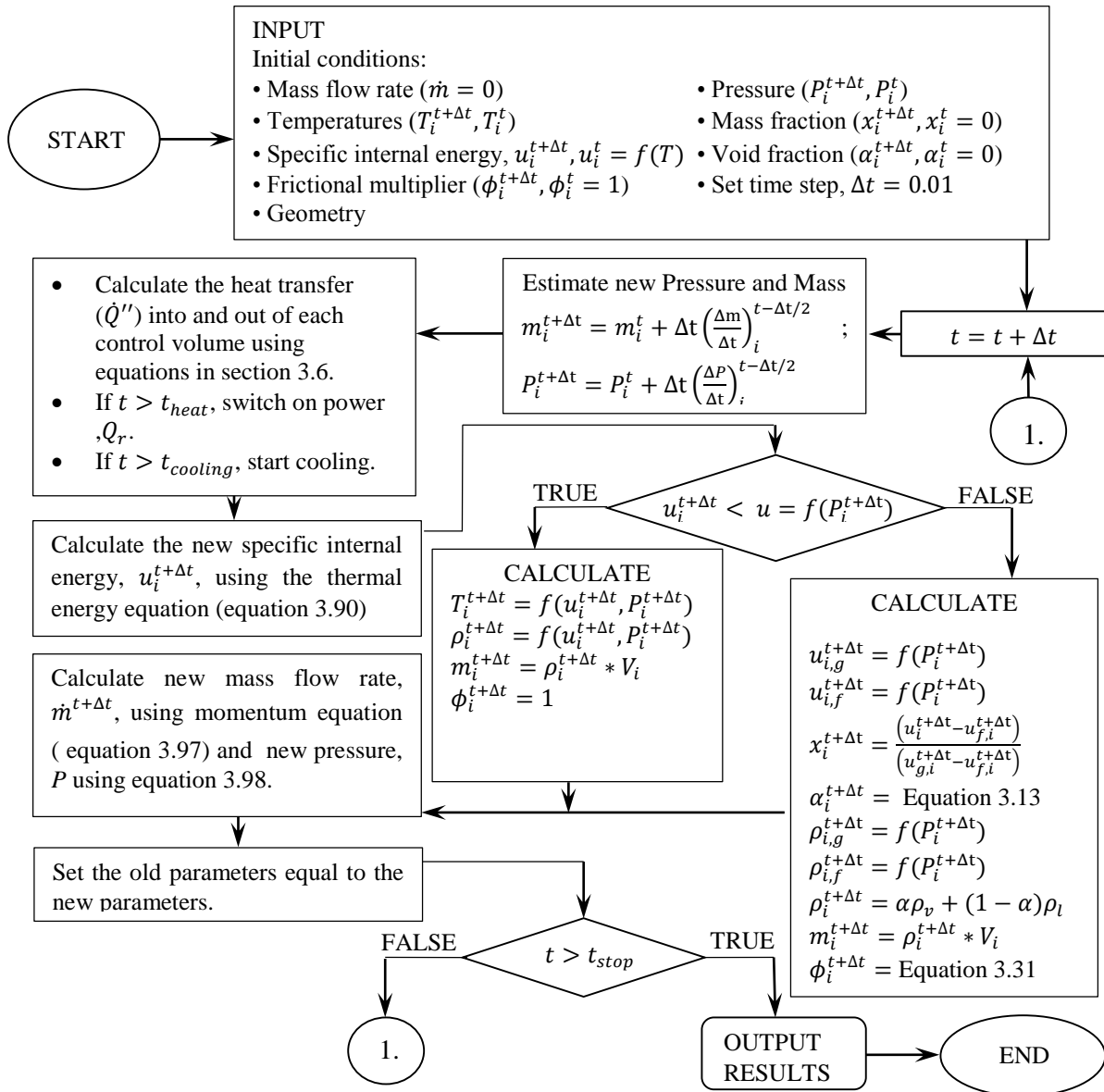


Figure 19 The sequence of steps followed by the mathematical model to predict the flow of the working fluid

## 4 EXPERIMENTAL SETUP

In this section, the experimental setup of the 27 m high cooling system will be explained with reference to the operating conditions for working the system. The instruments used to measure the experimental data will be explained, and the calibration of these instruments are shown in Appendix E.

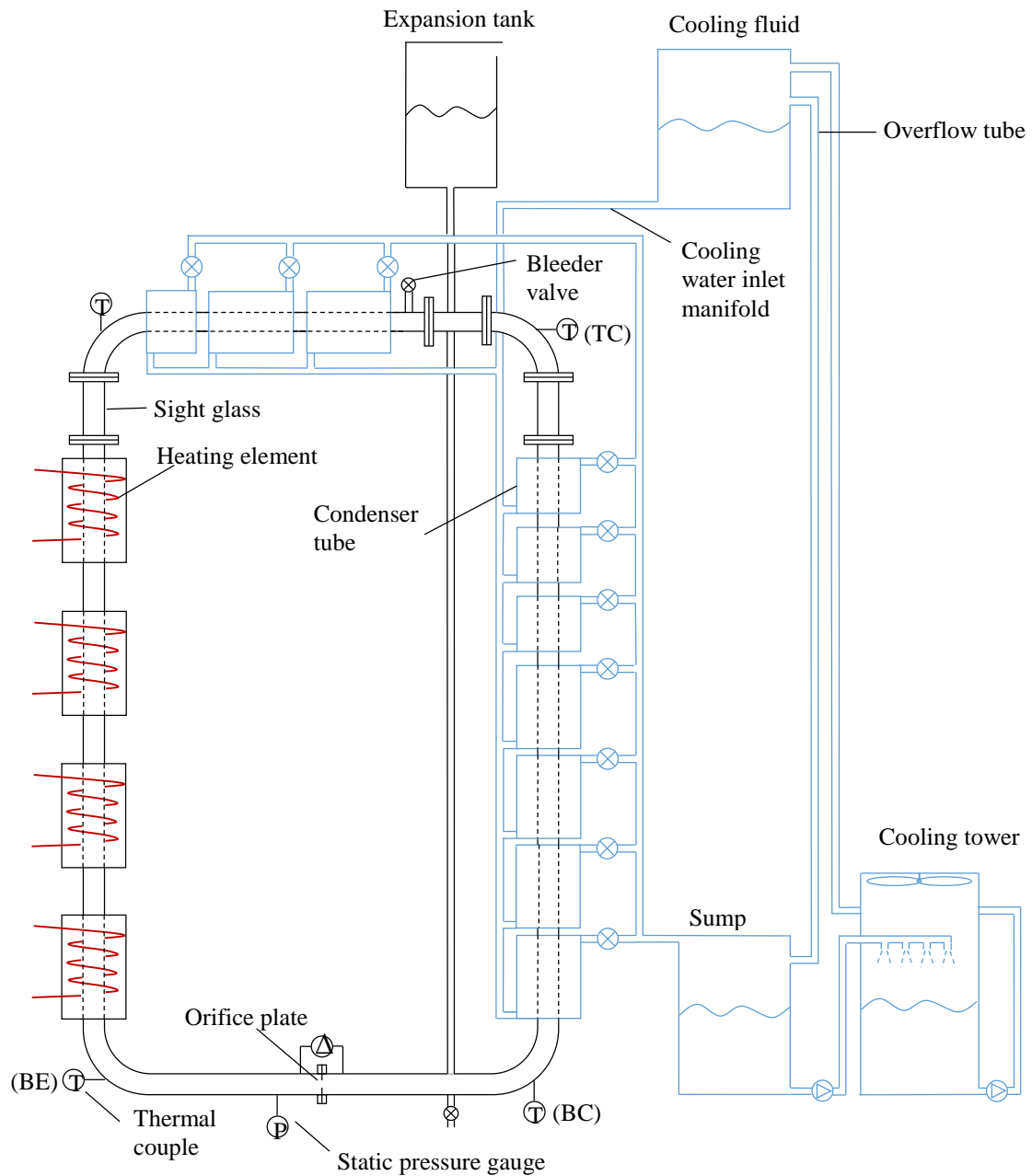


Figure 20 Illustration of the 27 x 6 m natural circulation loop with the cooling system

## 4.1 Geometry and materials

The experimental setup consists of a 27 m x 6 m full-size rectangular natural circulation loop. The loop is constructed of stainless steel (304-grade) pipes that have a diameter of 50.8 mm. At the top of the loop, in the right-hand corner, and on the top left corner of the loop, three polycarbonate sight glass tubes of 300 mm in length were inserted to inspect the flow visually (see Figure 20). A 250 L polypropylene expansion tank, which is open to the atmosphere, is connected to the natural circulation loop, to ensure that pressure buildup does not occur inside the loop. The expansion tank is connected at the bottom right of the loop, the tank is placed approximately 28 m from the ground and is open to the atmosphere.

On the left-hand side of the loop, on the vertical pipe, 25 resistance heating elements are clamped; these heating elements give a total of 17.5 kW at 240 V power. The heating elements are fully insulated with a ceramic fibre blanket (U-Therma 6, density 120 kg/m<sup>3</sup>) 50 mm thick, with a layer of cladding on the outside (see Figure 14 for illustration of sectional view of heating element insulation). The heating elements are divided into four banks of six heating elements each and one bank of two heating elements. Each bank is controlled as a unit.

On the top horizontal tube and right vertical tube of the loop, 14 tube-in-tube heat exchangers are distributed along the length of the pipe. The heat exchanger has an inner diameter of 50.8 mm and an outside diameter of 81 mm (Figures 15 and 16). The inlet of the cooling fluid for the heat exchangers comes from a 1 000 L constant header tank located approximately 28 m from the ground. The outlet of the cooling fluid goes into a 1 000 L reservoir located on the ground level. The inlets and outlets of the tube-in-tube heat exchangers are set up so that the cooling water flows in the opposite direction to the working fluid inside the pipe. The reservoir stores the heated cooling fluid before it is pumped into a cooling tower, which cools the liquid back to room temperature before it is pumped back to the 1 000 L constant header tank on the roof of the building. The 1 000 L header tank has an overflow line that goes back into the reservoirs (sump) on the ground floor. The flow rate through the condensers (tube-in-tube) heat exchangers are controlled by the operator by means of ball valves, which are located on the ground level.

On the bottom horizontal pipe of the rectangular natural circulation loop, a non-bevelled orifice plate with a  $\beta = 0.33$  (diameter ratio) was installed, which can measure flow in both directions when the system is oscillating. The orifice plate was placed in the centre of the pipe to ensure that the downstream and upstream 90° angle bends do not influence the flow measurements though any swirls from the bends. On the top right corner of the natural circulation loop, a bleeder valve was installed to eliminate all the air inside the loop.

## 4.2 Recommissioning

The 27 m x 6 m thermosyphon loop had last worked in 2012. Since then, the loop had been non-operational for four years. Because the system is situated outside, the environment had started to affect the condition of the loop. The cooling system for cooling water of the condenser uses PVC pipes, which deteriorate due to the ultraviolet rays of the sun. The PVC pipes in the top section of the loop were affected most, and some of the sections needed to be replaced. The electric motors, which had been non-operational for a few years, had seized and needed to be partially disassembled and the shafts needed to be loosened to enable the motors to start again. The pressure and the differential pressure transducers were removed and new ones were ordered and installed. The four working fluid thermocouples needed to be replaced (see Section 4.3).

## 4.3 Sensors

The working fluid temperatures of the evaporator inlet and outlet and condenser inlet and outlet sections were measured using 1.6 mm T-type thermocouples, TE (top element), TC (top cooling), BC (bottom cooling) and BE (bottom element) (Figure 20). The condenser cooling water temperatures were measured at the inlet and outlet of each heat exchanger with 1.6 mm T-type thermocouple probes. The temperatures of the heating elements were measured using J-type thermocouple probes.

The thermocouples were calibrated using a substandard platinum resistance thermometer manufactured by Isotech with model number 935-14-72. The tests indicated all the thermocouples measured within an acceptable accuracy range with little deviation between thermocouples of the same set (see Appendix A.4).

The flow rate measurements across the orifice plate were done using an Endress-Hauser Deltabar S PMD75 differential pressure transducer (Serial: L600562109D) with a 4-20 mA output signal. This transducer is capable of reading in both directions.

The relationship between the pressure difference and the mass flow rate in the system was acquired by doing the calibration of the orifice plate, not separately, but as part of the system, with the associated idiosyncrasies of the system as part of the calibration. Several tests showed repeatable results, leading to a satisfactory calibration curve (see Appendix A.3).

The pressure of the system was measured with an Endress-Hauser Cerabar S PMC71 pressure transducer (Serial: L600862109D) with a 4-20 mA output signal. The pressure transducers were both calibrated using a WIKA Master pressure gauge (Calibration certificate number: 07-00000345 and 07-00000346) (see Appendix D).



## 4.4 Data acquisition

The thermocouples were connected to an Agilent 34970A data logger (Serial: MY44035920). The pressure transducer was measured using a National Instruments NI cDAQ-9184 data logger with an NI 9203 cartridge. Data integration took place over a period of 20 ms and was logged every second.

## 4.5 Operational procedures

The thermosyphon loop is initially filled with water while the valve to the expansion tank is open. The bleeder valve on the top horizontal pipe is, first, left open to let the unwanted air escape. Once it is filled with water to the top of the loop (indicated by water leaking from the bleeder valve), the v escape valve is closed and the expansion tank starts to fill. The expansion tank is filled until the pressure transducer indicates 2.8 bar. When the pressure transducer indicates 2.8 bar, the feeder line is closed and the bleeder valve is opened for a brief second again, to ensure that no unwanted air has been let in by the water feeding line.

The positive and negative tubes of the differential pressure transducer need to be bled to ensure that no air, which could affect the pressure readings, is trapped inside them. These tubes are transparent and trapped air can easily be spotted inside them. The wall pressure transducer also needs to be bled, to ensure an accurate pressure head reading.

The sump needs to be filled and the water needs to be pumped to the top header tank. There needs to be a sufficient amount of water in the sump while the overflow of the constant header tank is running (half full). Once both the tanks are full, the condensers need to be flushed to remove the air that is trapped inside them. This is done by turning the system on – all the pumps and the cooling tower – and draining each condenser individually by opening the ball valves fully until the flow from the condenser is steady, without any gushing and or gurgling.

While doing these procedures the system needs to be checked for any leaks from one of the condensers or the thermosyphon loop. The slightest leak in the system can disturb the measurements. The instruments should then be connected to a computer, which starts to record the pressure and temperature measurements. The heating element can be turned on by, first, turning on the master switch on the switchboard, then using the dial to set the ampere value (power) that each element bundle should give, and then turning on the elements.

Depending on when the condensers are turned on, all the pumps and the cooling tower need to be turned on before the chosen condenser is activated. A bucket is used to determine the flow rate through the active condenser, by noting the time it takes for the fluid to fill the bucket. The process of attaining the correct flow could be time-consuming. Turning on the condenser and readjusting the flow affects the working fluid's flow greatly, and should be avoided.

## 5 OBSERVATIONS AND RESULTS

In this section, two series of experimental data will be presented and discussed. The first experimental set, set 1, represents a series of experiments that was conducted with the top right-hand vertical condenser activated (see Figure 20). The second set of experimental data was acquired with the top right-hand horizontal condenser activated (see Figure 20). The calibrated theoretical simulations were compared with experimental results. As is common in two phase-flow analysis, correlating factors were adjusted (calibrated) for a benchmark test run. The factors that were determined for a benchmark experimental test run are coefficient of friction, the void fraction, and the convection heat transfer coefficient.

### 5.1 Experimental sets 1 and 2

A series of experiments was conducted for which the top right-hand side condenser cooling water was activated from the start of the experiment (see Figure 20). All the heating elements were also turned on at 0 s. The heating elements were set to full power from the start of the experiment, and the cooling fluid through the condenser needed to be at a very low flow rate, of about 0.0682 L/s. This was done to ensure that the working fluid would enter the separated two-phase flow regime. The experiments were all started at about 08:00 to ensure that the initial temperatures of the system were roughly the same (8 to 12° C). Doing so also ensured that all the components of the structure of the loop were more or less at the same initial temperatures. The position for the condenser was chosen because most of the experiments reported in the literature were done with the heat input on the left-hand side vertical pipe and the heat removal on the right-hand side vertical pipe of the system. The heating elements were turned off after the system reached two-phase flow. This was done to check if the theoretical simulation program can predict the mass flow rate of the working fluid when the system is losing heat. The experiments were repeated and showed similar results; thus, only one experiment will be reported to represent each set.

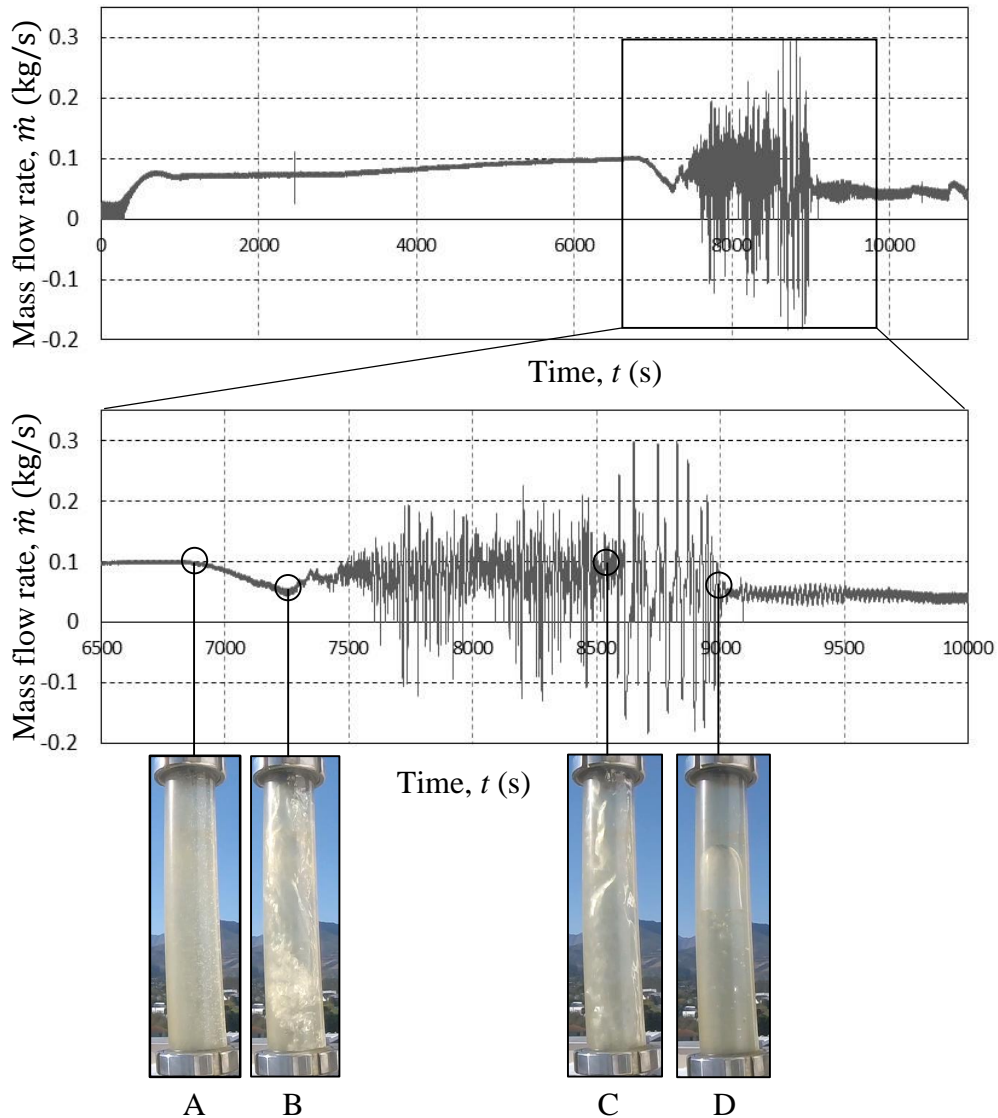


Figure 21 Experimental mass flow rate measurements over time and flow regimes as observed through vertical sight glass for set 1

In Figure 21 the mass flow rate of the working fluid is shown over time. Below the graph, a series of photos is presented, which shows the flow regime that was observed through the vertical sight glass above the heating section (see Figure 21). At 700 s the working fluid reached a peak; this happened because of the initial high-density gradient in the system. The working fluid's mass flow rate increased, increasing the rate at which the heat was transported to the rest of the system. When the temperature difference between the left- and the right-hand sides of the loop is smaller, the density gradient decreases, which, in turn, results in a reduced mass flow rate. The working fluid was in the single-phase region for the first 6 800 s, when it reached a maximum single-phase mass flow rate of

0.1 kg/s. This maximum single-phase mass flow rate was seen in all the experiments with the condenser thus activated.

The working fluid started to move into the two-phase flow region at point A, and it can be seen, through the sight glass, that the flow started turning into bubbly flow, with small bubbles appearing in the working fluid. In the next 400 s the flow went from bubbly flow to wispy-annular flow, see point B in Figure 21. As the working fluid transitioned from bubble flow to wispy-annular flow, so the heat transfer went from nucleate boiling to film evaporator effect. Before the power was turned off at point C, the flow represented a combination of wispy-annular flow and fully developed annular flow (see point C in Figure 21). At point C, film-evaporation was the major heat transfer mechanism in the heating section (see Section 3.5.2). Once the power was turned off, at point C, the working fluid returned to slug flow (see point D in Figure 21), and then back to single-phase flow shortly thereafter, without bubbles in the working fluid. The mass flow rate remained constant in the system, because of the residual heat from the structure. The heat gained from the structure of the system caused a density gradient. The density gradient can be seen in Figure 22(a), which shows the working fluid temperatures at the bottom of the loop, where temperatures at BE and BC were still much lower than the top temperatures at TE and TC.

The working fluid temperature, TE, was at the saturation temperature between 7 300 s and 9 000 s. This is indicated by the fluid not exceeding 110°C (Figure 22(a)), which is the saturation temperature corresponding to the pressure. The saturation temperature changed slightly, because of the change in pressure of this system, which caused the corresponding saturation temperature to change (see Figure 22(b)). It is clear in Figure 22(b) that the pressure of the system only changed slightly, and returned back to the average pressure head after the system had stopped boiling.

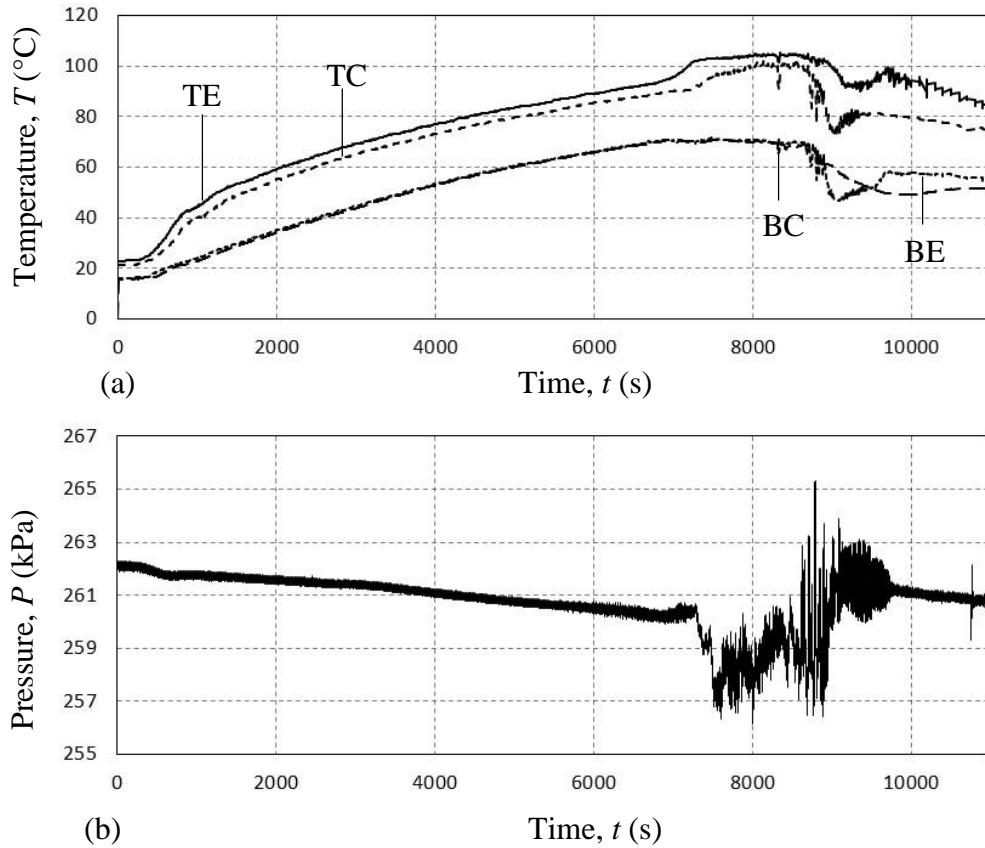


Figure 22 Working fluid temperatures over time (a), and pressure over time (b), for set 1

The second set of experiments was conducted with the top right horizontal condenser activated (see Figure 20). The position of the condenser is proposed by Dobson and Ruppertsberg (2007). For these experiments, the cooling water and the heating elements were turned on from the start of the experiment. The cooling water flow rate was set to between 0.0416 and 0.0625 L/s. The same power input was used for this experimental set as for experimental set 1, to ensure that the working fluid started boiling. The experiments were all conducted early in the morning to ensure that the initial temperature of the system was relatively constant (8 to 12  $^{\circ}\text{C}$ ). Doing so also ensured that the initial temperature of the working fluid and the structure was relatively similar.

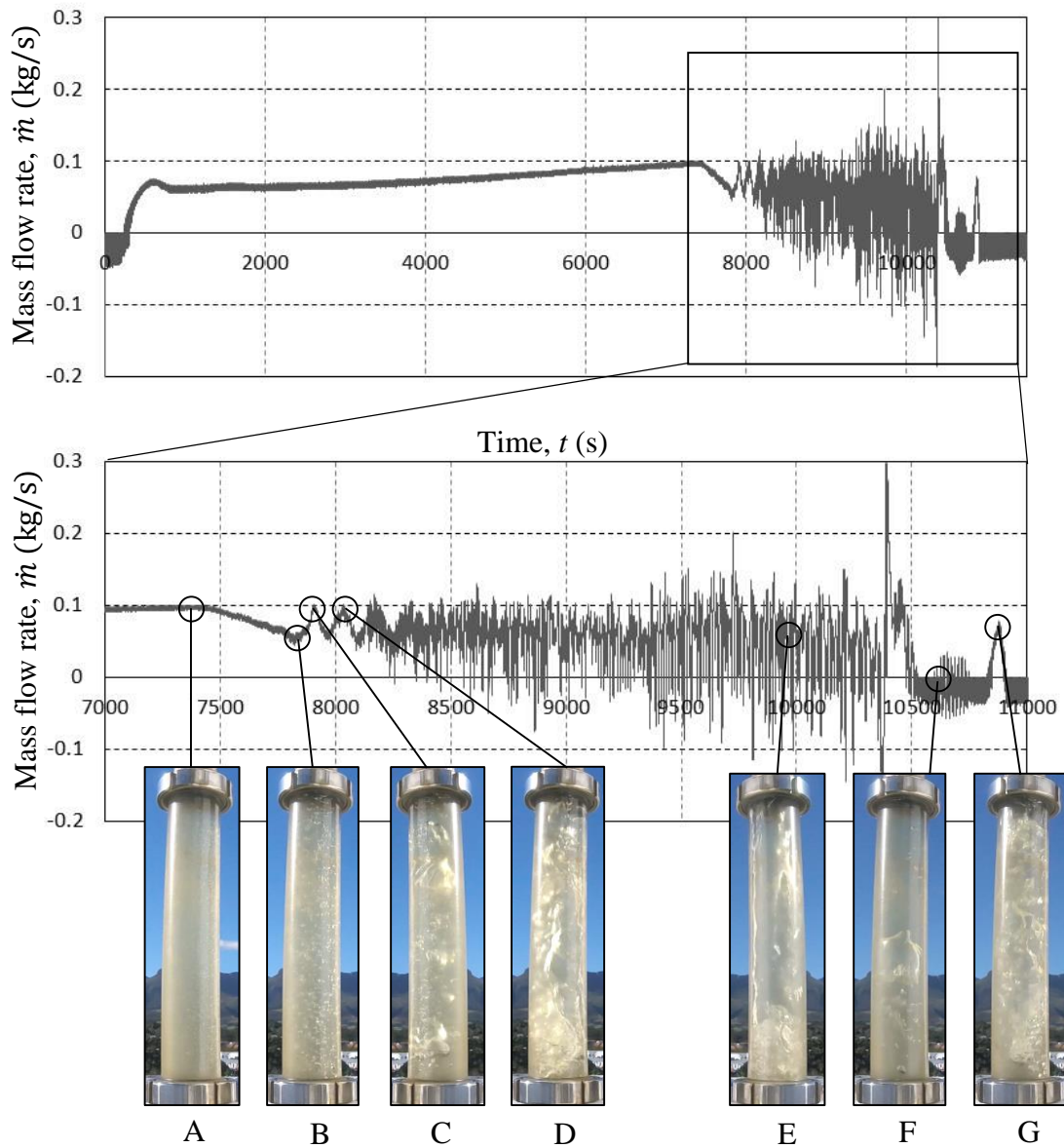


Figure 23 Experimental mass flow rate measurements over time and flow regimes as observed through vertical sight glass for set 2

The working fluid was in the single flow region for the first 7 400 s of the experiment (see Figure 23). The maximum single-phase mass flow rate is similar to that of the first experimental set, at 0.1 kg/s. The working fluid enters the two-phase flow region at 7 400 s, at point A. At this point, small bubbles start to form inside the working fluid. The heat transfer in the evaporator section of the loop at this stage of the experiment is due to nucleate boiling. In Figure 23, at point A, bubble flow can be seen, which is the first two-phase flow regime (see Figure

24(a)). The bubble flow developed for the next 400 s; the bubble size increased; larger and more noticeable bubbles occurred at point B. The flow then turned into slug flow at point C, and to churn flow at point D. Then, the flow was a combination of wispy-annular and annular flow, until it became fully annular flow at point E. The power was turned off at point E, when the flow was fully annular. After the heating elements had been switched off, the mass flow rate dropped to zero after 500 s. When the flow rate was zero, at point F, the working fluid was in thermodynamic equilibrium, and the density gradient was zero. The residual heat from the structure of the loop continued heating the working fluid, until a large enough density gradient was present to overcome the static friction of the system and to allow the working fluid to start circulating again, at point G in Figure 23. When the working fluid started circulating again, the heat was transferred by convection around the loop, decreasing the density gradient, and returning the mass flow rate of the working fluid back to zero.

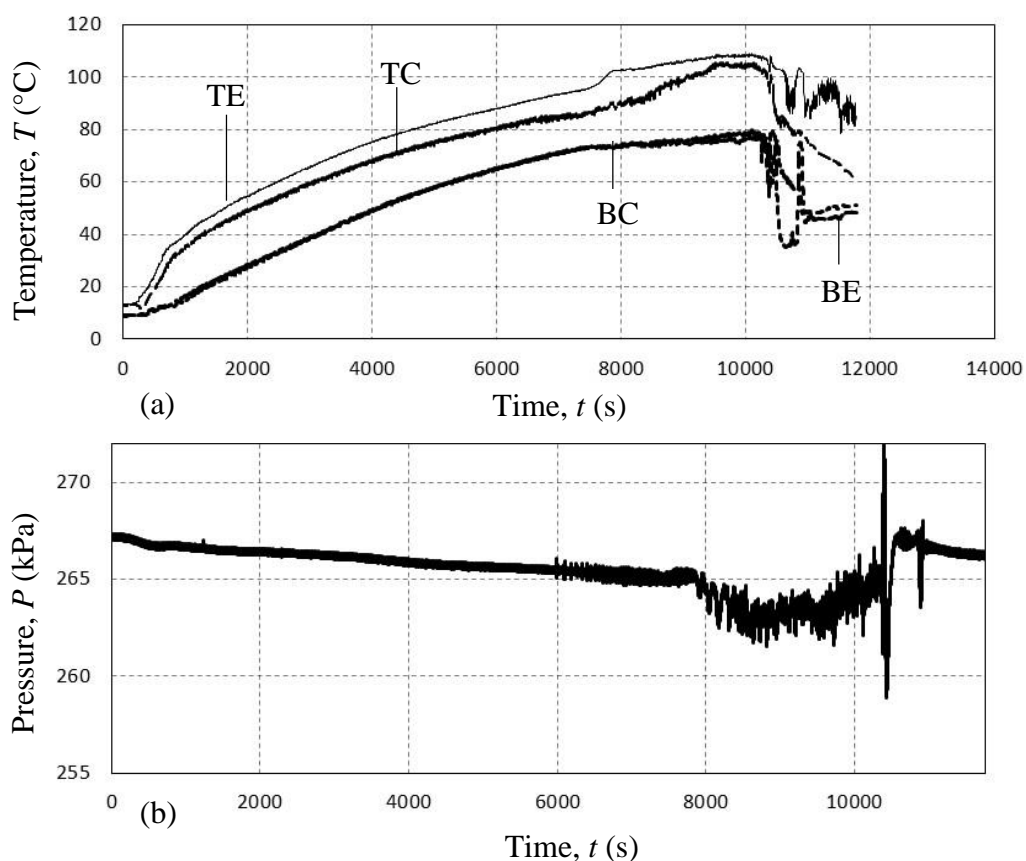


Figure 24 (a) Working fluid temperatures over time, (b) Pressure over time, for set 2

The working fluid temperature at TE was at the saturation temperature between 8 000 s and 10 000 s. The instantaneous change in pressure in the top horizontal

pipe caused the corresponding saturation temperature to fluctuate (see Figure 24(a)).

The fluctuations in the pressure of the experimental sets were caused by *geysering* (see Section 2.3). This occurs when pressure fluctuations in the system cause sudden increases in vapour generation at the bottom of the vertical heating section (see Figure 22(b) and Figure 24(b)). This sudden increase in vapour is the cause of vapour bursting explosively in the top part of the heating section. As subcooled liquid returns, the section is returned to a non-boiling state, and the cycle is repeated. The return of the liquid after the vapour explosion is perceived as annular-flow through the sight glass, see point C. Geysering has a great effect on the differential pressure and pressure of the system. Geysering causes an acceleration and deceleration of the mass flow rate and has an oscillating effect on the working fluid, which causes reversed flow (see Figures 21 and 23). These fluctuations can also be caused by chugging, which is similar to geysering, and which can have either minor or major effects on the flow of the working fluid.

## 5.2 Theoretical modelling

The physical experimental model was positioned outside, against a vertical wall between two buildings. The placement of the thermosyphon meant that the sun did not fall on the thermosyphon loop evenly. The thermosyphon's position between buildings also caused fluctuating wind speeds on the system, making it difficult to determine the natural convection on the outside layer of the system. The heating elements coil-to-air ratio was not recorded when the loop was installed either. These unknown factors in this non-ideal environment needed to be calibrated to achieve accuracy with the theoretical program.

J.C. Ruppertsberg had conducted experiments with fully calibrated data when the thermosyphons loop's thermocouples on the heating elements and condensers were still functional. One of these data sets was used as a benchmark to calibrate the theoretical program before it was used to simulate the data acquired in Section 5.1 (see Figure 25).



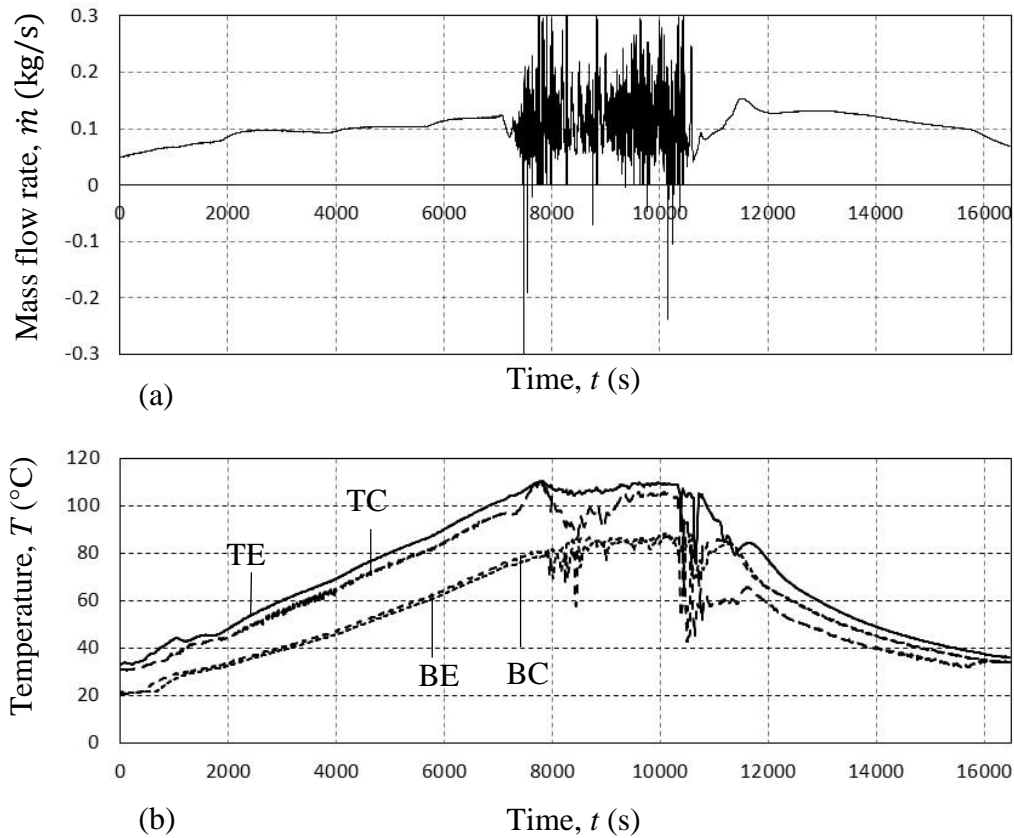


Figure 25 (a) Benchmark experimental mass flow rate over time (b) working fluid experimental temperatures over time

Figure 26 shows that the power input to the system was done in increments. The power was initially increased to 9 960 W from the start, 14 928 W at 1 795 s, 17 427 W at 3 595 s and 18 300 W at 5 340 s. The power was switched off at 10 140 s. The heat loss (dotted line) was calculated using  $Q_{loss} = \dot{m} c_p (TE - BE)$ , where  $\dot{m}$  is the mass flow rate of the system, and  $c_p$  is the specific heat of water and  $TE - BE$  is the temperature difference between the water into the evaporator section (left-hand side of the loop) and the temperature of the water leaving the evaporator. The difference between the two lines are the losses to the environment and structure of the loop.

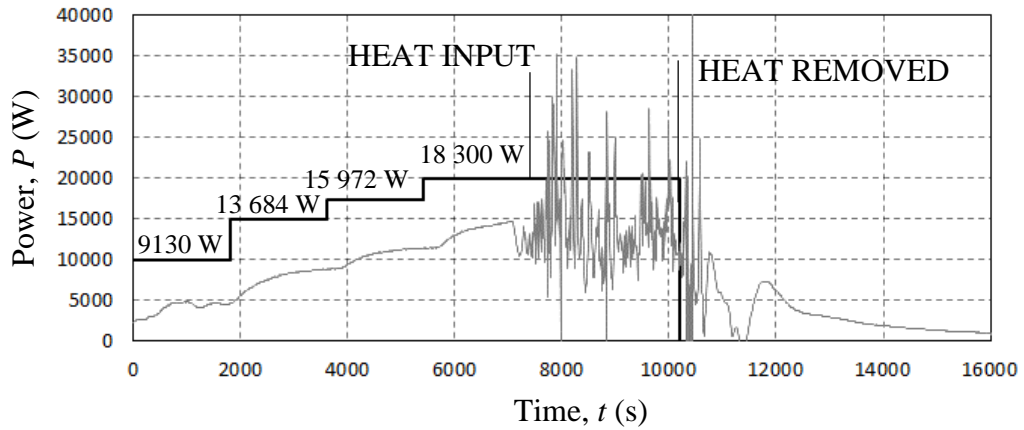


Figure 26 Benchmark heat input and heat removed from thermosyphon loop over time

### 5.2.1 Void fraction and frictional multiplier comparison

In this section, the separated flow models and frictional multiplier coefficients will be investigated, to determine which model predicts the mass flow rate of the working fluid the most accurately for the benchmark experiment discussed in Section 5.2. The models were used with correlation factors, to determine the mass flow rate of the working fluid. Table 4 shows the different combinations of separated flow models and the frictional multipliers used.

Table 4 Different void fraction and frictional multiplier cases used to determine the most appropriate theoretical prediction method for the performance of two-phase flow systems

Case	$\alpha$	$\phi^2$
1	CISE correlation (Whalley, 1897)	Lockhart-Martinelli
2	CISE correlation	Friedel
3	Lockhart-Martinelli (Lockhart & Martinelli, 1949)	Lockhart-Martinelli (Lockhart & Martinelli, 1949)
4	Lockhart-Martinelli	Friedel (Whalley, 1897)
5	Homogeneous (Carey, 1992)	Homogeneous (Carey, 1992)
6	Homogeneous	Friedel
7	Homogeneous	Lockhart-Martinelli

The single-phase region was not presented, because the void fraction is not applicable to the single-phase region of the flow; only when the fluid enters into separated flow does the void fraction have an effect on the mass flow rate. The friction factor was increased, because the theoretical mass flow rate was double the experimental mass flow rate. This indicates that the friction coefficient is not large enough or that there are minor losses inside the system that were not accounted for.

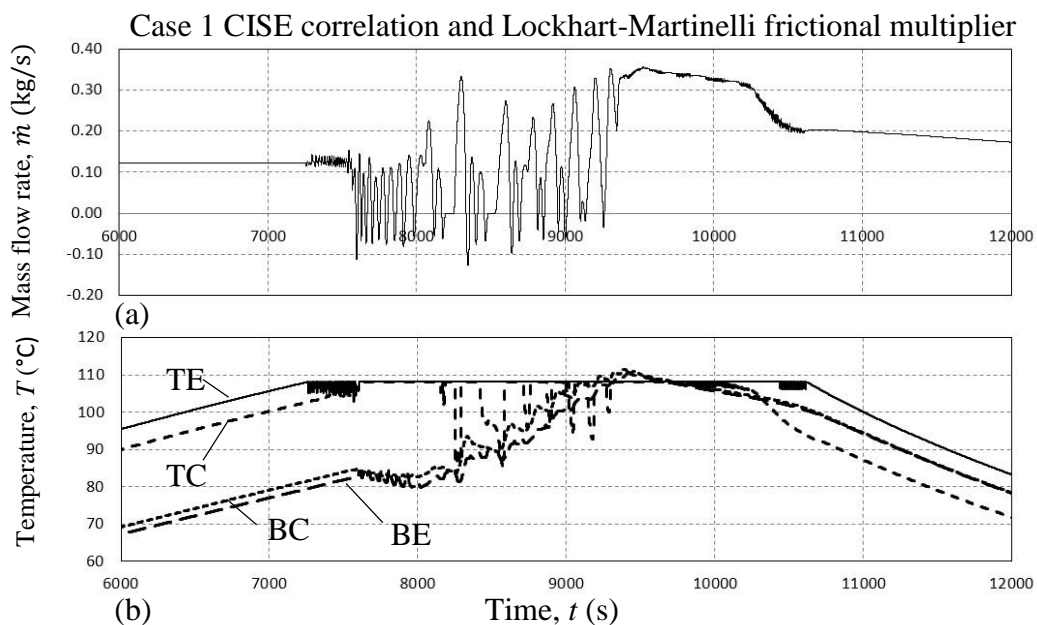


Figure 27 CISE correlation with the Lockhart-Martinelli frictional multiplier. Predicted theoretical results of working fluid (a) mass flow rate (b) temperatures

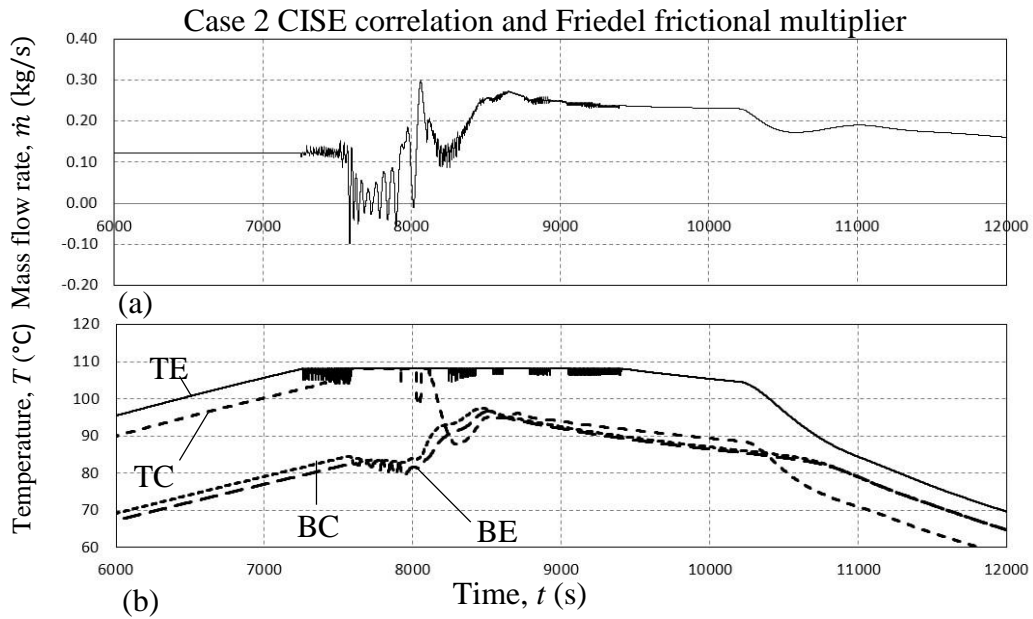


Figure 28 CISE correlation with the Friedel frictional multiplier. Predicted theoretical results of working fluid (a) mass flow rate (b) temperatures

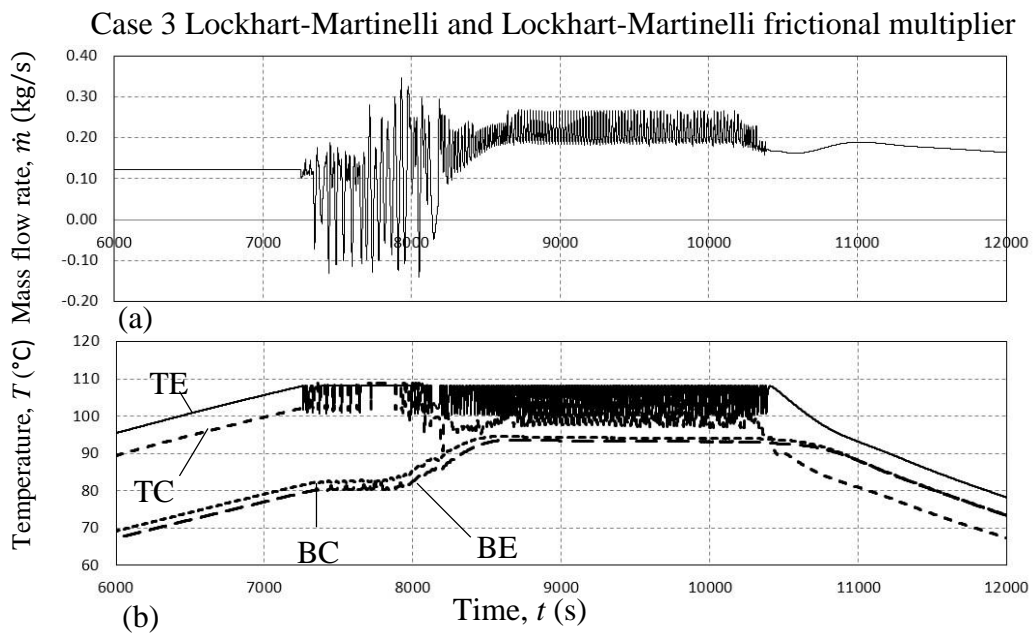


Figure 29 Lockhart-Martinelli model with Lockhart-Martinelli frictional multiplier. Predicted theoretical results of working fluid (a) mass flow rate (b) temperatures

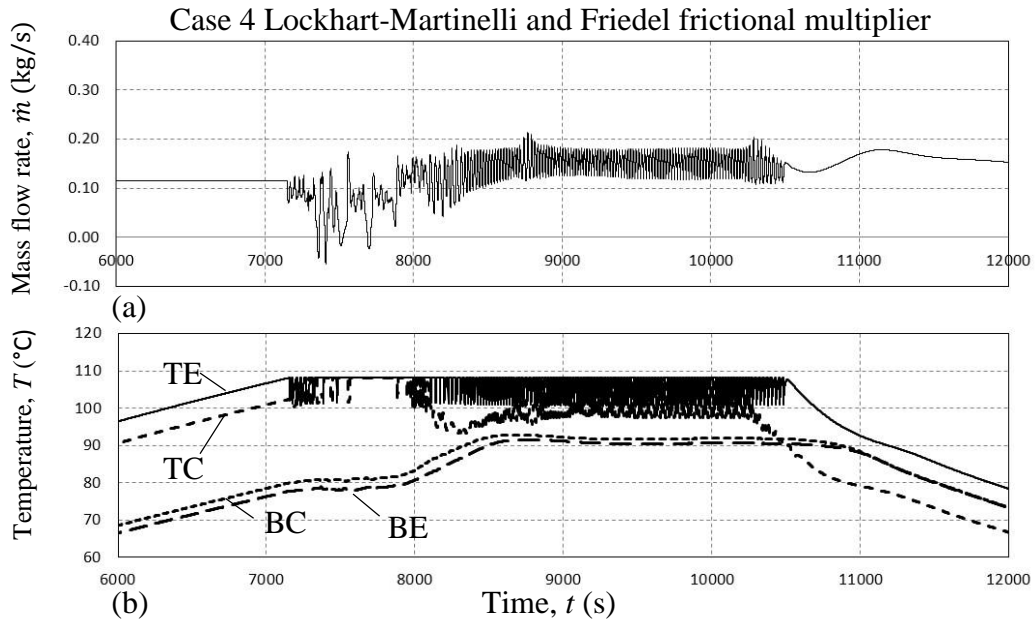


Figure 30 Lockhart-Martinelli model with Friedel frictional multiplier. Predicted theoretical results of working fluid (a) mass flow rate (b) temperatures

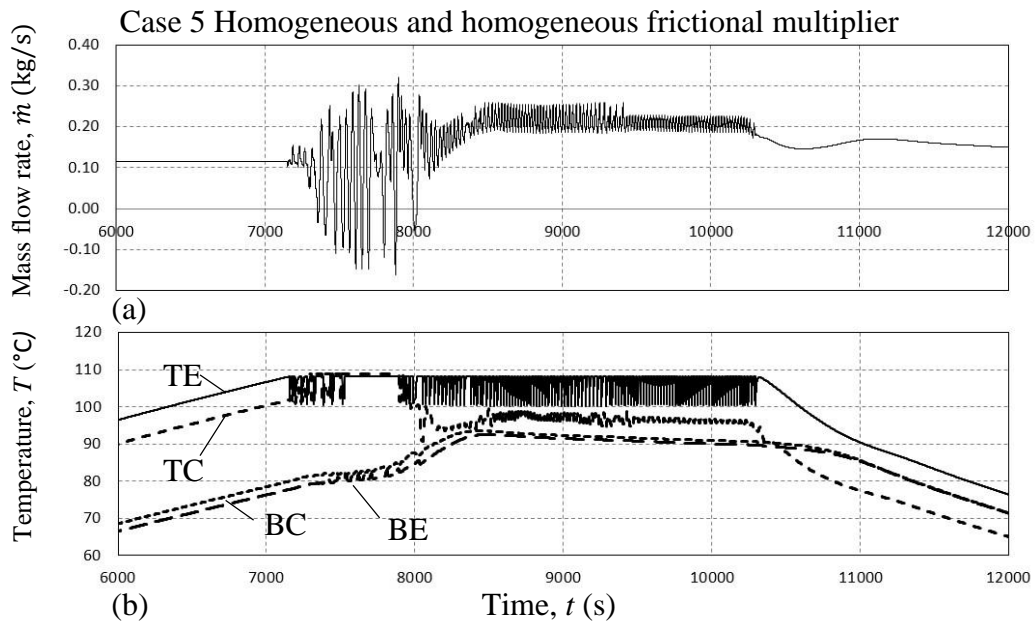


Figure 31 Homogeneous model with homogeneous frictional multiplier. Predicted theoretical results of working fluid (a) mass flow rate (b) temperatures

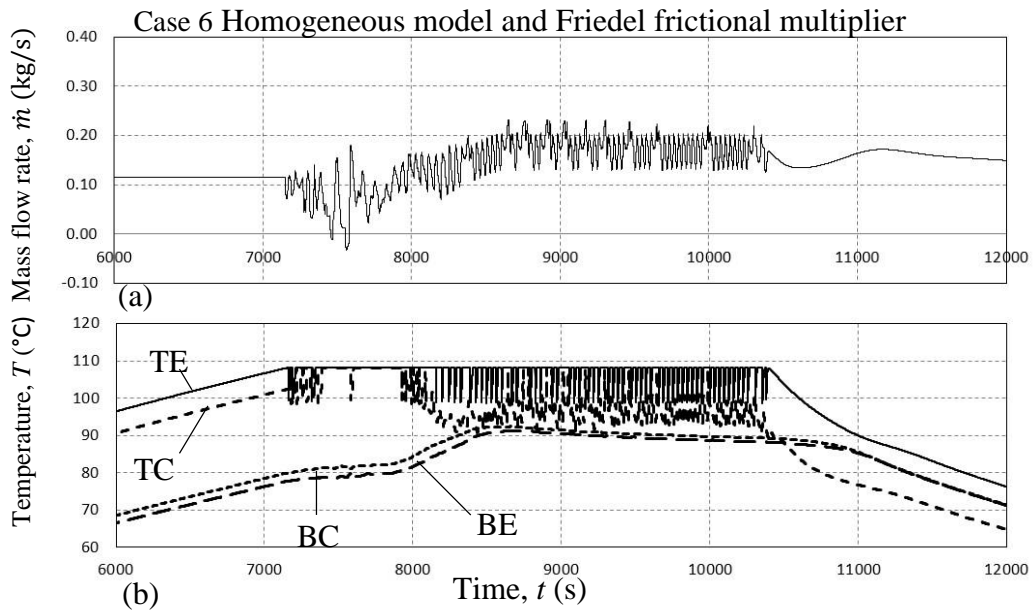


Figure 32 Homogeneous model and Friedel frictional multiplier. Predicted theoretical results of working fluid (a) mass flow rate (b) temperatures

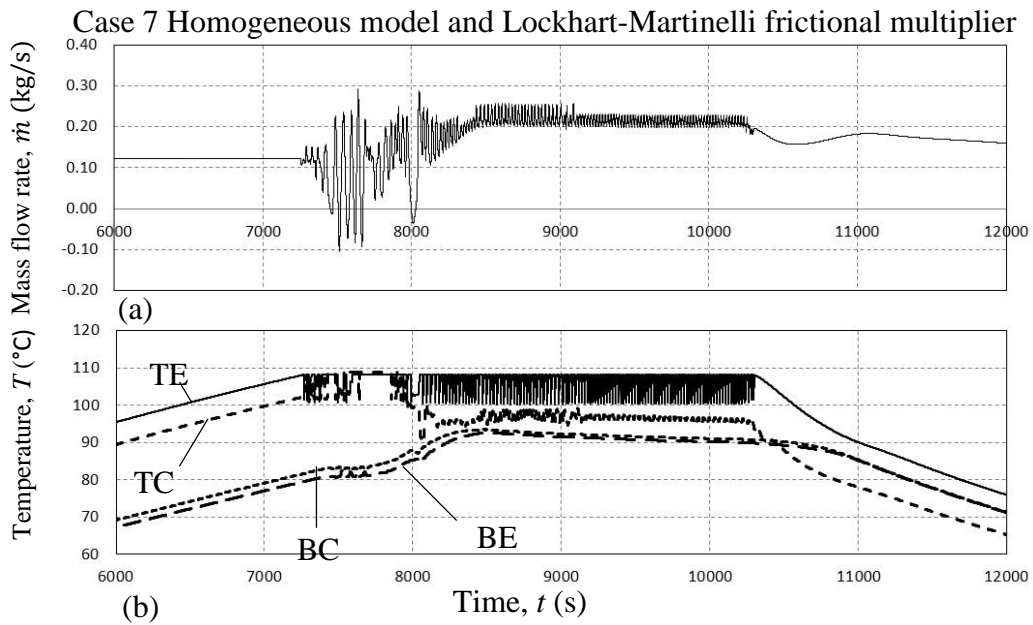


Figure 33 Homogeneous model and Lockhart-Martinelli frictional multiplier. Predicted theoretical results of working fluid (a) mass flow rate (b) temperatures

The void fraction and frictional multiplier coefficients gave very similar results in predicting the separated flow region of the benchmark experiment. Cases 1 and 2 (Figures 27 and 28), where the CISE correlation was used, was the most inaccurate method. The CISE correlation does not predict the flow fluctuations as accurately as the other cases do. The CISE correlation's void fraction could not go higher than 0.5 before the program became unstable, and the void fraction was restricted for this reason.

Most of the literature reports that the homogeneous void fraction model and frictional multiplier method is inaccurate. This was not the case for this system. The homogeneous void fraction model, Cases 5, 6 and 7 (Figures 31, 32 and 33), gave results very similar to the Lockhart-Martinelli void fraction model, which is proclaimed by the literature to be one of the most accurate methods. Two criteria need to be met to ensure that the most appropriate method is chosen to predict the separated flow region. The average mass flow rate needs to stay constant after the cooling water has been activated, and the mass flow rate fluctuations must not be reduced by the coefficient.

The Lockhart-Martinelli frictional multiplier did not affect the flow fluctuations, but the average mass flow rate did not stay constant when the cooling water was increased (see Cases 3 and 7, Figures 29 and 33). The Friedel frictional multiplier gave the lowest average mass flow rate, but when it was combined with the Homogeneous void fraction, it decreased the fluctuations of the flow (see Case 6, Figure 32). The Lockhart-Martinelli void fraction model gave the highest flow fluctuations, and pairing it with the Friedel frictional multiplier, which gave the lowest average mass flow rate, seems to be the best choice for predicting the separated flow region of the working fluid (see Case 4, Figure 30).

The temperature graphs were very similar, and all gave accurate predictions of the working fluid temperature. The only inaccurate temperature predictions were in Cases 1 and 2 (Figures 27 and 28).

### 5.2.2 Comparison of theoretical and experimental models

The Lockhart-Martinelli void fraction model and the Friedel frictional multiplier (Case 4 in Figure 30, Section 5.2.1) method was chosen as the most accurate method for predicting the separated flow region of the working fluid. Figure 34 presents the benchmark experiment and the calibrated theoretical simulation program's mass flow rate.

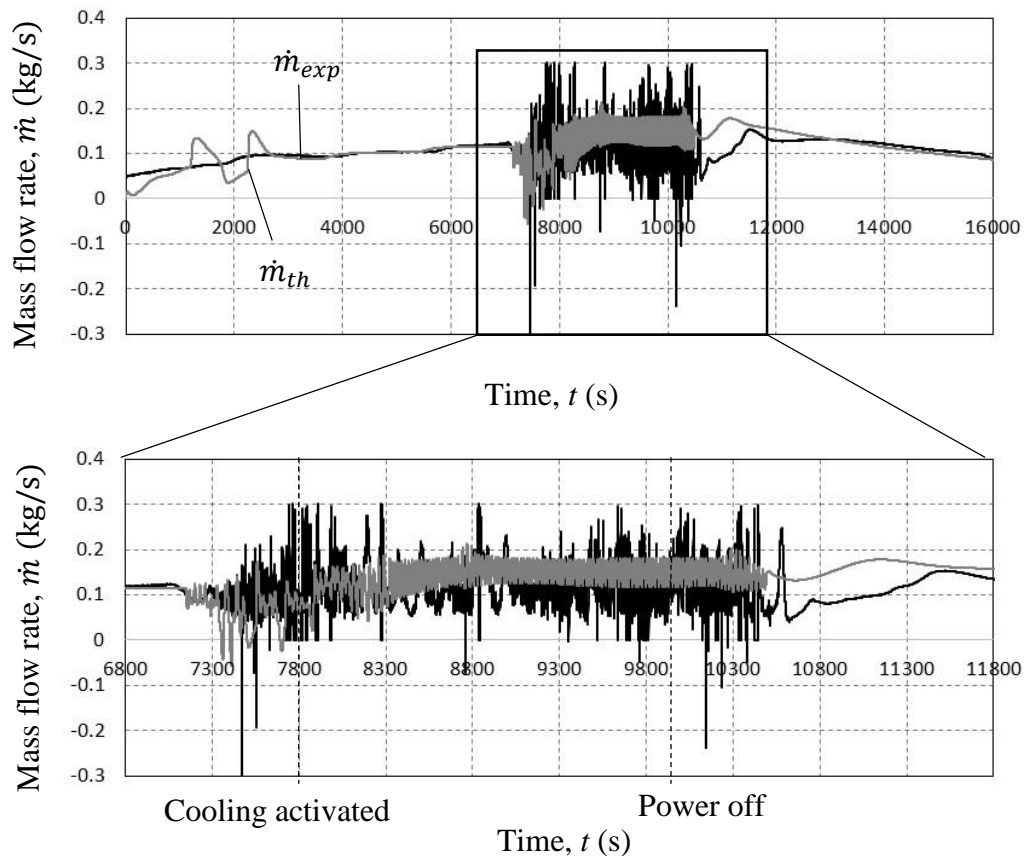


Figure 34 Comparison of experimental and theoretical mass flow rate over time

The theoretical model predicted the mass flow rate of the system well, with a slight overshoot at 1 800 s, where the simulation model readjusted itself to follow the experimental mass flow rate more accurately from this point onwards. The experimental and the theoretical mass flow rates decreased at 7 200 s. At this time, the working fluid entered the separated flow region, and the friction increased. The increase in friction was simulated by the mathematical simulation model by the frictional multiplier,  $\phi^2$ , which was then activated. At the same point, the void fraction started increasing and the two-phase heat transfer coefficients were used. When the cooling was activated at 7 800 s, the theoretical mass flow rate increased, because of an increase in density gradient. The experimental mass flow rate, however, did not increase, and only changed its oscillating pattern. The reason for the increase of the theoretical mass flow rate was the large amount of heat gained by the structure of the loop before the cooling water was activated. This indicates that the structural properties of the theoretical model are not correct. The friction coefficients also had an effect on the mass flow rate, and also resulted from the increase in mass flow rate at that point. When the system entered the single-phase region again, the experimental mass flow rate was



much lower than that of the theoretical model. The theoretical model also returned to the single-phase region at 10 200 s, while the experimental mass flow rate returned to the single-phase region at 10 500 s. This is an indication that the heat transfer coefficients and structural properties were not accurate.

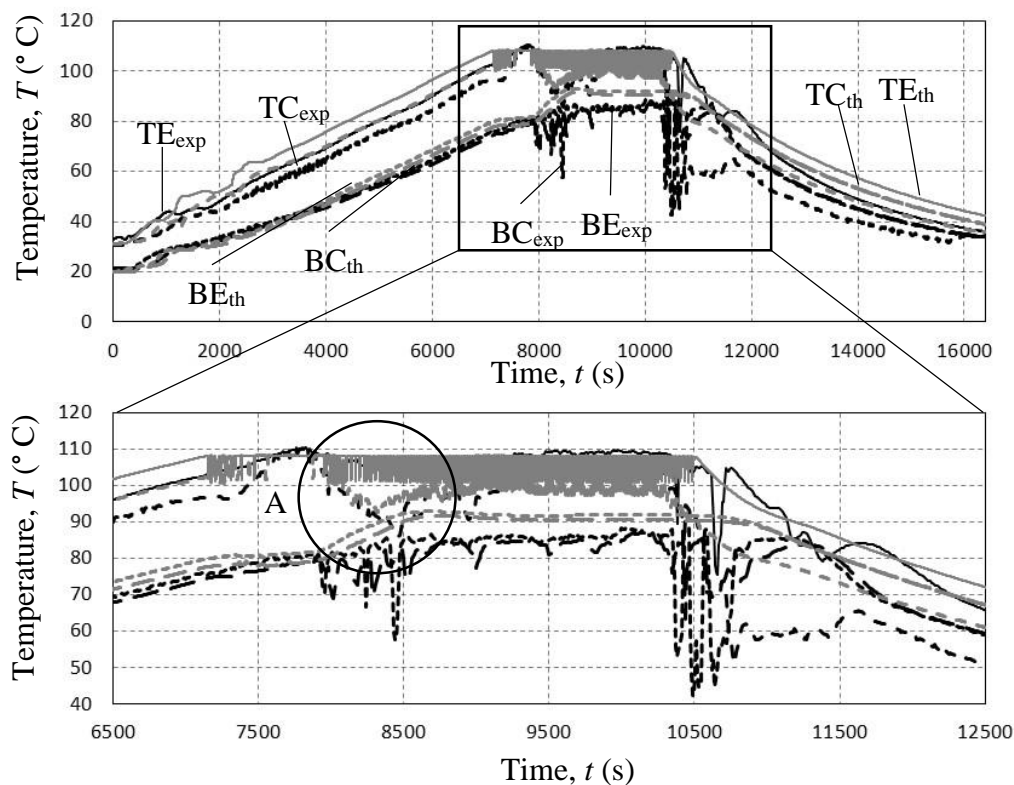


Figure 35 Comparison of benchmark experiment and theoretical working fluid temperatures over time

The theoretical program simulated the working fluid temperatures well in the single-phase region from 0 to 7 000 s (see Figure 35). In this region, the experimental and theoretical temperatures had the same gradient. The top heating section temperatures, TE, reached approximately the same maximum temperatures, because of the saturation temperature being dependent on the constant pressure. The theoretical program, however, did not compensate for the instantaneous pressure fluctuations and, thus, the saturation temperature remained constant. The simulation program simulated the temperature of the top cooling section (TC) very accurately at point A (Figure 35). At this point, the condenser cooling water was activated and the TE thermocouple was downstream of the condenser, resulting in a temperature drop. As the working fluid returned to the single-phase region, the theoretical temperature was higher than that of the

experimental temperatures. This is an indication of the structural properties and the heat transfer coefficients, which were not precise.

The simulation program was then used to simulate the mass flow rate and working fluid temperature of the experimental set 2 (see Section 5.1). The difference between the experimental conditions of the benchmark experiment and the experimental set 2 is that experimental set 2 condenser cooling water was activated from the start of the experiment. The same top right corner horizontal condenser was used. The heating elements were set to maximum power from the start of the experiment, to ensure that the working fluid would enter the separated flow region.

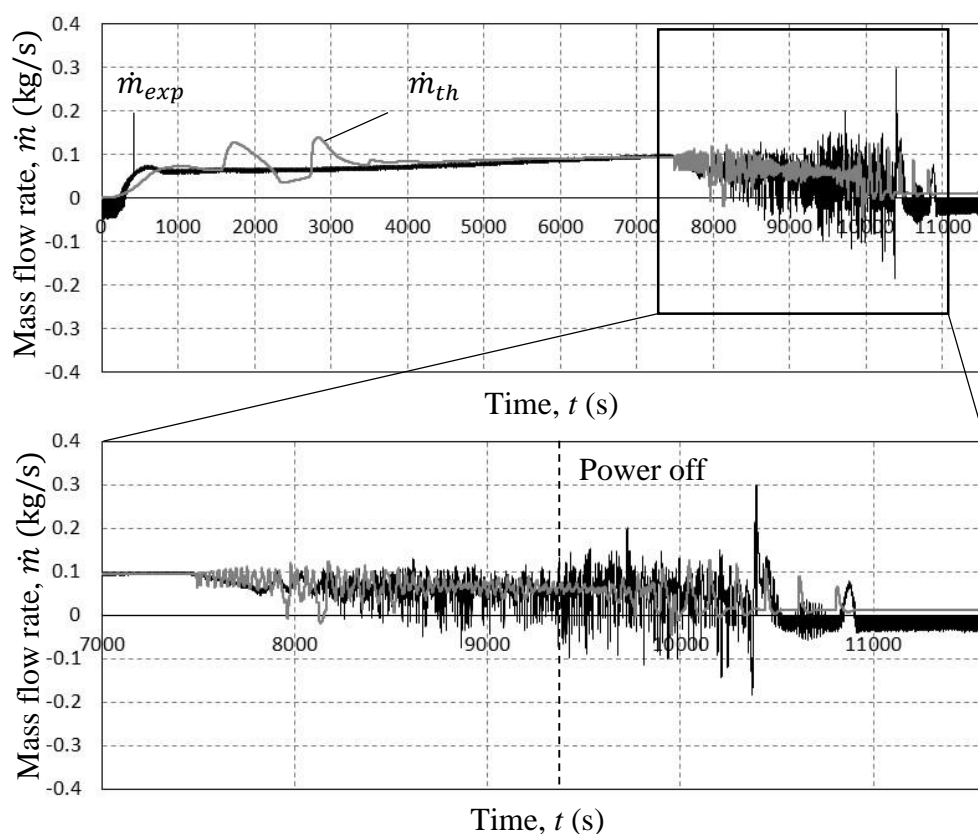


Figure 36 Comparison of experimental set 2 and theoretical mass flow rate over time

The theoretical program simulated the single-phase region very accurately. The theoretical program had the same overshoot at 1 800 s as recorded in Figure 36 but corrected itself to follow the experimental mass flow rate perfectly from then on. The theoretical mass flow rate entered the separated flow region at the same time as the experimental program, at 7 500 s. This indicates that the single-phase heat transfer coefficient was accurate, and that the constant pressure head of the

simulation model was the same as the experimental pressure. The theoretical mass flow rate followed the experimental mass flow rate almost perfectly from the time the power was turned off at 9 400 s, until 10 500 s. The theoretical mass flow rate had two last increases in mass flow rate before it returned to almost zero. The experimental mass flow rate only increased one last time before returning to zero. This is an indication that the structural properties of the loop are not precise, and neither are the friction coefficients. The theoretical mass flow rate did not return to zero fully, because of the residual heat of the structure was still causing a density gradient.

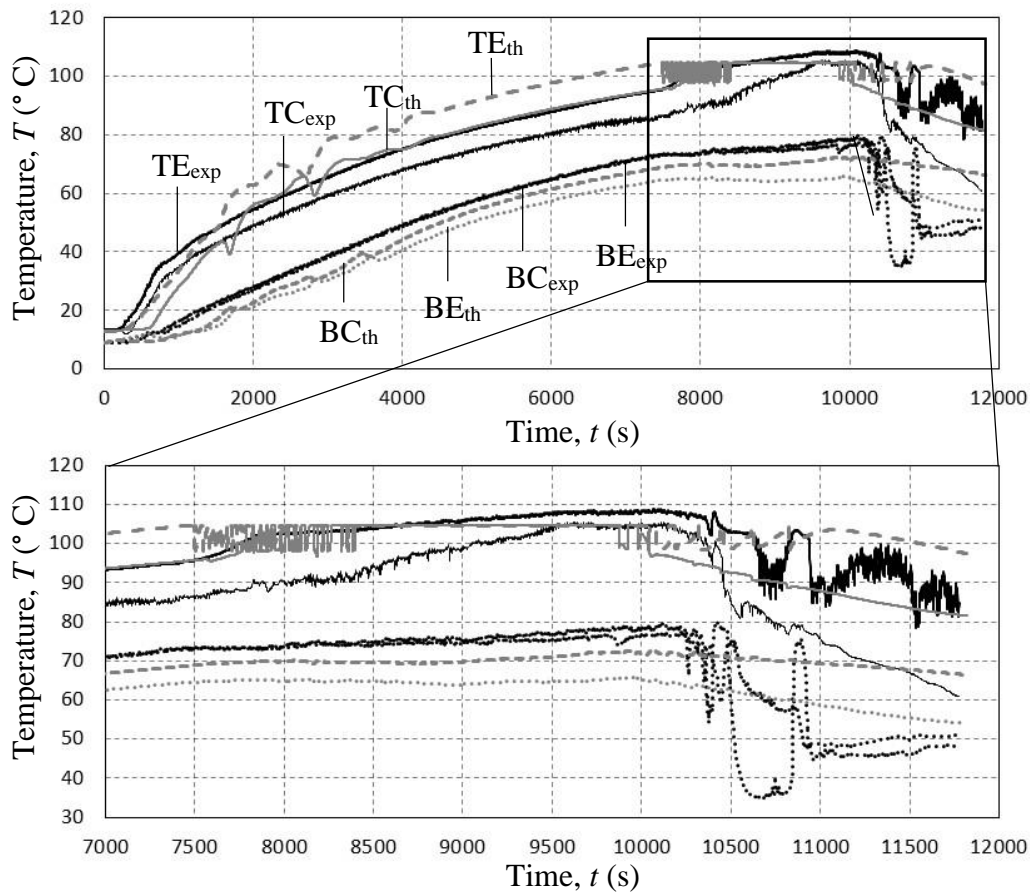


Figure 37 Comparison of experimental set 2 and theoretical working fluid temperatures over time

The experimental working fluid temperature had a smaller temperature difference than the theoretical working fluid temperature. In Figure 37, the theoretical working fluid temperatures BE and BC are lower than that of the experimental working fluid temperatures. The working fluid temperatures TC and TE are higher than that of the experimental working fluid temperatures. This indicates that the heat loss simulated by the program was higher than that of the experimental heat

loss. This is because the thermosyphon loop was situated outside, against the side of a building, where the surrounding conditions change daily. The difference in temperature can also be the result of initial conditions of the structure, which could be lower or higher than that of the experiment. The theoretical temperatures had the same gradient as the experimental temperatures in the single-phase region from 0 s to 7000 s. This indicates that the heat transfer coefficient in the single-phase region was accurate.

The two experiments that were simulated differed from one another in one main way: the benchmark experiment had, had sufficient time for the physical structure of the loop to increase in temperature before the cooling water was activated. In the second experiment, the physical structure did not have the same heat increase, because the cooling water had been activated at the start of the experiment. The simulated mass flow rate of the second set of experiments were more accurate than that of the bench experiment. This indicates that the heat capacity, residual heat and physical properties of the physical structure have a very large effect on the mass flow rate of the simulation model. The theoretical simulation model predicted the benchmark temperatures more accurately than the second experiment did. This is because the program was calibrated to the conditions of the surroundings on that day, which was not the same as the second experiment's conditions in the surroundings on the day it was conducted. It can also be seen that the heat transfer coefficients have a large effect on the mass flow rate and that the single-phase heat transfer coefficients play a bigger role than the two-phase coefficients do.

### 5.2.3 Experimental and theoretical comparison of system pressure

In this section the boussinesq approximation was not used and the actual pressure variation around the loop was calculated. This relatively small pressure drop is due to the friction as the fluid flows around the loop.

Boussinesq assumes a hydrostatic fluid and as such does not take into account the pressure drop due to friction. In figure 38 a) the initial theoretical working fluid pressure, at 0 s, is higher than that of the experimental measured pressure. The theoretical density used to calculate the hydrostatic pressure of the system could be larger than that of the experimental density. The theoretical pressure decreases to 260 kPa gauge pressure where the theoretical pressure's lowest value is 264 kPa. The theoretical pressure drop has a larger gradient than that of the experimental pressure drop. This can be because the coefficient of friction which is not accurate enough for this system. When introducing the change in pressure into the simulation program the void fraction needs to be limited to a smaller value because the program becomes numerically unstable and causes oscillations in the system.

The change in void fraction size is seen in figure 36, where the theoretical mass flow rate fluctuates at a higher amplitude than the mass flow rate in figure 38 a) .

Because the change in pressure causes the program to become unstable at a lower void fraction, the program was chosen to operate without the pressure drop and the boussinesq approximation was assumed.

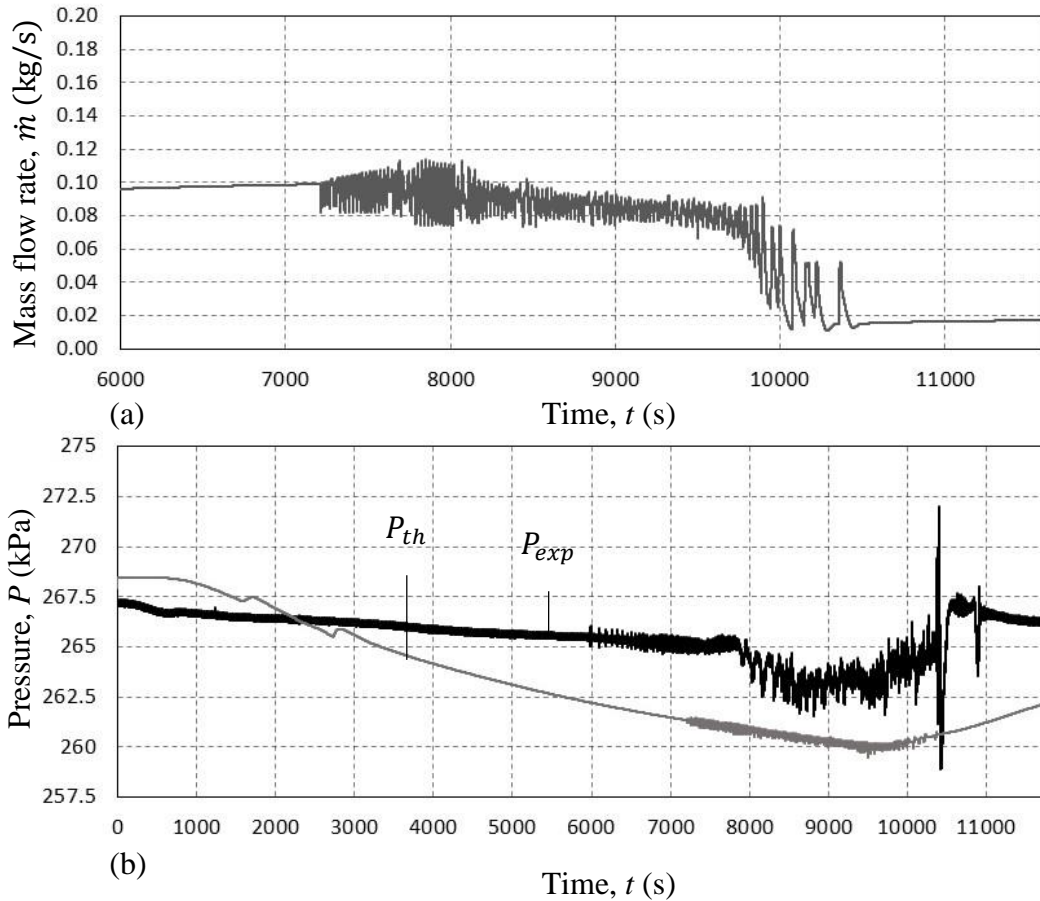


Figure 38 a) Theoretical mass flow rate of experimental set 2 over time, b) Experimental and theoretical pressure of experimental set 2 over time

#### 5.2.4 Theoretical and experimental comparison of single phase region

In this section the theoretical simulation program was used to simulate a experiment which was only operated in the single phase region. The theoretical and experimental mass flow rate and temperature are compared.

The experiment was conducted with the top right horizontal condenser activated from the start of the experiment with the heating elements set to maximum power (18.2 kW). The condenser was set to 0.06 L/s, just above 0.05 L/s to ensure that

the working fluid stays in the single phase region. The power was switched off at 14400 s

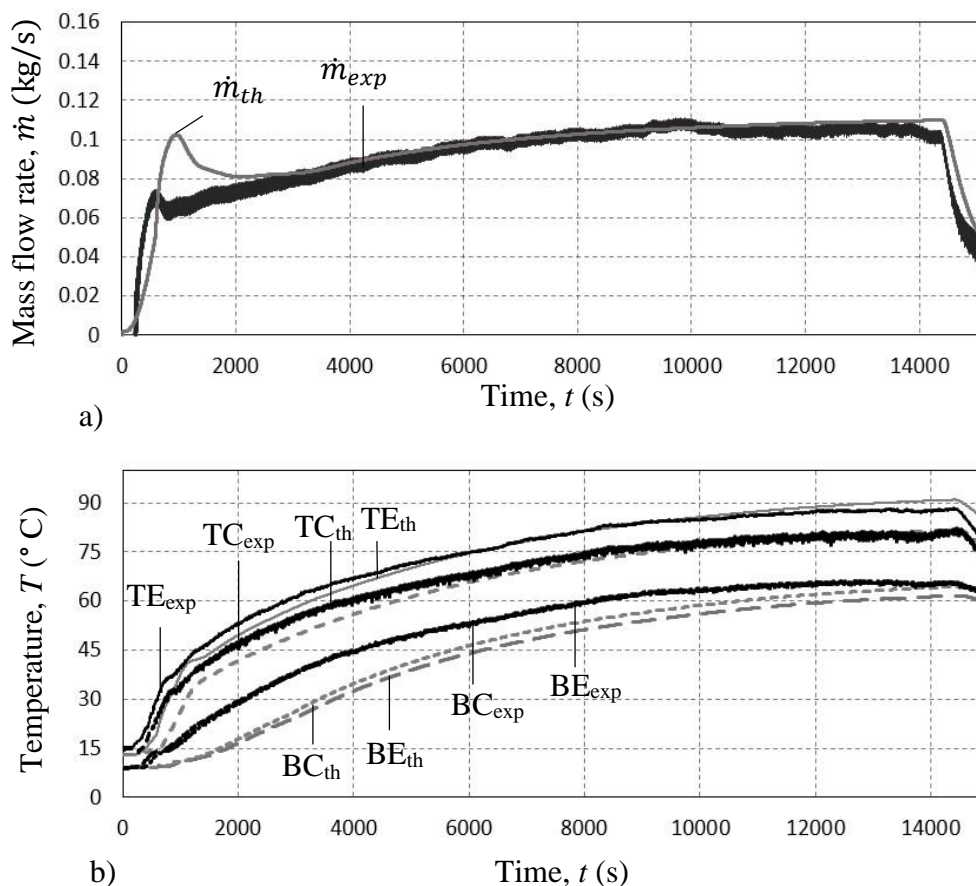


Figure 39 a) Theoretical and experimental mass flow rate over time, b) theoretical and Experimental temperatures over time

The theoretical model predicted the mass flow rate of the system well, with a slight overshoot at 1 000 s, where the simulation model readjusted itself to follow the experimental mass flow rate more accurately from this point onwards. This initial overshoot is caused by the working fluid gaining initial heat from the heating elements, increasing the density gradient before the working fluid can transport the heat fast enough around the loop to decrease the density gradient (see Figure 39 (a)).

The theoretical program simulated the working fluid temperatures well for the single-phase experiment. The theoretical temperature BC and BE is lower than that of the experimental temperature BC and BE. This is because the heat loss to

the environment on the vertical right hand side and bottom horizontal section is larger than that of the experimental setup (see Figure 39 (b)).

### 5.3 Conclusion summary

The mathematical simulation program was used to simulate the experimental results from the benchmark experiment and experimental set 2 (see Section 5.2.2). The mathematical simulation program was, first, calibrated to a benchmark experiment and different void fraction models and frictional multiplier coefficients were first tested to choose the most appropriate model for predicting the separated two-phase flow region of the working fluid. It was concluded that using the Lockhart-Martinelli void fraction and Friedel frictional multiplier was the most accurate method of predicting the flow. It was also noted that the Homogenous void fraction model was fairly accurate compare to the Lockhart-Martinelli void fraction method. When comparing the mathematical simulation model with the experimental results, the mathematical model predicts the single-phase region of the working fluid adequately, and the simulation program predicts the average separated two-phase flow region of the working fluid reasonably accurately. Because of the difficulty of predicting the separated two-phase flow regime of the system, it is suggested that a thermosyphon loop is designed to stay in the single-phase region, and that the two-phase region is only used as a failsafe. The ability of the thermosyphon loop to transfer a large amount of heat without boiling was seen in this system, where the heating element was turned on to its maximum power of 18 300 W, and the condenser's cooling water flow was largely restricted, to enable the system to boil.

## 6 CONCLUSION

The main focus of this project was an investigation into a full-scale 27 m x 6 m thermosyphon loop that can be used as a fully passive reactor cavity cooling system (RCCS). Thermosyphon loops are closed thermodynamic systems in which the working fluid is naturally circulated by the temperature difference density gradient around the loop.

The first objective of this project was to conduct a literature survey to understand and determine the best method to predict the flow inside a thermosyphon loop theoretically. There is a large amount of published literature regarding thermosyphon loops and their theoretical modelling. The methodology and assumptions collected from the literature review were sufficiently extensive to enable the development of a simple and accurate theoretical simulation model.

The second objective of this project was to recommission a full-scale thermosyphon loop, with heating elements simulating the heat from the reactor and condensers simulating the heat removal, and to conduct experiments on the system under various conditions. The recommissioning of the loop included the replacement of old PVC pipes, loosening the electric motors after they had been non-operational for some years, and replacing the four main thermocouples with T-type thermocouples.

The third objective was to operate the recommissioned loop under various heating and cooling conditions. Two series of experiments were conducted. The first set of experiments was conducted with the top right vertical condenser activated from the start of the experiment; the position of the activated condenser is the most common in the literature study. The second experimental sets were done with the top right-hand horizontal condenser activated from the start, which is proposed by Dobson (2006) for the cavity cooling system. Each operating condition was repeated three times and each repetition showed similar results. These experiments showed the ability of the thermosyphon loop to be a passive cooling system, which reduce the safety issue related to human error.

The experimental results also indicate that the thermosyphon loop is capable of transporting 18 300 W of heat with ease. This was illustrated by the condenser cooling water, which was controled to flow close to the smallest flow rate that would get the system to start boiling. If the flow rate was greater than 0.05 L/s, the system would not boil. It was also found that, in all the experiments, the single-phase flow rate of the working fluid reached an approximate maximum flow rate of 0.1 kg/s, regardless of the condenser position, and the transition to the maximum heat input. Thus, the maximum mass flow rate was reached with the heat input set to maximum from the start, or gradually increased. The flow regimes of the experiments were observed through the top vertical heating section sight glass at different points in time. The flow patterns were established, and it was observed that geysering and chugging were the main causes of pressure



fluctuations in the system. Geysering also made the separated two-phase mass flow rate region difficult to simulate. The working fluid was also observed to reach full annular-flow before the power was turned off.

The fourth objective was to write a computer program for simulating the transient behaviour of the working fluid inside the loop. The theoretical model and the experimental results were then compared. The mathematical model that had been created made the following main assumptions: The diameter of the pipe was small enough to use a one-dimensional approach, the flow would be quasi-static, and the expansion tank would not have an effect on the system. A control-based analysis was done, where the loop was divided into axially symmetrical control volumes. The property functions and the three conservation equations, namely, mass, momentum and energy, were applied to these control volumes. The equations of change were then formulated explicitly. The equations to determine the heat transfer coefficients,  $h$ , void fraction,  $\alpha$ , two-phase flow frictional multiplier,  $\phi^2$ , and friction factors,  $C_f$ , were found in the literature. The literature survey showed that the simplest method of predicting the flow inside the loop is by means of a separated flow model, of which the simplest one is the homogeneous model.

To determine the unknown variables of the system, a benchmark experiment was chosen for calibrating the program. Multiple void fraction models and frictional multipliers were compared, and it was concluded that the Lockhart-Martinelli void fraction correlation and the Friedel friction multiplier were the most effective method to predict the separated two-phase flow region of this system. It was found that the seemingly “inaccurate” Homogeneous model, as claimed by the literature, was not as inaccurate for this system. The void fraction and frictional multiplier coefficient gave very similar results.

The theoretical results also indicate that the heat transfer coefficients have a considerable effect on the flow behaviour and heat transfer of the fluid. The properties of the physical structure, not only heat transfer but also heat capacity, have a great effect on the mass flow rate of the working fluid. The single-phase heat transfer coefficients had a greater effect on the system than the two-phase flow coefficients did.

The calibrated mathematical model was compared to the second set of experimental data. The theoretical simulation predicted the working fluid temperatures more accurately for the benchmark experimental results than the experimental set 2 did. The theoretical simulation predicted the flow of the experimental set 2 more accurately than the benchmark experiment did. In the benchmark experiment, the physical structure of the thermosyphon loop had sufficient time to reach very high temperatures before the cooling water was activated. In the second set of experiments, the condenser cooling water was activated from the start of the simulation, and the structural temperature did not increase as much. The theoretical model predicted the reduction in mass flow rate in the system, when the flow went into the separated two-phase flow region. This

was caused by the two-phase frictional multiplier. In the second set of experiments, the experimental mass flow rate went down to zero and, at 10 800 s experienced a sudden rise, before returning to zero again. The theoretical model predicted two smaller mass flow rate increases, at an earlier stage. The theoretical mass flow rate which is out of phase with the experimental mass flow rate is an indication that the thermal capacity of the system and friction are not accurately represented by the mathematical model.

When the working fluid entered the separated two-phase flow region, vapour and liquid were present inside the system. The agitation of the liquid vapour mixture due to the increase vapour flow rate caused the heat transfer of the system to increase rapidly, compared to the increase in the single-phase region. The separated two-phase region of the system provides the thermosyphon loop with an additional “safety feature”. Thus, when a situation occurs that the heat input to the working fluid is greater than expected and the working fluid enters the separated flow region, the heat transfer coefficient is increased, which causes the thermosyphon loop to remove heat at a greater rate and return the working fluid back to the single-phase region. Because the separated two-phase flow region of the thermosyphon loop is very difficult to simulate, it is proposed that a thermosyphon loop that stays in the single-phase region be designed and that the two-phase flow region serve as a failsafe for times when too much heat is added to the system.

In conclusion, the simple one-dimensional theoretical model can predict the internal temperatures and mass flow rate of the thermosyphon loop quite accurately, with a few areas of uncertainty. These areas are the pressure of the system, and the friction coefficient. The loop also indicated that it can remove 18 300 W of heat with ease, so, a series of such loops are good candidates for a high temperature reactor (HTR) cavity cooling system (RCCS) (see Section 1.2, Figure 2).

## 7 RECOMMENDATIONS FOR FUTURE WORK

The investigation into the full-scale thermosyphon loop highlighted areas that may be introduced to increase the validation of the application of such loops for an RCCS. In this section, recommendations for the physical experimental setup and mathematical simulation model are made, in order to improve research into these systems.

### 7.1 Condenser water

The condenser cooling water is controlled by ball valves positioned at the bottom of the loop. The constant header tank at the top gives the driving force for the cooling water through the condensers. The flow rate is measured using a stopwatch and a bucket. This method of measuring the flow makes slight flow adjustments tedious and time consuming. A better method for cooling the thermosyphon loop needs to be used to ensure accuracy.

The condensers, which were not used in the experiments, were still filled with static cooling water. These water sleeves cause natural circulation inside the condensers, which needs to be addressed. It is suggested that the current condensers are replaced by a condenser that can be drained of excess water. The mathematical model could also be updated by a more complex model, to simulate the natural convection in these water sleeves.

### 7.2 Environmental losses

The position of the thermosyphon loop outside, against the side of a building, makes calculating the natural convection on the outside of the loop almost impossible to do accurately. The loop should be built in a controlled environment, where there the surrounding temperature is constant, and there is no wind.

### 7.3 Mass flow rate measurement

A more sensitive mass flow rate measurement device, which does not include an orifice plate, should be used. The orifice plate disturbs the flow inside the pipe. Devices, such as high-speed cameras, hot-film anemometers or laser optical equipment, can be used.

### 7.4 Mathematical model

The mathematical model could be updated to include the two-dimensional heat transfer inside the physical structure of the loop. The program should be adapted so that it can calculate mass flow rate with void fractions greater than one. The flow losses, such as friction loss and minor losses, should be addressed by finding appropriate frictional energy loss coefficients.

## 8 REFERENCES

- Abreu, S.L. & Colle, S. 2004. An experimental study of two-phase closed thermosyphons for compact solar domestic hot-water systems. *Solar Energy*. 76(1–3):141–145.
- Baroczy, C.J. 1963. *Correlation of liquid fraction in two-phase flow with application to liquid metals*. Vol. 61.
- Batty, J.C. & Folkman, S.L. 1983. *Food Engineering Fundimental*. John Wiley & Sons.
- Bieliński, H. 2016. Validation of the generalized model of two-phase thermosyphon loop based on experimental measurements of volumetric flow rate. *Archives of Thermodynamics*. 37(3):109–138.
- Bird, R.B., Stewart, W.E. & Lightfoot, E.N. 1960. *Transport Phenomena*. [Online], Available: <http://books.google.com/books?id=KtsIAQAIAAJ>.
- Boure, J.A., Bergles, A.E. & Tong, L.S. 1973. Review of two-phase flow instability. *Nuclear Engineering and Design*. 25:165–192.
- Butterworth, D. 1975. A COMPARISON OF SOME VOID-FRACTION RELATIONSHIPS FOR CO-CURRENT GAS-LIQUID FLOW. 1:845–850.
- Cao, Y. & Gao, M. 2002. Wickless network heat pipes for high heat flux spreading applications. *International Journal of Heat and Mass Transfer*. 45(12):2539–2547.
- Carey, V.P. 1992. *Liquid-Vapor Phase-Change Phenomena*. First Eddi ed. Bristol: Hemisphere Publishing Corporation.
- Cengel, Y.A. & Cimbala, J.M. 2014. *Fluid Mechanics*. Third eddi ed. Singapore: MC Graw Hill.
- Cengel, Y.A. & Ghajar, A.J. 2012. *Heat and Mass Transfer*. Fifth ed. MC Graw Hill.
- Chen, J.C. 1966. Correlation for boiling heat transfer to saturated fluids in convective flow. *Industrial and Engineering Chemistry Process Design and Development*. 5(3):322–329.
- Chen, S.L., Gerner, F.M. & Tien, C.L. 1987. General film condensation correlations. *Experimental Heat Transfer*. 1(2):93–107.
- Cicchitti, A., Lombardi, C., Silvestri, M., Soldaini, G. & Zavattarelli, R. 1960.

- Two-phase cooling experiments: pressure drop, heat transfer and burnout measurements. *Energia Nucleare*. 7(6):407–425.
- Dobson, R.T. 2006. A novel closed loop thermosyphon heat pipe reactor cavity cooling system for a pebble bed modular reactor. In Kumamoto *8th Int. Heat Pipe Symp.* 397–384.
- Dobson, R. & Ruppertsberg, J. 2007. Flow and heat transfer in a closed loop thermosyphon. Part I—theoretical simulation. *Journal of Energy in Southern Africa*. 18(3):41–48.
- Gnielinski, V. 1976. New equations for heat and mass transfer in turbulent pipe and channel flow.pdf. *International chemical engineering*. 16(2):359–368.
- Goodfellow, M.J., Dewick, P., Wortley, J. & Azapagic, A. 2015. Public perceptions of design options for new nuclear plants in the UK. *Process Safety and Environmental Protection*. 94(C):72–88.
- IAEA. 1991. Safety Related Terms for Advanced Nuclear Plants. *Iaea-Tecdoc-626*. (September):20. [Online], Available: [http://www-pub.iaea.org/MTCD/publications/PDF/te\\_626\\_web.pdf](http://www-pub.iaea.org/MTCD/publications/PDF/te_626_web.pdf).
- Idsinga, W. & Todreas, N. 1977. AN A S S E S S M E N T OF T W O - P H A S E STEAM-WATER SYSTEMS. 3(5):401–413.
- Jaster, H. & Kosky, P.G. 1976. Condensation heat transfer in a mixed flow regime. *International Journal of Heat and Mass Transfer*. 19(1):95–99.
- Journée, B. & Meijers, J. 2018. *Stellenbosch Weather*. [Online], Available: <http://weather.sun.ac.za/>.
- Lee, S.Y. & Kim, Y.L. 1999. An analytical investigation of role of expansion tank in semi-closed two-phase natural circulation loop. 190:353–360.
- Lockhart, R.W. & Martinelli, R.C. 1949. Proposed Correlation of Data for Isothermal Two-Phase, Two-Component Flow in Pipes. *Chemical Engineering Progress*. 45(1):39–48.
- MacAdams, W., Woods, W. & Bryan, R. 1942. Vaporization inside horizontal tubes in benzene-oil mixture. *Trans ASME*. 66(3):671–684.
- Mills, A. & Ganesan, V. 2015. *Heat Transfer*. Pearson.
- NIST Chemistry WebBook*. 2017. [Online], Available: <https://webbook.nist.gov/chemistry/>.

- Petukhov, B.S. 1970. Heat Transfer and Friction in Turbulent Pipe Flow with Variable Physical Properties. *Advances in Heat Transfer*. 6:503–564.
- Ruppersberg, J.C. & Dobson, R.T. 2007. Flow and heat transfer in a closed loop thermosyphon Part II-experimental simulation. *Journal of Energy in Southern Africa*. 18(3):41–48.
- Senda, P.T. 2018. Transient flow, flow pattern characterisation and performance evaluation of a two-phase natural circulation heat transfer loop. Stellenbosch.
- Shah, M.M. 1979. A general correlation for heat transfer during film condensation inside pipes. *International Journal of Heat and Mass Transfer*. 22(4):547–556.
- Shah, M.M. 1984. A correlation for heat transfer during subcooled boiling on a single tube with forced crossflow. *International Journal of Heat and Fluid Flow*. 5(1):13–20.
- Siegrist, M. & Visschers, V.H.M. 2013. Acceptance of nuclear power: The Fukushima effect. *Energy Policy*. 59:112–119.
- Sittmann, I. 2010. INSIDE-PIPE HEAT TRANSFER COEFFICIENT CHARACTERISATION OF A LOOP-TYPE HEAT PIPE SUITABLE FOR THE REACTOR CAVITY COOLING SYSTEM OF THE PEBBLE BED MODULAR REACTOR. Univercity of Stellenbosch.
- Soliman, M., Schuster, J.R. & Berenson, P.J. 1968. A General Heat Transfer Correlation for Annular Flow Condensation. *Journal of Heat Transfer*. 90(2):267–274.
- Sundaram, A.S. & Bhaskaran, A. 2011. Thermal Modeling of Thermosyphon Integrated Heat Sink for CPU Cooling. *Journal of Electronics Cooling and Thermal Control*. 01(02):15–21.
- Thom, J.R.S. 1964. Prediction of pressure drop during forced circulation boiling of water. *International Journal of Heat and Mass Transfer*. 7(7):709–724.
- Traviss, D.P., Rohsenow, W.M. & Baron, A.B. 1973. Forced-Convection Condensation Inside Tubes: a Heat Transfer Equation for Condenser Design. *ASHRAE Transactions*. 79(Part 1):157–165.
- Venkata, J. & Bhramara, P. 2017. ScienceDirect CFD Analysis of Multi turn Pulsating Heat pipe. *Materials Today: Proceedings*. 4(2):2701–2710.
- Verwey, A. 2010. Modelling of a passive Reactor Cavity Cooling System ( RCCS ) for a nuclear reactor core subject to environmental changes and the

optimisation of the by. (March).

- Vijayan, P.K., Patil, A.P., Pilkhwal, D.S., Saha, D. & Venkat Raj, V. 2000. Assessment of pressure drop and void fraction correlations with data from two-phase natural circulation loops. *Heat and Mass Transfer/Waerme- und Stoffuebertragung*. 36(6):541–548.
- Vikas, J., Nayak, A.K., Dhiman, M., Kulkarni, P.P., Vijayan, P.K. & Vaze, K.K. 2013. Role of passive safety features in prevention and mitigation of severe plant conditions in indian advanced heavy water reactor. *Nuclear Engineering and Technology*. 45(5):625–636.
- Vincent, C.C.J. & Kok, J.B.W. 1992. Investigation of the overall transient performance of the industrial two-phase closed loop thermosyphon. *International Journal of Heat and Mass Transfer*. 35(6):1419–1426.
- Whalley, P.B. 1897. *Boiling condensation and gas-liquid flow*. First ed. New York: Oxford University Press.
- Yilmaz, T. 1991. COMPUTERSIMULATION of TWO - PHASE FLOW THERMOSYPHONS ON A R W a T E R H E a T I N G System. 32(2):133–144.
- Zivi, S.M. 1964. Estimation of Steady-State Steam Void-Fraction by Means of the Principle of Minimum Entropy Production. *Journal of Heat Transfer*. 86(2):247–251.

## APPENDIX A DERIVATION OF EQUATIONS

The following sections derive the mathematical form of the equations used in the theoretical simulation model. These equations are: the continuity equation, the momentum equation, the thermal energy equation, heat transfer through a cylindrical shell and the equation used in determining the heat transfer from the water to the support structure of the system.

### A.1 Continuity equation

The conservation of mass is defined as (Bird *et al.* 1960)

$$\left\{ \begin{array}{c} \text{Rate of} \\ \text{mass} \\ \text{accumulation} \end{array} \right\} = \left\{ \begin{array}{c} \text{Rate of} \\ \text{mass} \\ \text{in} \end{array} \right\} - \left\{ \begin{array}{c} \text{Rate of} \\ \text{mass} \\ \text{out} \end{array} \right\} \quad (\text{A.1.1})$$

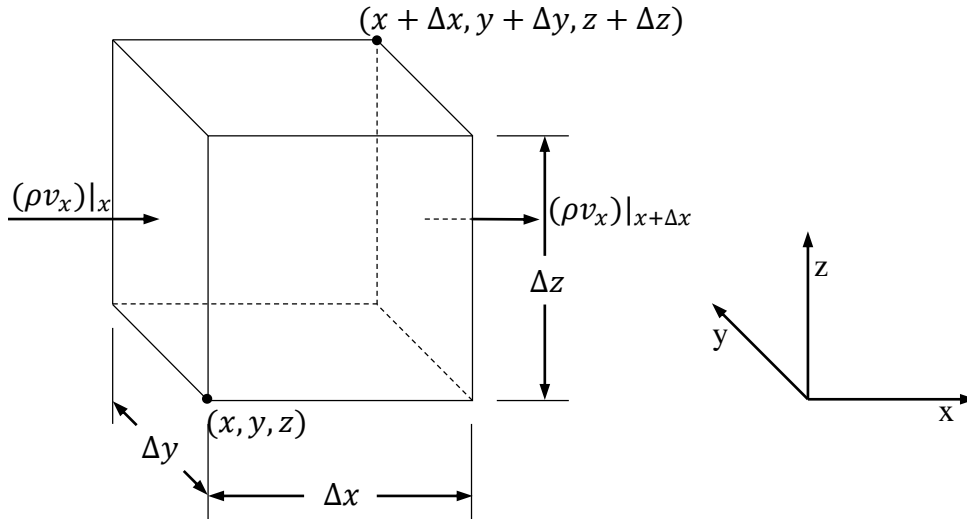


Figure A-1 Region of volume  $\Delta x \Delta y \Delta z$  fixed in space through which a fluid is flowing (in the x-direction)

The rate of mass accumulation in the x-direction, as seen in figure C-1, is given by  $(\rho v_x)|_x \Delta y \Delta z - (\rho v_x)|_{x+\Delta x} \Delta y \Delta z$ , and for all three directions

$$\left( \frac{\partial \rho}{\partial t} \right) (\Delta x \Delta y \Delta z) = \Delta y \Delta z (\rho v_x)|_x - (\rho v_x)|_{x+\Delta x} + \Delta x \Delta z (\rho v_y)|_y - (\rho v_y)|_{y+\Delta y} + \Delta x \Delta y (\rho v_z)|_z - (\rho v_z)|_{z+\Delta z} \quad (\text{A.1.2})$$

Dividing equation A.1.2 by  $(\Delta x \Delta y \Delta z)$  and in the limits as  $\Delta x, \Delta y$  and  $\Delta z$  tends to zero, the equation may be written as



$$\frac{\partial \rho}{\partial t} = - \left( \frac{\partial}{\partial x} \rho v_x + \frac{\partial}{\partial y} \rho v_y + \frac{\partial}{\partial z} \rho v_z \right) \quad (\text{A.1.3})$$

Taking  $m_{cv} = \rho(\Delta x \Delta y \Delta z)$  and the mass flux  $\dot{m}'' = \rho v$  ( kg/m<sup>2</sup>s) the equation A.1.2 becomes (Mills & Ganesan 2015)

$$\left( \frac{\Delta m_{cv}}{\Delta t} \right) = \Delta y \Delta z (\dot{m}''_x \Delta y \Delta z|_x - \dot{m}''_x \Delta y \Delta z|_{x+\Delta x}) + \Delta x \Delta z (\dot{m}''_y|_y - \dot{m}''_y|_{y+\Delta y}) + \Delta x \Delta y (\dot{m}''_z|_z - \dot{m}''_z|_{z+\Delta z}) \quad (\text{A.1.4})$$

or

$$\frac{\Delta m_{cv}}{\Delta t} = \dot{m}_{in} - \dot{m}_{out} \quad (\text{A.1.5})$$

## A.2 Momentum equation

The conservation of momentum is defined as (Bird *et al.* 1960)

$$\left\{ \begin{array}{l} \text{Rate of} \\ \text{momentum} \\ \text{accumulation} \end{array} \right\} = \left\{ \begin{array}{l} \text{Rate of} \\ \text{momentum} \\ \text{in} \end{array} \right\} - \left\{ \begin{array}{l} \text{Rate of} \\ \text{momentum} \\ \text{out} \end{array} \right\} + \left\{ \begin{array}{l} \text{Sum of forces} \\ \text{acting on} \\ \text{system} \end{array} \right\} \quad (\text{A.2.1})$$

The momentum flow through an element can be described by two mechanisms: bulk fluid flow (convection) and velocity gradient (molecular transfer).

For simplicity reasons only the x-component will be shown, and noted that the equation A.2.1 is a vector equation with components in each of the coordinate directions, figure C-2. The rate at which momentum travels through a control volume by entering at face  $x$  by means of convection in the x-direction is given by  $\rho v_x v_x|_x \Delta y \Delta z - \rho v_x v_x|_{x+\Delta x} \Delta y \Delta z$ , and for all the other face as

$$\begin{aligned} & \Delta y \Delta z (\rho v_x v_x|_x - \rho v_x v_x|_{x+\Delta x}) + \Delta x \Delta z (\rho v_y v_x|_y - \rho v_y v_x|_{y+\Delta y}) \\ & + \Delta y \Delta x (\rho v_z v_x|_z - \rho v_z v_x|_{z+\Delta z}) \end{aligned} \quad (\text{A.2.2})$$

The same is done for the rate at which momentum travels through a control volume by means of molecular transfer by entering at face  $x$  in the x-direction as  $\tau_{xx}|_x \Delta y \Delta z - \tau_{xx}|_{x+\Delta x} \Delta y \Delta z$  and is written for all the faces as

$$\begin{aligned} & \Delta y \Delta z (\tau_{xx}|_x - \tau_{xx}|_{x+\Delta x}) + \Delta x \Delta z (\tau_{yx}|_y - \tau_{yx}|_{y+\Delta y}) \\ & + \Delta y \Delta x (\tau_{zx}|_z - \tau_{zx}|_{z+\Delta z}) \end{aligned} \quad (\text{A.2.3})$$

Note that the normal stress  $\tau_{yx}$  is the stress from viscous forces in the x-direction and tangential on the y-face. The only two important forces for the general case is the gravitational force,  $g$  and the pressure,  $P$  from the fluid written as

$$\Delta y \Delta z (P|_x - P|_{x+\Delta x}) + \rho g_x \Delta x \Delta y \Delta z \tag{A.2.4}$$

The rate of accumulation of x-momentum within the element is  $(\partial \rho v_x / \partial t) \Delta x \Delta y \Delta z$ , and substituting equations A.2.2, A.2.3 and A.2.4 into equation A.2.1 gives

$$\begin{aligned} \left(\frac{\partial \rho v_x}{\partial t}\right) \Delta x \Delta y \Delta z = & \Delta y \Delta z (\rho v_x v_x|_x - \rho v_x v_x|_{x+\Delta x}) + \Delta x \Delta z (\rho v_y v_x|_y - \\ & \rho v_y v_x|_{y+\Delta y}) + \Delta y \Delta x (\rho v_z v_x|_z - \rho v_z v_x|_{z+\Delta z}) + \Delta y \Delta z (\tau_{xx}|_x - \tau_{xx}|_{x+\Delta x}) + \\ & \Delta x \Delta z (\tau_{yx}|_y - \tau_{yx}|_{y+\Delta y}) + \Delta y \Delta x (\tau_{zx}|_z - \tau_{zx}|_{z+\Delta z}) + \Delta y \Delta z (P|_x - \\ & P|_{x+\Delta x}) + \rho g_x \Delta x \Delta y \Delta z \end{aligned} \tag{A.2.5}$$

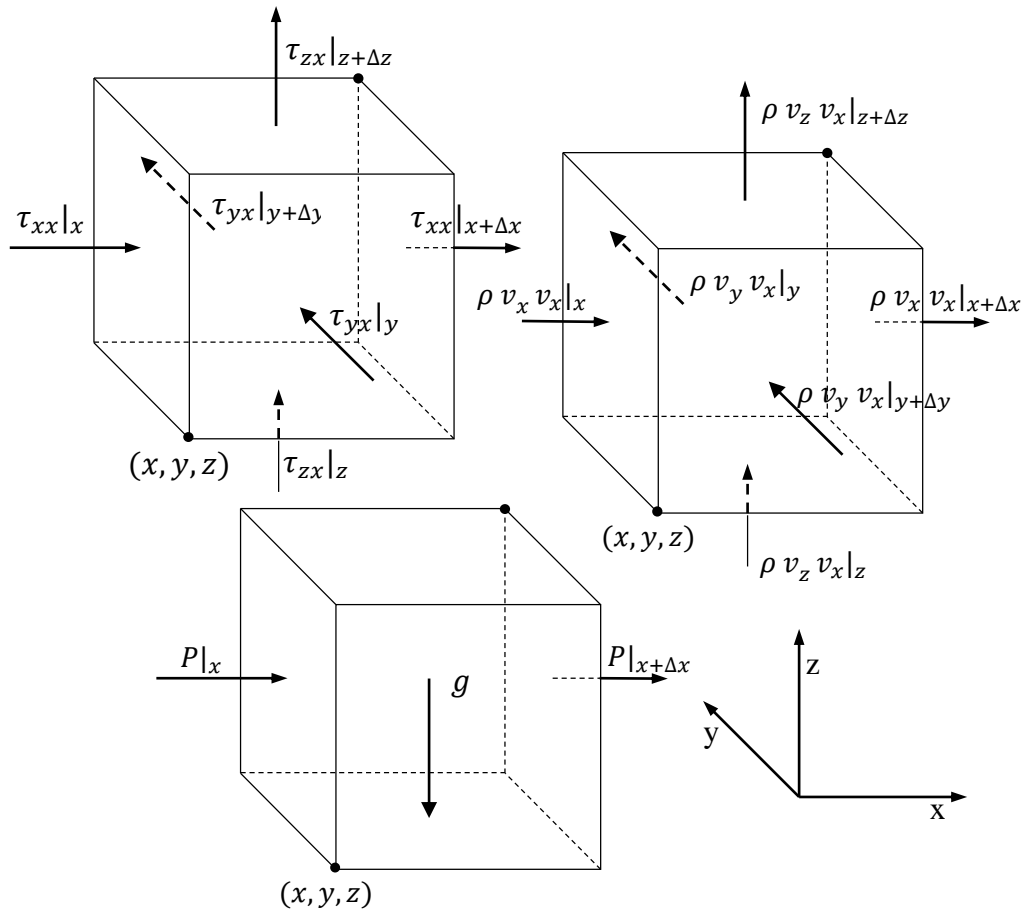


Figure A-2 Region of volume  $\Delta x \Delta y \Delta z$  fixed in space through which a fluid is flowing (in the x-direction)

Dividing equation A.2.5 by the volume  $\Delta x \Delta y \Delta z$  and in the limit of  $\Delta x, \Delta y$  and  $\Delta z$  as tend to zero, equation A.2.5 becomes the momentum equation of the x-component

$$\left( \frac{\partial \rho v_x}{\partial t} \right) = \left( \frac{\partial}{\partial x} \rho v_x v_x + \frac{\partial}{\partial y} \rho v_y v_x + \frac{\partial}{\partial z} \rho v_z v_x \right) - \left( \frac{\partial}{\partial x} \tau_{xx} + \frac{\partial}{\partial y} \tau_{yx} + \frac{\partial}{\partial z} \tau_{zx} \right) + (P|_x - P|_{x+\Delta x}) + \rho g_x \quad (\text{A.2.6})$$

Taking  $m_{cv} = \rho(\Delta x \Delta y \Delta z)$  and the mass flux  $\dot{m}'' = \rho v$  ( kg/m<sup>2</sup>s) (Mills & Ganesan, 2015), equation A.2.5 becomes

$$\begin{aligned} \frac{\Delta m_{cv} v_x}{\Delta t} = & \Delta y \Delta z (\dot{m}_x'' v_x|_x - \dot{m}_x'' v_x|_{x+\Delta x}) + \Delta x \Delta z (\dot{m}_x'' v_y|_y - \\ & \dot{m}_x'' v_y|_{y+\Delta y}) + \Delta y \Delta x (\dot{m}_x'' v_z|_z - \dot{m}_x'' v_z|_{z+\Delta z}) + \Delta y \Delta z (\tau_{xx}|_x - \tau_{xx}|_{x+\Delta x}) + \\ & \Delta x \Delta z (\tau_{yx}|_y - \tau_{yx}|_{y+\Delta y}) + \Delta y \Delta x (\tau_{zx}|_z - \tau_{zx}|_{z+\Delta z}) + \Delta y \Delta z (P|_x - \\ & P|_{x+\Delta x}) + g_x m_{cv} \end{aligned} \quad (\text{A.2.7})$$

Writing equation A.2.7 in one dimension with  $A = \Delta y \Delta z$  gives

$$\frac{\Delta m_{cv} v}{\Delta t} = (\dot{m}v)_{in} - (\dot{m}v)_{out} + (PA) - (PA) + (\tau A) - (\tau A) + gm \quad (\text{A.2.8})$$

### A.3 Derivation of thermal energy

Bird *et al.* (1960) gives the conservation of energy in words as

$$\begin{aligned} \left\{ \begin{array}{l} \text{rate of} \\ \text{increase of} \\ \text{kinetic and} \\ \text{internal} \\ \text{energy} \end{array} \right\} = & \left\{ \begin{array}{l} \text{net rate of kinetic} \\ \text{and internal} \\ \text{energy addition} \\ \text{by convection} \\ \text{transport} \end{array} \right\} + \left\{ \begin{array}{l} \text{neat rate of heat} \\ \text{addition by} \\ \text{molecular} \\ \text{transport} \\ \text{(conduction)} \end{array} \right\} + \\ \left\{ \begin{array}{l} \text{rate of work} \\ \text{done on system} \\ \text{by molecular} \\ \text{mechanisms} \\ \text{(i.e., by stresses)} \end{array} \right\} + & \left\{ \begin{array}{l} \text{rate of work} \\ \text{done on system} \\ \text{by external} \\ \text{forces} \\ \text{(e.g., by gravity)} \end{array} \right\} \end{aligned} \quad (\text{A.3.1})$$

Written in vector and tensor notation (per unit volume), in the same sequence as

$$\frac{\partial}{\partial t} \left( \frac{1}{2} \rho v^2 + \rho \hat{U} \right) = \left( \nabla \cdot \left( \frac{1}{2} \rho v^2 + \rho \hat{U} \right) \mathbf{V} \right) - (\nabla \cdot \mathbf{q}) - (\nabla \cdot \mathbf{p}\mathbf{v}) - (\nabla \cdot [\boldsymbol{\tau} \cdot \mathbf{v}]) + \rho(\mathbf{v} \cdot \mathbf{g}) \quad (\text{A.3.2})$$

or as

$$\frac{\partial}{\partial t}(\rho(u + v^2/2)) + [\nabla \cdot \rho \mathbf{v}(u + v^2/2)] = \dot{Q}_{ht}''' + \rho(\mathbf{v} \cdot \mathbf{g}) - (\nabla \cdot p\mathbf{v}) - (\nabla \cdot [\boldsymbol{\tau} \cdot \mathbf{v}]) \quad [\text{J/m}^3] \quad (\text{A.3.3})$$

The mechanical energy equation is another form of the energy equation and is obtained by taking the momentum equation given as

$$\frac{\partial}{\partial t}(\rho \mathbf{v}) + [\nabla \cdot \rho \mathbf{v}\mathbf{v}] = -\nabla p + \rho \mathbf{g} - (\nabla \cdot p) - [\nabla \cdot \boldsymbol{\tau}] \quad [\text{N/m}^3] \quad (\text{A.3.4})$$

forming the scalar product of equation A.3.4 by using the velocity vector  $\mathbf{v}$ , equation A.3.4 turns into

$$\frac{\partial}{\partial t}(\rho \mathbf{v}) \cdot \mathbf{v} + [\nabla \cdot \rho \mathbf{v}\mathbf{v}] \cdot \mathbf{v} = -\nabla p \cdot \mathbf{v} + \rho \mathbf{g} \cdot \mathbf{v} - (\nabla \cdot p) \cdot \mathbf{v} - [\nabla \cdot \boldsymbol{\tau}] \cdot \mathbf{v} \quad [\text{W/m}^3] \quad (\text{A.3.5})$$

Using the identities

$$(\nabla \cdot p) \cdot \mathbf{v} = (\nabla \cdot p\mathbf{v}) - p(\nabla \cdot \mathbf{v})$$

$$[\nabla \cdot \boldsymbol{\tau}] \cdot \mathbf{v} = \nabla \cdot [\boldsymbol{\tau} \cdot \mathbf{v}] - (\boldsymbol{\tau} : \nabla \mathbf{v})$$

$$\frac{\partial}{\partial t}(\rho \mathbf{v}) \cdot \mathbf{v} = \frac{\partial}{\partial t}\left(\frac{1}{2}\rho v^2\right), \text{ and}$$

$$[\nabla \cdot \rho \mathbf{v}\mathbf{v}] \cdot \mathbf{v} = \left(\nabla \cdot \frac{1}{2}\rho v^2 \mathbf{v}\right)$$

And the continuity equation

$$\frac{\partial \rho}{\partial t} = -(\nabla \cdot \rho \mathbf{v}) \quad [\text{kg/sm}^3]$$

The equation A.3.5 may be written as the mechanical equation

$$\frac{\partial}{\partial t}\left(\frac{1}{2}\rho v^2\right) = -\left(\nabla \cdot \frac{1}{2}\rho v^2 \mathbf{v}\right) - (\nabla \cdot p\mathbf{v}) + \rho(\mathbf{v} \cdot \mathbf{g}) - p(-\nabla \cdot \mathbf{v}) - (\nabla \cdot [\boldsymbol{\tau} \cdot \mathbf{v}]) - (-\boldsymbol{\tau} : \nabla \mathbf{v}) \quad [\text{W/m}^3] \quad (\text{A.3.6})$$

Subtracting equation A.3.2 from equation A.3.6 gives the internal/thermal energy equation

$$\frac{\partial}{\partial t}(\rho \mathbf{u}) = -\nabla \cdot \rho \mathbf{u}\mathbf{v} + \dot{Q}_{ht}''' - p(\nabla \cdot \mathbf{v}) - (\boldsymbol{\tau} : \nabla \mathbf{v}) \quad [\text{W/m}^3] \quad (\text{A.3.7})$$

or, for one-dimensional flow as

$$\frac{\partial}{\partial t}(\rho u) = -\frac{\partial}{\partial z}(\rho uv) + \dot{Q}_{ht}''' - p \frac{\partial v}{\partial z} - \tau_{rz} \frac{\partial v_z}{\partial r} \quad [\text{W/m}^3] \quad (\text{A.3.8})$$

where  $\tau_{rz}$  is the wall shear stress.

The term  $\frac{\partial}{\partial t}(\rho u)$ , is the net increase or net decrease of the internal energy of the control volume, per unit volume. The term  $-p(\nabla \cdot \mathbf{v})$  is the reversible rate of internal energy increasing or decreasing by expansion or compression. When the control volume is compressed the internal energy is increased and when the control volume expands the internal energy decreases, hence an increase and decrease in temperature. The last term  $-(\boldsymbol{\tau} : \nabla \mathbf{v})$  is the rate at which the internal energy increase due to viscous dissipation, such as the work done against friction which causes heat and which always causes the control volumes internal energy to increase. The term  $\dot{Q}_{ht}'''$  is the increase or decrease of internal energy due to heat transfer from conduction or convection from adjacent control volumes, per unit volume. The heat is always transfer from the higher temperature to the lower temperature. The heat transfer is positive into the control volume and negative out.

Writing equation A.3.8 for a finite sized one-dimensional cylindrical control volume that consist of a cross-sectional area  $A_x$ , with a radius,  $r$ , and a length  $\Delta z$  as

$$\frac{\Delta}{\Delta t}(mu) = -\Delta(\dot{m}u) + \dot{Q}_{ht} - pA_x\Delta v - \bar{\tau}_w A_z \bar{v} \quad [\text{W}] \quad (\text{A.3.9})$$

where  $A = \pi r^2$ ,  $A_z = \wp \Delta z$ , and the perimeter  $\wp = 2\pi R$  and  $\tau_{rz@r=R} = \bar{\tau}_w$  the so-called wall stress, and  $\bar{v}$  is the average velocity long its length  $\Delta z$ .

#### A.4 Heat conduction through a cylindrical shell

The energy equation for a closed system, with potential and kinetic energy egnoed and assuming an incompressible solid with density constant over time, is given as (Mills & Ganesan 2015)

$$\Delta U = \dot{Q}\Delta t + \dot{Q}_v \Delta t \quad (\text{A.4.1})$$

Where the change in internal energy  $\Delta U$  is equal to the net heat transfer,  $\dot{Q}\Delta t = \dot{Q}_{in} - \dot{Q}_{out}$  and the heat generated within the system,  $\dot{Q}_v\Delta t$ . Dividing by  $\Delta t$  and in the limit of  $\Delta t$  as tends to zero, equation A.4.1 becomes

$$\frac{dU}{dt} = \dot{Q} + \dot{Q}_v \quad (\text{A.4.2})$$

Given that the system has a fixed mass, the mass can be calculated as,  $m = \rho V$ . The change in internal energy can then be written as  $dU = \rho V du$ , where  $u$  is the specific internal energy [J/kg]. For an incompressible solid  $du = c_v dT$ , where  $c_v$  is the constant volume specific heat [J/kg K] and  $T$  [K] is the temperature. The equation A.4.2 can be written as

$$\rho V c \frac{dT}{dt} = \dot{Q} + \dot{Q}_v \quad (\text{A.4.3})$$

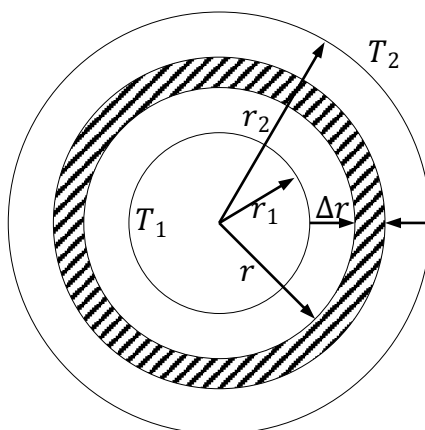


Figure A-3 A cylindrical shell showing an elemental control volume for application of the energy conservation principle

Figure C-3 shows a cylindrical shell of the length  $L$ , with an inner and outer radius  $r_1$  and  $r_2$  respectively. The area can be calculated as,  $A = 2 \pi r L$ . The inner and outer surface temperature is maintained at  $T_1$  and  $T_2$  respectively. There is a control volume located between radius  $r$  and  $r + \Delta r$ . If there is no internal energy source ( $\dot{Q}_v = 0$ ) and the temperature is unchanging in time and in accordance with equation A.4.3, the heat transfer across the face at  $r$  needs to be equal to the heat transfer crossing the face at  $r + \Delta r$ . This can be written as

$$\dot{Q}|_r = \dot{Q}|_{r+\Delta r} \quad (\text{A.4.4})$$

Using Fourier's law

$$\dot{Q} = Aq = 2\pi r L \left( -k \frac{dT}{dr} \right) \quad (\text{A.4.5})$$

dividing by  $2 \pi k L$  and assuming  $k$  is independent of temperature gives

$$\frac{\dot{Q}}{2 \pi k L} = -r \frac{dT}{dr} = \text{constant} = C_1 \quad (\text{A.4.6})$$

Equation A.4.6 is a first order differential equation for  $T(r)$ . Integrating gives

$$T = -C_1 \ln(r) + C_2 \quad (\text{A.4.7})$$

Determining  $C_1$  using boundary conditions give

$$C_1 = \frac{T_1 - T_2}{\ln\left(\frac{r_2}{r_1}\right)} \quad (\text{A.4.8})$$

Substituting equation A.4.8 back into equation A.4.6 gives

$$\dot{Q} = \frac{2 \pi k L (T_1 - T_2)}{\ln\left(\frac{r_2}{r_1}\right)} \quad (\text{A.4.9})$$

The thermal resistance is then

$$R = \frac{\ln\left(\frac{r_2}{r_1}\right)}{2 \pi k L} \quad (\text{A.4.10})$$

## A.5 Internal energy of structure

From the conservation of energy equation for a closed system and no internal heat generation ( $\dot{Q}_v = 0$ ), equation A.4.1 becomes

$$\frac{dU}{dt} = \dot{Q}_{total} \quad (\text{A.5.1})$$

where

$$\frac{dU}{dt} = \frac{d(mu)}{dt} = u \frac{dm}{dt} + m \frac{du}{dt} \quad (\text{A.5.2})$$

Since the control volumes represent solid material

$$\frac{dm}{dt} \approx 0$$

$$\text{thus } \frac{dU}{dt} = m \frac{du}{dt} = m c \frac{dT}{dt} \quad (\text{A.5.3})$$

substituting into equation A.5.2 and integrating with respect to time

$$\int_t^{t+\Delta t} (\dot{Q}_{total}) dt = m c \int_{T^t}^{T^{t+\Delta t}} dT$$

$$\Delta(\dot{Q}_{total}) = m c (T^{t+\Delta t} - T^t) \quad (\text{A.5.4})$$

Rearranging the equation gives

$$T^{t+\Delta t} = T^t + \frac{\Delta t}{m c} (\dot{Q}_{total}) \quad (\text{A.5.5})$$

Multiplying with  $c$  and writing in terms of specific internal energy gives

$$U^{t+\Delta t} = U^t + \frac{\Delta t}{m} (\dot{Q}_{total}) \quad (\text{A.5.6})$$

## A.6 CISE correlation

Whalley (1897) gives used a correlation for the void fraction,  $\alpha$  in terms of a slip ratio  $S$ . The void fraction is given as

$$\alpha = \frac{1}{1 + \left( S \frac{1-x\rho_g}{x\rho_l} \right)} \quad (\text{A.6.1})$$

The slip ratio  $S$  is given as

$$S = 1 + E_1 \left( \frac{y}{1+yE_2} - yE_2 \right)^{0.5} \quad (\text{A.6.2})$$

where

$$y = \frac{\beta}{1-\beta}$$

$$\beta = \frac{\rho_l x}{\rho_l x + \rho_g (1-x)}$$

$$E_1 = 1.578 Re^{-0.019} \left( \frac{\rho_l}{\rho_g} \right)^{0.22}$$

$$E_2 = 0.0273 We Re^{-0.51} \left( \frac{\rho_l}{\rho_g} \right)^{-0.08}$$

where  $x$  is the quality;  $\rho_l$  is the density of the liquid phase,  $\rho_g$  is the density of the vapour;  $Re$  is the Reynolds number given as

$$Re = \frac{v d \rho}{\mu}$$

and the Weber number as

$$We = \frac{(v \rho)^2 d}{\sigma \rho_l}$$

where  $v$  is the total (liquid + vapour) velocity of the fluid;  $d$  is the pipe diameter;  $\sigma$  is the surface tension and  $\mu_l$  is the liquid viscosity.



## A.7 Friedel correlation for frictional two-phase multiplier

The Friedel correlation factor (Whalley 1897) is written in terms of the two-phase multiplier

$$\phi_{lo}^2 = \frac{(-dp/dz)_F}{(-dp/dz)_{lo}}$$

where  $(-dp/dz)_F$  is for the total friction gradient (fluid + vapour) and  $(-dp/dz)_{lo}$  is the liquid only pressure drop. The friction correlation is given as

$$\phi_{lo}^2 = E + \frac{3.24 F H}{Fr^{0.045} We^{0.035}} \quad (A.7.1)$$

$$E = (1 - x)^2 + x^2 \frac{\rho_l C_{fgo}}{g C_{flo}}$$

$$F = x^{0.78} (1 - x)^{0.224}$$

$$H = \left(\frac{\rho_l}{\rho_g}\right)^{0.91} \left(\frac{\mu_g}{\mu_l}\right)^{0.9} \left(1 - \frac{\mu_g}{\mu_l}\right)^{0.7}$$

$$Fr = \frac{(\rho v)^2}{g d \rho_h^2}$$

$$We = \frac{(v \rho)^2 d}{\sigma \rho_h}$$

And

$$\rho_h = \left(\frac{x}{\rho_g} + \frac{1-x}{\rho_l}\right)^{-1}$$

For these formulas  $x$  is the quality of the fluid;  $\rho_g$  is the density of the vapour;  $\rho_l$  is the density of the liquid;  $C_{fgo}$  and  $C_{flo}$  is the vapour only and liquid only friction factors respectively;  $\mu_g$  is the vapour viscosity;  $\mu_l$  is the liquid viscosity;  $g$  is the gravitational acceleration and  $\sigma$  is the surface tension.

## APPENDIX B THEORETICAL PROGRAM ALGORITHM

This appendix gives the sequence of steps in which the theoretical program was written.

**Step 1** Referring to figure 8, the dimensions of the loop are defined.

*Define dimensions*

$$L_{updown} = 26.925 ; L_{hori} = 5.972 ; L_{expansion} = 27.56$$

$$D_1 = 0.0478; D_2 = 0.051; D_3 = 0.06; D_4 = 0.16; D_5 = 0.165; D_{ci} = 0.081; D_{co} = 0.085; r_1 = \frac{D_1}{2}; r_2 = \frac{D_2}{2}; r_3 = \frac{D_3}{2}; r_4 = \frac{D_4}{2}; r_5 = \frac{D_5}{2}; r_{ci} = \frac{D_{ci}}{2}; r_{co} = \frac{D_{co}}{2}$$

*Control volume numbers*

$$N_1 = 20 ; N_2 = 45 ; N_3 = 20 ; N_4 = 45 ; N_{tot} = N_1 + N_2 + N_3 + N_4$$

*Control volume length*

$$\Delta L_{hori1} = \frac{L_{hori}}{N_1} ; \Delta L_{hori2} = \frac{L_{hori}}{N_3} ; \Delta L_{updown1} = \frac{L_{updown1}}{N_2} ; \Delta L_{updown2} = \frac{L_{updown2}}{N_4}$$

**Step 2** Define initial values of the variables

The initial conditions are dependent on the experimental data chosen to simulate, these conditions change per experiment. The values show are just an example.

$$T_{amb} = f(t) ; T_{iniLeft} = 21 ; T_{iniright} = 20 ; T_{iniTop} = 20 ; T_{iniBotom} = 20$$

$$T_{iniStructure} = 28 ; T_{iniWS} = 28; x_{ini} = 0 ; \dot{m} = 0 ; ALPHA_{ini} = 0; \Delta t = 0.1$$

Atmospheric pressure

$$P_{atm} = 101 [kpa]$$

**Step 3** Define the specific experiment calibration variables

$$\text{AlphaLimiter} = 0.2; \text{FrictionMultiplier} = 6$$

**Start time step loop**

$$\text{For } i = 0 \text{ to } N_{tot} ; m_i^{t+\Delta t} = m_i^t + \Delta t * \left(\frac{\Delta m}{\Delta t}\right)_i^{t-\frac{\Delta t}{2}} ; P_i^{t+\Delta t} = P_i^t + \Delta t * \left(\frac{\Delta P}{\Delta t}\right)_i^{t-\frac{\Delta t}{2}}$$

Set boundary conditions

$$m_{i=0}^{t+\Delta t} = m_{i=N_{tot}}^{t+\Delta t} ; P_{i=0}^{t+\Delta t} = P_{i=N_{tot}}^{t+\Delta t} ; m_{i=N_{tot}+1}^{t+\Delta t} = m_{i=1}^{t+\Delta t} ; P_{i=N_{tot}+1}^{t+\Delta t} = P_{i=1}^{t+\Delta t}$$

**Step 4** Calculate the heat losses to the environment

Calculate the heat transfer coefficients for flow inside pipe

For  $i = 0$  to  $N_{tot}$

$$Pr = f(T_i) ; k_i = f(T_i)$$

$$\beta_i = \frac{1}{T_i + 273.15}$$

$$V_i = \frac{\dot{m}}{A_x} ; Re = \frac{V * D_1 * \rho_i}{\mu_{li}}$$

If  $Re < 2300 ; Nu = 3.66$

If  $Re > 2300 ;$

$$Nu = 0.023 Re^{0.8} Pr^{0.4}$$

$$h_i = k_i Nu / D_1$$

Evaporator (left-hand) side heat transfer coefficient when boiling occurs in vertical pipe

if  $(x > 0 \ \&\& \ x < 1 \ \&\& \ i > N_1 \ \&\& \ i < N_1 + N_2)$

$$Re_{i,l} = \frac{v_i(l-x)D_1\rho_{i,l}}{\mu_{i,l}}$$

$$h_l = 0.023 \left(\frac{k_l}{D}\right) Re_{i,l}^{0.8} Pr_{i,l}^{0.4}$$

$$X_{tt} = \left(\frac{1-x}{x}\right)^{0.9} \left(\frac{\rho_v}{\rho_l}\right)^{0.5} \left(\frac{\mu_l}{\mu_v}\right)^{0.1}$$

$$Re_{i,lv} = \frac{v_i D_1 \rho_i}{\mu_i}$$

$$F = 2.35 \left(0.213 + \frac{1}{X_{tt}}\right)^{0.736}$$

$$h_{mac} = h_l F$$

$$Re_{tp} = Re_{i,l} F^{1.25}$$

$$h_{lv} = 0.023 \left( \frac{k_l}{D} \right) Re_{lv}^{0.8} Pr_l^{0.4}$$

$$S = (1 + 2.56 \cdot 10^{-6} Re_{tp}^{1.17})^{-1}$$

$$h_{mic} = 0.00122 \left[ \frac{k_{i,l}^{0.79} c_{pl}^{0.45} \rho_{i,l}^{0.4}}{\sigma^{0.5} \mu_{i,l}^{0.9} h_{lv}^{0.24} \rho_{i,v}^{0.24}} \right] [P_{sat}(T_i) - P_i]^{0.75} [T_i - T_{sat}(P_i)]^{0.24} S$$

$$h_i = h_{mic} + h_{mac}$$

Calculate the thermal resistance and heat loss

Bottom horizontal pipe

For  $i = 0$  to  $N_1$

$$k_{pw} = 14 ; h_{oc} = 5 ; h_{or} = h_{oc} * 0.53$$

$$R_{pw} = \frac{\log \frac{r_2}{r_1}}{k_{pw} L \pi 2} ; R_{wf} = \frac{1}{h_i A Z_{wf}}$$

$$R_{oc,pw} = \frac{1}{h_{oc} A Z_{opw}} ; R_{or,pw} = \frac{1}{h_{or} A Z_{opw}}$$

$$R_{eq,rc} = \frac{1}{\frac{1}{R_{oc,pw}} + \frac{1}{R_{or,pw}}}$$

Heat loss for bottom of loop

$$\dot{Q}_{loss,i} = \frac{T_{wf,i} - T_{amb}}{R_{pw} + R_{wf} + R_{eq,rc}}$$

Top horizontal and right vertical pipe

For  $i = N_1 + N_2$  to  $N_{tot}$

$$Pr_{ccw,i} = f(T_{ccw,i}) ; k_{ccw,i} = f(T_{ccw,i})$$

$$h_{oc} = 5 ; h_{or} = h_{oc} * 0.53 ; k_{ccw} = 14$$

$$\beta_{ccw,i} = \frac{1}{T_{ccw,i} + 273.15}$$

$$Re_{ccw} = \frac{g(T_{ccw,i} - T_{pw,i})(t_{ccw})^3 \rho_{ccw,i}}{\mu_{ccw,i}} Pr_{ccw,i}$$

Left vertical pipe

$$\text{if}(i > N_1 + N_2 \ \&\& \ i < N_1 + N_2 + N_3)$$

$$Nu_{ccw,i} = 0.069 Re_{ccw,i}^{0.333} Pr_{ccw,i}^{0.074}$$

Top horizontal pipe

$$\text{if}(i > N_1 + N_2 + N_3 \ \&\& \ i < N_{tot})$$

$$Nu_{ccw,i} = 0.046 Re_{ccw,i}^{0.333}$$

$$h_{ccw,i} = \frac{Nu_{ws} k_{ws}}{t_{ws}}; R_{ws} = \frac{1}{h_{ws} A_{Z_{ws}}}$$

$$R_i = \frac{1}{h_i A_{Z_{ipw}}}; R_{pw} = \frac{\log \frac{r_2}{r_1}}{k_{pw} L \pi 2}; R_{ccw} = \frac{\log \frac{r_{co}}{r_{ci}}}{k_{iw} L \pi 2}; R_{oc,cw} = \frac{1}{h_{oc} A_{Z_{ocw}}}; R_{or,cw} = \frac{1}{h_{or} A_{Z_{cow}}}; R_{eq,rc} = \frac{1}{\frac{1}{R_{oc,cw}} + \frac{1}{R_{or,cw}}}$$

New internal energy of cooling water

$$m_{ccw,i} = \rho_{ccw,i} V_{ccw,i}; m_{pw} = \rho_{ss} V_{pw}; m_{cw} = \rho_{ss} V_{cw}$$

$$\dot{Q}_{wf,pw,i} = \frac{T_i - T_{pw,i}}{R_i + \frac{R_{pw,i}}{2}}; \dot{Q}_{pw,ccw,i} = \frac{T_i - T_{pw,i}}{\frac{R_{ccw,i}}{2} + \frac{R_{pw,i}}{2}}$$

$$\dot{Q}_{ccw,pw,i} = \frac{T_{pw,i} - T_{ccw,i}}{\frac{R_{ccw,i}}{2} + \frac{R_{pw,i}}{2}}; \dot{Q}_{ccw,cw,i} = \frac{T_{cw,i} - T_{ccw,i}}{R_{ccw,i} + \frac{R_{cw,i}}{2}}$$

$$\dot{Q}_{cw,ccw,i} = \frac{T_{ccw,i} - T_{cw,i}}{\frac{R_{ccw,i}}{2} + \frac{R_{cw,i}}{2}}; \dot{Q}_{cw,surr} = \frac{T_{amb} - T_{cw,i}}{\frac{R_{cw,i}}{2} + R_{eqrc}}$$

$$u_{pw,i}^{t+\Delta t} = \left( u_{pw,i}^t + \Delta t \frac{\dot{Q}_{wf,pw,i} + \dot{Q}_{pw,ccw,i}}{m_{pw,i}} \right)$$

$$u_{ccw,i}^{t+\Delta t} = \left( u_{ccw,i}^t + \Delta t \frac{\dot{Q}_{ccw,pw,i} + \dot{Q}_{ccw,cw,i}}{m_{ccw,i}} \right)$$

$$u_{cw,i}^{t+\Delta t} = \left( u_{cw,i}^t + \Delta t \frac{\dot{Q}_{cw,ccw,i} + \dot{Q}_{cw,surr,i}}{m_{cw,i}} \right)$$

Heat loss of internal fluid for top and right part of loop

$$\dot{Q}_{loss,i} = \frac{T_i - T_{amb}}{R_i + \frac{R_{pw,i}}{2}}$$

Thermal resistance for evaporator section

For  $i = N_1$  to  $N_1 + N_2$

$$h_{oc} = 5; h_{or} = h_{oc} 0.53; k_{cw} = 14$$

$$k_{ins} = 0.036; k_e = 11.3; k_{clad} = 11.3$$

$$R_{piwc} = \frac{1}{h_i A z_{piw}}; R_{pw} = \frac{\log \frac{r_2}{r_1}}{k_{pw} L \pi 2}; R_e = \frac{\log \frac{r_3}{r_2}}{k_e L \pi 2}; R_{ins} = \frac{\log \frac{r_4}{r_3}}{k_{ins} L \pi 2}; R_{ins} = \frac{\log \frac{r_4}{r_3}}{k_{ins} L \pi 2}$$

$$R_{clad} = \frac{\log \frac{r_5}{r_4}}{k_{clad} L \pi 2}; R_{oc,clad,i} = \frac{1}{h_{oc} A z_{clad,ow}}; R_{or,clad,i} = \frac{1}{h_{or} A z_{clad,ow}}$$

$$R_{eq,rc} = \frac{1}{\frac{1}{R_{oc,clad,i}} + \frac{1}{R_{or,clad,i}}}$$

New internal energy of heating element and pipe wall

$$m_{pw} = \rho_{ss} V_{pw}; m_e = \rho_e V_e$$

$$\dot{Q}_{wf,pw,i} = \frac{T_i - T_{pw,i}}{R_i + \frac{R_{pw,i}}{2}}; \dot{Q}_{pw,e,i} = \frac{T_{e,i} - T_{pw,i}}{\frac{R_{e,i}}{2} + \frac{R_{pw,i}}{2}}$$

$$\dot{Q}_{e,pw,i} = \frac{T_{pw,i} - T_{e,i}}{\frac{R_{e,i}}{2} + \frac{R_{pw,i}}{2}}; \dot{Q}_{e,surr} = \frac{T_{amb} - T_{e,i}}{R_{ins,i} + R_{clad,i} + \frac{R_{e,i}}{2} + R_{eqrc}}$$

$$u_{pw}^{t+\Delta t} = \left( u_{pw}^t + \Delta t \frac{\dot{Q}_{ipw} + \dot{Q}_{pwe}}{m_{pw}} \right)$$

$$u_e^{t+\Delta t} = \left( u_e^t + \Delta t \frac{\dot{Q}_{epw} + \dot{Q}_{eo} + \dot{Q}_r}{m_e} \right)$$

Heat loss of internal fluid left side of loop

$$\dot{Q}_{r,i} = \frac{T_i - T_{pw}}{R_{piwc} + \frac{R_{pw}}{2}}$$

**Step 5** Calculate the new internal energy of the working fluid

Calculate reversible work rate

For  $i = 0$  to  $N_{tot}$

if  $\dot{m} \geq 0$

$$\left(\frac{P}{\rho}\right)_{i,out}^t = \frac{P_{i+1/2}^t}{\rho_i^t}; \left(\frac{P}{\rho}\right)_{i,in}^t = \frac{P_{i-1/2}^t}{\rho_{i-1}^t}$$

$$\Delta PA_v = \dot{m} \left( \left(\frac{P}{\rho}\right)_{i,out}^t + \left(\frac{P}{\rho}\right)_{i,in}^t \right)^t$$

if  $\dot{m} < 0$ ;

$$\left(\frac{P}{\rho}\right)_{i,out}^t = \frac{P_{i-1/2}^t}{\rho_{h,i}^t}; \left(\frac{P}{\rho}\right)_{i,in}^t = \frac{P_{i+1/2}^t}{\rho_{i+1}^t}$$

$$(-\Delta PA_v)_i^t = \dot{m} * abs \left( \left(\frac{P}{\rho}\right)_{i,out}^t + \left(\frac{P}{\rho}\right)_{i,in}^t \right)^t$$

Calculate the change in internal energy due to convective internal energy

For  $i = 0$  to  $N_{tot}$

$$\text{if } \dot{m} \geq 0; \Delta \dot{m} u_i^t = \dot{m} * u_{i-1}^t - \dot{m} * u_i^t$$

$$\text{if } \dot{m} < 0; \Delta \dot{m} u_i^t = \dot{m} * u_{i+1}^t - \dot{m} * u_i^t$$

Calculate the irreversible work,  $\tau A_z v$

For  $i = 0$  to  $N_{tot}$

$$\text{if } (x_i \leq 0); \mu_i^t = f(T_i^t)$$

$$\text{if } (x_i > 0 \ \&\& \ x_i < 1); \mu_{l,i}^t = f(T_i^t); \mu_{v,i}^t = f(T_i^t); \rho_{v,i}^t = f(P_i^t); \rho_{l,i}^t = f(P_i^t)$$

$$\mu_i^t = \frac{1}{\frac{x_i^t}{\mu_{v,i}^t} + \frac{1-x_i^t}{\mu_{l,i}^t}}$$

$$\varphi_{lo,i}^2 = f(X)$$

$$R_e = \frac{abs(\dot{m})}{A_x} \frac{D_1}{\mu_i^t}$$

$$\text{if } (R_e \leq 1); C_f = 16$$

$$\text{if } (R_e > 1 \ \&\& \ R_e \leq 1181) ; C_f = \frac{16}{R_e}$$

$$\text{if } (R_e > 1181) ; C_f = 0.078 R_e^{-0.25}$$

$$\tau_{l0,i}^t = 0.5 C_f \rho_i \frac{v^2}{2}$$

$$v_i^t = \left( \frac{\dot{m}}{\rho A_x} \right)_i^t$$

$$\varphi_{l0,i}^2 = f(X)$$

$$\wp_i = \pi D1 L_i$$

$$F_i^t = \tau_{l0,i}^t \wp_i \varphi_{l0,i}^2 (\Delta L + \Delta L_{eq})$$

$$(Fv)_i^t = F_i^t v_i^t$$

Calculate sum of thermal energies

For  $i = 0$  to  $N_{tot}$

$$\Sigma \dot{E}_i^t = (-\Delta \dot{m} u)_i^t + \Sigma \dot{Q}_i^t + (-\Delta P A v)_i^t + (Fv)_i^t$$

Calculate the new specific internal energies

For  $i = 0$  to  $N_{tot}$

$$u_i^{t+\Delta t} = [(mu)_i^t + \Delta t \Sigma \dot{E}_i^t] / m_i^{t+\Delta t}$$

Set boundaries

$$u_0^{t+\Delta t} = u_{N_{tot}}^{t+\Delta t}$$

$$u_{N_{tot}+1}^{t+\Delta t} = u_1^{t+\Delta t}$$

**Step 6** Calculating the new temperatures and new densities

For  $i = 0$  to  $N_{tot}$

$$u_{i,f}^{t+\Delta t} = f(P_i^{t+\Delta t}) ; u_{i,g}^{t+\Delta t} = f(P_i^{t+\Delta t}) ; \rho_{f,i}^{t+\Delta t} = f(P_i^{t+\Delta t}) ; \rho_{g,i}^{t+\Delta t} = f(P_i^{t+\Delta t})$$

$$\text{if } (u_i^{t+\Delta t} < u_{i,f}^{t+\Delta t})$$



$$T_i^{t+\Delta t} = f(u_i^{t+\Delta t}, P_i^{t+\Delta t})$$

$$\rho_i^{t+\Delta t} = f(u_i^{t+\Delta t}, P_i^{t+\Delta t})$$

$$\varphi_{lo,i}^2 = 1; x_i^{t+\Delta t} = 0; \alpha_i^{t+\Delta t} = 0$$

$$m_i^{t+\Delta t} = \rho_i^{t+\Delta t} L_i A_x$$

$$if (u_i^{t+\Delta t} > u_{i,f}^{t+\Delta t})$$

$$\mu_{l,i}^{t+\Delta t} = f(T_i^{t+\Delta t}); \mu_{v,i}^{t+\Delta t} = f(T_i^{t+\Delta t});$$

$$x_i^{t+\Delta t} = (u_i^{t+\Delta t} - u_{i,f}^{t+\Delta t}) / (u_{i,g}^{t+\Delta t} - u_{i,f}^{t+\Delta t})$$

$$T_i^{t+\Delta t} = f(P_{sat,i}^{t+\Delta t})$$

$$Mart = \left(\frac{u_g}{u_f}\right)_i^{t+\Delta t} \left(\frac{\mu_l}{\mu_v}\right)_i^{t+\Delta t} \left(\frac{(1-x_i^{t+\Delta t})}{x_i^{t+\Delta t}}\right)$$

$$\alpha_i^{t+\Delta t} = (1 + 0.28 Mart^{0.71})^{-1}$$

$$F = x^{0.78} (1 - x)^{0.224}$$

$$R_f = \frac{abs(\dot{m})(1-x)}{A_x} \frac{D_1}{\mu_i^t}$$

$$if (R_f \leq 1); C_{flo} = 16$$

$$if (R_f > 1 \ \&\& \ R_f \leq 1181); C_{flo} = \frac{16}{R_f}$$

$$if (R_f > 1181); C_{flo} = 0.078 R_f^{-0.25}$$

$$R_g = \frac{abs(\dot{m})x}{A_x} \frac{D_1}{\mu_i^t}$$

$$if (R_g \leq 1); C_{fgo} = 16$$

$$if (R_g > 1 \ \&\& \ R_g \leq 1181); C_{fgo} = \frac{16}{R_e}$$

$$if (R_g > 1181); C_{fgo} = 0.078 R_e^{-0.25}$$

$$H = \left(\frac{\rho_l}{\rho_g}\right)^{0.91} \left(\frac{\mu_g}{\mu_l}\right)^{0.9} \left(1 - \frac{\mu_g}{\mu_l}\right)^{0.7}$$

$$E = (1 - x)^2 + x^2 \frac{\rho_l C_{fgo}}{g C_{flo}}$$

$$\phi_{lo}^2 = E + \frac{3.24 F H}{Fr^{0.045} We^{0.035}}$$

$$\rho_i^{t+\Delta t} = \alpha_i^{t+\Delta t} * \rho_{g,i}^{t+\Delta t} + (1 - \alpha_i^{t+\Delta t}) * \rho_{f,i}^{t+\Delta t}$$

$$m_i^{t+\Delta t} = \rho_i^{t+\Delta t} * L_i * A_x$$

Set boundary control regions

$$T_0^{t+\Delta t} = T_{N_{tot}}^{t+\Delta t} ; T_{N_{tot}+1}^{t+\Delta t} = T_1^{t+\Delta t}$$

$$\rho_0^{t+\Delta t} = \rho_{N_{tot}}^{t+\Delta t} ; \rho_{N_{tot}+1}^{t+\Delta t} = \rho_1^{t+\Delta t}$$

$$m_0^{t+\Delta t} = m_{N_{tot}}^{t+\Delta t} ; m_{N_{tot}+1}^{t+\Delta t} = m_1^{t+\Delta t}$$

$$x_0^{t+\Delta t} = x_{N_{tot}}^{t+\Delta t} ; x_{N_{tot}+1}^{t+\Delta t} = x_1^{t+\Delta t}$$

$$\rho_0^{t+\Delta t} = \rho_{N_{tot}}^{t+\Delta t} ; \rho_{N_{tot}+1}^{t+\Delta t} = \rho_1^{t+\Delta t}$$

$$\alpha_0^{t+\Delta t} = \alpha_{N_{tot}}^{t+\Delta t} ; \alpha_{N_{tot}+1}^{t+\Delta t} = \alpha_1^{t+\Delta t}$$

**Step 7** Calculate the new mass flow rate ( $\dot{m}^{t+\Delta t}$ )

Determine the momentum term  $MM_i^t$

For  $i = 0$  to  $N_{tot}$

if ( $x_i^t \leq 0$  &&  $\alpha_i^t \leq 0$  or  $x_i^t \geq 1$  &&  $\alpha_i^t \geq 1$ )

$$MM_i^t = \frac{(m_i^t)}{\rho_i^t A_x^2}$$

if ( $x_i^t \leq 0$  &&  $\alpha_i^t \leq 0$  or  $x_i^t \geq 1$  &&  $\alpha_i^t \geq 1$ )

$$MM_i^t = \frac{(m_i^t)}{\rho_i^t A_x} \left( \frac{x^2}{\alpha \rho_g} \frac{(1-x)^2}{(1-\alpha) \rho_l} \right)_i^t$$

$$\Sigma MM^t = \Sigma MM^t + MM_i^t$$

Determine the momentum term for the next time step  $MM_i^{t+\Delta t}$

For  $i = 0$  to  $N_{tot}$

if ( $x_i^{t+\Delta t} \leq 0$  and  $\alpha_i^{t+\Delta t} \leq 0$  or  $x_i^{t+\Delta t} \geq 1$  and  $\alpha_i^{t+\Delta t} \geq 1$ )

$$MM_i^{t+\Delta t} = \frac{(m_i^{t+\Delta t})}{\rho_i^{t+\Delta t} A_x^2}$$

if ( $x_i^{t+\Delta t} \leq 0$  and  $\alpha_i^{t+\Delta t} \leq 0$  or  $x_i^{t+\Delta t} \geq 1$  and  $\alpha_i^{t+\Delta t} \geq 1$ )

$$MM_i^{t+\Delta t} = \frac{(m_i^{t+\Delta t})}{\rho_i^{t+\Delta t} A_x} \left( \frac{x^2}{\alpha \rho_g} \frac{(1-x)^2}{(1-\alpha) \rho_l} \right)_i^{t+\Delta t}$$

$$\Sigma MM^{t+\Delta t} = \Sigma MM^{t+\Delta t} + MM_i^{t+\Delta t}$$

Calculate the sum of the momentum flux terms  $MF_i^t$

For  $i = 0$  to  $N_{tot}$

if ( $x_i^t \leq 0$  and  $\alpha_i^t \leq 0$  or  $x_i^t \geq 1$  and  $\alpha_i^t \geq 1$ )

if  $\dot{m} \geq 0$

$$MF_i^t = \frac{1}{A_x} \left( \frac{1}{A_x \rho_{i-1}^t} - \frac{1}{A_x \rho_i^t} \right)$$

if  $\dot{m} < 0$

$$MF_i^t = \frac{1}{A_x} \left( \frac{1}{A_x \rho_{i+1}^t} - \frac{1}{A_x \rho_i^t} \right)$$

if ( $x_i^t \leq 0$  and  $\alpha_i^t \leq 0$  or  $x_i^t \geq 1$  and  $\alpha_i^t \geq 1$ )

if  $\dot{m} \geq 0$

$$MF_i^t = \frac{1}{A_x} \left[ \left( \frac{x^2}{\alpha \rho_g A_x} \frac{(1-x)^2}{(1-\alpha) \rho_l A_x} \right)_{i-1}^t - \left( \frac{x^2}{\alpha \rho_g A_x} \frac{(1-x)^2}{(1-\alpha) \rho_l A_x} \right)_i^t \right]$$

if  $\dot{m} < 0$

$$MF_i^t = \frac{1}{A_x} \left[ \left( \frac{x^2}{\alpha \rho_g A_x} \frac{(1-x)^2}{(1-\alpha) \rho_l A_x} \right)_{i+1}^t - \left( \frac{x^2}{\alpha \rho_g A_x} \frac{(1-x)^2}{(1-\alpha) \rho_l A_x} \right)_i^t \right]$$

$$\Sigma MF = \Sigma MF + MF_i^t$$

Calculate the sum of the gravity terms  $\Sigma G^t$

$$G_i^t = \rho_i^t L_i g \sin(\theta_i)$$

$$\Sigma G = \Sigma G + G_i^t$$

Calculate the sum of the friction terms  $\Sigma F^t$

For  $i = 0$  to  $N_{tot}$

$$\mu_{l,i}^t = f(T_i^t); \mu_{v,i}^t = f(T_i^t);$$

$$\mu_i^t = \frac{1}{\frac{x_i^t}{\mu_{v,i}^t} + \frac{1-x_i^t}{\mu_{l,i}^t}}$$

$$R_e = v_i \frac{D_1}{\mu_i^t}$$

$$R_e = \frac{abs(\dot{m})}{A_x} \frac{D_1}{\mu_i^t}$$

$$if (R_e \leq 1); C_f = 16$$

$$if (R_e > 1 \text{ and } R_e \leq 1181); C_f = \frac{16}{R_e}$$

$$if (R_e > 1181); C_f = 0.078 R_e^{-0.25}$$

$$\tau_{lo,i}^t = 0.5 C_f \rho_i \frac{v^2}{2}$$

$$v_i^t = \left( \frac{\dot{m}}{\rho A_x} \right)_i^t$$

$$\varphi_{lo,i}^2 = f(X)$$

$$if (x_i^{t+\Delta t} \leq 0 \text{ and } \alpha_i^{t+\Delta t} \leq 0); \varphi_{lo,i}^2 = 1;$$

$$else \varphi_{lo,i}^2 = \varphi_{Friedel,i}^2$$

$$\wp_i = \pi D_1 L_i$$

$$F_i^t = \tau_{lo,i}^t \wp_i \varphi_{lo,i}^2$$

$$\Sigma F = \Sigma F + F_i^t$$

Calculate the new mass flow rate

$$\dot{m}^{t+\Delta t} = \dot{m}^t \frac{\Sigma MM^t}{\Sigma MM^{t+\Delta t}} + \frac{\Delta t(\dot{m}^2 \Sigma MF + \Sigma G - \Sigma F)}{\Sigma MM^{t+\Delta t}}$$

**Step 8** Calculate the new pressure

For  $i = N_1 + N_2 + 1$  to  $N_{tot}$

$$\Sigma \rho = \Sigma \rho + \rho_i^{t+\Delta t}$$

$$P_{out, N_1 + N_2 + 1}^{t+\Delta t} = P_{atm} + (L_{expansion} 998 g) - (L_{updown} \left( \frac{\Sigma \rho}{N_{tot}} \right) g)$$

For  $i = 0$  to  $N_{tot}$

Determine the momentum term  $M_i^t$

if ( $x_i^t \leq 0$  and  $\alpha_i^t \leq 0$  or  $x_i^t \geq 1$  and  $\alpha_i^t \geq 1$ )

$$M_i^t = \frac{(m_i^t \dot{m}^t)}{\rho_i^t A_x^2}$$

if ( $x_i^t \leq 0$  and  $\alpha_i^t \leq 0$  or  $x_i^t \geq 1$  and  $\alpha_i^t \geq 1$ )

$$M_i^t = \frac{(m_i^t \dot{m}^t)}{\rho_i^t A_x} * \left( \frac{x^2}{\alpha \rho_g} \frac{(1-x)^2}{(1-\alpha) \rho_l} \right)_i^t$$

Determine the momentum term for the next time step  $M_i^{t+\Delta t}$

if ( $x_i^{t+\Delta t} \leq 0$  and  $\alpha_i^{t+\Delta t} \leq 0$  or  $x_i^{t+\Delta t} \geq 1$  and  $\alpha_i^{t+\Delta t} \geq 1$ )

$$M_i^{t+\Delta t} = \frac{(m_i^{t+\Delta t} \dot{m}^{t+\Delta t})}{\rho_i^{t+\Delta t} A_x^2}$$

if ( $x_i^{t+\Delta t} \leq 0$  and  $\alpha_i^{t+\Delta t} \leq 0$  or  $x_i^{t+\Delta t} \geq 1$  and  $\alpha_i^{t+\Delta t} \geq 1$ )

$$M_i^{t+\Delta t} = \frac{(m_i^{t+\Delta t} \dot{m}^{t+\Delta t})}{\rho_i^{t+\Delta t} A_x} \left( \frac{x^2}{\alpha \rho_g} \frac{(1-x)^2}{(1-\alpha) \rho_l} \right)_i^{t+\Delta t}$$

$$\left( \frac{\Delta M_i}{\Delta t} \right)^{t+\Delta t} = (M_i^{t+\Delta t} - M_i^t) / \Delta t$$

Calculate the sum of the momentum flux terms  $MF_i^t$

if  $(x_i^{t+\Delta t} \leq 0 \text{ and } \alpha_i^{t+\Delta t} \leq 0 \text{ or } x_i^{t+\Delta t} \geq 1 \text{ and } \alpha_i^{t+\Delta t} \geq 1)$

if  $\dot{m} \geq 0$

$$MF_i^{t+\Delta t} = \frac{(\dot{m}^{t+\Delta t})^2}{A_x} * \left( \frac{1}{A_x \rho_{i-1}^{t+\Delta t}} - \frac{1}{A_x \rho_i^{t+\Delta t}} \right)$$

if  $\dot{m} < 0$

$$MF_i^{t+\Delta t} = \frac{(\dot{m}^{t+\Delta t})^2}{A_x} \left( \frac{1}{A_x \rho_{i+1}^{t+\Delta t}} - \frac{1}{A_x \rho_i^{t+\Delta t}} \right)$$

if  $(x_i^{t+\Delta t} \leq 0 \text{ and } \alpha_i^{t+\Delta t} \leq 0 \text{ or } x_i^{t+\Delta t} \geq 1 \text{ and } \alpha_i^{t+\Delta t} \geq 1)$

if  $\dot{m} \geq 0$

$$MF_i^{t+\Delta t} = \frac{(\dot{m}^{t+\Delta t})^2}{A_x} \left[ \left( \frac{x^2}{\alpha \rho_g A_x} * \frac{(1-x)^2}{(1-\alpha) \rho_l A_x} \right)_{i-1}^t - \left( \frac{x^2}{\alpha \rho_g A_x} * \frac{(1-x)^2}{(1-\alpha) \rho_l A_x} \right)_i^t \right]$$

if  $\dot{m} < 0$

$$MF_i^{t+\Delta t} = \frac{(\dot{m}^{t+\Delta t})^2}{A_x} \left[ \left( \frac{x^2}{\alpha \rho_g A_x} * \frac{(1-x)^2}{(1-\alpha) \rho_l A_x} \right)_{i+1}^t - \left( \frac{x^2}{\alpha \rho_g A_x} * \frac{(1-x)^2}{(1-\alpha) \rho_l A_x} \right)_i^t \right]$$

Calculate the gravity terms  $G^t$

$$G_i^{t+\Delta t} = \rho_i^{t+\Delta t} L_i g \sin(\theta_i)$$

Calculate the friction terms  $F^t$

$$\mu_{l,i}^{t+\Delta t} = f(T_i^{t+\Delta t}); \mu_{v,i}^{t+\Delta t} = f(T_i^{t+\Delta t});$$

$$\mu_i^{t+\Delta t} = \frac{1}{\frac{x_i^{t+\Delta t}}{\mu_{v,i}^{t+\Delta t}} + \frac{1-x_i^{t+\Delta t}}{\mu_{l,i}^{t+\Delta t}}}$$

$$R_e = v_i \frac{D_1}{\mu_i^{t+\Delta t}}$$

$$R_e = \frac{abs(\dot{m})}{A_x} \frac{D_1}{\mu_i^{t+\Delta t}}$$

if  $(R_e \leq 1); C_f = 16$

if  $(R_e > 1 \text{ and } R_e \leq 1181); C_f = \frac{16}{R_e}$

$$\text{if } (R_e > 1181); C_f = 0.078 R_e^{-0.25}$$

$$\tau_{lo,i}^{t+\Delta t} = 0.5 C_f \rho_i \frac{v^2}{2}$$

$$v_i^{t+\Delta t} = \left( \frac{\dot{m}}{\rho * A_x} \right)_i^{t+\Delta t}$$

$$\varphi_{lo,i}^2 = f(X)$$

$$\text{if } (x_i^{t+\Delta t} \leq 0 \text{ and } \alpha_i^{t+\Delta t} \leq 0); \varphi_{lo,i}^2 = 1;$$

$$\text{else } \varphi_{lo,i}^2 = \varphi_{Friedel,i}^2$$

$$\wp_i = \pi D1 L_i$$

$$F_i^{t+\Delta t} = \tau_{lo,i}^{t+\Delta t} * \wp_i * \varphi_{lo,i}^2$$

**Step 9** Calculate the new pressure

$$P_{in,i}^{t+\Delta t} = P_{out,i-1}^{t+\Delta t}$$

$$P_{out,i-1}^{t+\Delta t} = P_{in,i}^{t+\Delta t} + MF_i^{t+\Delta t} + G_i^{t+\Delta t} + \left( \frac{\Delta M_i}{\Delta t} \right)^{t+\Delta t} + M_i^{t+\Delta t}$$

$$P_i^{t+\Delta t} = (P_{in,i}^{t+\Delta t} + P_{out,i}^{t+\Delta t})/2$$

Do the same for elements 1 to N1+N2

Set old values to new values

$$\dot{m}^t = \dot{m}^{t+\Delta t}$$

For  $i = 0$  to  $N_{tot}$

$$\left( \frac{\Delta m}{\Delta t} \right)_i^{t-\frac{\Delta t}{2}} = (m_i^{t+\Delta t} - m_i^t)/\Delta t; \left( \frac{\Delta P}{\Delta t} \right)_i^{t-\frac{\Delta t}{2}} = (P_i^{t+\Delta t} - P_i^t)/\Delta t$$

$$\left( \frac{\Delta m}{\Delta t} \right)_i^t = \left( \frac{\Delta m}{\Delta t} \right)_i^{t+\Delta t}; \left( \frac{\Delta P}{\Delta t} \right)_i^t = \left( \frac{\Delta P}{\Delta t} \right)_i^{t+\Delta t}$$

$$m_i^t = m_i^{t+\Delta t}; P_i^t = P_i^{t+\Delta t}; T_i^t = T_i^{t+\Delta t}; u_i^t = u_i^{t+\Delta t}; x_i^t = x_i^{t+\Delta t}$$

$$\alpha_i^t = \alpha_i^{t+\Delta t}; \varphi_i^t = \varphi_i^{t+\Delta t};$$

Set boundary conditions

$$T_0^t = T_{N_{tot}}^t ; T_{N_{tot}+1}^t = T_1^t ; m_0^t = m_{N_{tot}}^t ; m_{N_{tot}+1}^t = m_1^t$$

$$u_0^t = u_{N_{tot}}^t ; u_{N_{tot}+1}^t = u_1^t ; \rho_0^t = \rho_{N_{tot}}^t ; \rho_{N_{tot}+1}^t = \rho_1^t$$

$$P_0^t = P_{N_{tot}}^t ; P_{N_{tot}+1}^t = P_1^t ; \alpha_0^t = \alpha_{N_{tot}}^t ; \alpha_{N_{tot}+1}^t = \alpha_1^t$$

$$x_0^t = x_{N_{tot}}^t ; x_{N_{tot}+1}^t = x_1^t$$

Add time step

$$t = t + \Delta t$$

Return to top of time loop



## APPENDIX C PROPERTY FUNCTIONS

### C.1 Properties of water

In this appendix the functions, described in Section 3.8 which determine the properties of the system is shown. The properties were taken from the NIST (National institute of standards and technology) (“NIST Chemistry WebBook”, 2017).

Table C-1 Saturated liquid specific internal energy  $u_f$  as a function of pressure

$u_f = c_0 + c_1P + c_2P^2 + c_3P^3 + c_4P^4 + c_5P^5 + c_6P^6$ $u_f$ in kJ/kg if $P$ in kPa			
	$0.061 < P < 16.53$	$16.53 \leq P \leq 327.11$	$327.11 < P \leq 4111.97$
$C_0$	-51.1226157751	1.4888334489E+02	4.0035471901E+02
$c_1$	102.0209601818	6.4979242988E+00	6.7778941222E-01
$c_2$	-27.1553689066	-7.7624453465E-02	-5.2019150283E-04
$c_3$	4.4293810645	6.1112412441E-04	2.7672986193E-07
$c_4$	-0.3975462815	-2.7501304017E-06	-8.5602736175E-11
$c_5$	0.0181153216	6.4396072696E-09	1.3928091928E-14
$c_6$	-0.0003266039	-6.0693721631E-12	-9.1901529276E-19

Table C-2 Saturated vapour specific internal energy  $u_g$  as a function of pressure

$u_g = c_0 + c_1P + c_2P^2 + c_3P^3 + c_4P^4 + c_5P^5 + c_6P^6$ $u_g$ in kJ/kg if $P$ in kPa			
	$0.061 < P < 16.53$	$16.53 \leq P \leq 327.11$	$327.11 < P \leq 4111.97$
$C_0$	2358.1579797960	2.4238762160E+03	2504.272669486530000
$c_1$	33.4363477297	2.0507191192E+00	0.1717752935832960000
$c_2$	-8.9147174687	-2.5178821003E-02	-0.0001545079243937680
$c_3$	1.4531404289	1.9878593852E-04	0.0000000834158796614
$c_4$	-0.1303615077	-8.9552920133E-07	-0.0000000000259833654
$c_5$	0.0059384234	2.0981323578E-09	0.0000000000000042435
$c_6$	-0.0001070414	-1.9781867354E-12	-0.0000000000000000003

Table C-3 Saturated liquid density  $\rho_l$  as a function of pressure in kJ/kg if  $P$  in kPa

$u_g = c_0 + c_1P + c_2P^2 + c_3P^3 + c_4P^4 + c_5P^5 + c_6P^6$			
	$0.061 < P < 16.53$	$16.53 \leq P \leq 327.11$	$327.11 < P \leq 4111.97$
$C_0$	9.99893091469801E+02	9.9573725184E+02	9.6431660562E+02
$C_1$	5.73089169256146E-01	-7.6649913333E-01	-1.3293419551E-01
$C_2$	-8.9192358508238E-01	7.7224135921E-03	9.0360672724E-05
$C_3$	1.85319663788385E-01	-5.7607084723E-05	-4.6856353600E-08
$C_4$	-1.8373199542337E-02	2.5249707260E-07	1.4315526259E-11
$C_5$	8.8305245982667E-04	-5.8223899919E-10	-2.3127440662E-15
$C_6$	-1.644869240637E-05	5.43359458E-13	1.5190539152E-19

Table C-4 Saturated vapour density  $\rho_g$  as a function of pressure in kJ/kg if P in kPa

$u_g = c_0 + c_1P + c_2P^2 + c_3P^3 + c_4P^4 + c_5P^5 + c_6P^6$			
	0.061 < P < 16.53	16.53 ≤ P ≤ 327.11	327.11 < P ≤ 4111.97
C <sub>0</sub>	2.2183085408E-04	5.4216949984E-03	8.1129440366E-02
c <sub>1</sub>	7.7188137948E-03	6.4552112843E-03	5.3652735901E-03
c <sub>2</sub>	-2.3245501562E-04	-1.0499043787E-05	-4.9826774425E-07
c <sub>3</sub>	2.9313067648E-05	6.5772099409E-08	2.6108651358E-10
c <sub>4</sub>	-2.3815594809E-06	-2.6882739944E-10	-7.4331020380E-14
c <sub>5</sub>	1.0306206287E-07	5.9825430312E-13	1.1623116070E-17
c <sub>6</sub>	-1.8014005626E-09	-5.4665770412E-16	-7.4771886893E-22

Table C-5 Saturated temperature T<sub>sat</sub> as a function of pressure in kJ/kg if P in kPa

$\rho_g = c_0 + c_1P + c_2P^2 + c_3P^3 + c_4P^4 + c_5P^5 + c_6P^6$			
	0.061 < P < 16.53	16.53 ≤ P ≤ 327.11	327.11 < P ≤ 4111.97
c <sub>0</sub>	-1.2133791931E+01	3.5544956965E+01	9.5805436011E+01
c <sub>1</sub>	2.4219031307E+01	1.5549111048E+00	+1.5957346907E-01
c <sub>2</sub>	-6.422865726E+00	-1.861195782E-02	-1.240818488E-04
c <sub>3</sub>	1.0458389499E+00	1.4653434721E-04	6.6048247052E-08
c <sub>4</sub>	-9.3775141201E-02	-6.5940867344E-07	-2.0438957188E-11
c <sub>5</sub>	4.2705211636E-03	1.5440147291E-09	3.3262325892E-15
c <sub>6</sub>	-7.6962116033E-05	-1.4552189188E-12	-2.1950298662E-19

Table C-6 Subcooled liquid density  $\rho$  as a function of specific internal energy and pressure in kg/m<sup>3</sup> if u in kJ/kg and P in kPa

$\rho_g = c_0 + c_1u + c_2P + c_3u^2 + c_4uP + c_5P^2 + c_6u^3 + c_7u^2P + c_8uP^2 + c_9P^3 + c_{10}u^4 + c_{11}u^3P + c_{12}u^2P^2 + c_{13}uP^3 + c_{14}P^4$					
0.061 < P < 4111.97 kPa and 29.43 < u < 1090.27 kJ/kg					
C <sub>0</sub>	1000.779719	c <sub>6</sub>	2.07712E-07	C <sub>12</sub>	-1.33563E-08
c <sub>1</sub>	-0.007880504	c <sub>7</sub>	9.55791E-07	C <sub>13</sub>	-1.55635E-06
c <sub>2</sub>	0.501061297	c <sub>8</sub>	1.99151E-05	C <sub>14</sub>	0.000295794
c <sub>3</sub>	-0.000294956	C <sub>9</sub>	-0.001472865		
c <sub>4</sub>	-0.000567902	C <sub>10</sub>	-8.58722E-11		
c <sub>5</sub>	-0.001389033	C <sub>11</sub>	-2.49935E-10		

Table C-7 Subcooled liquid temperature T as a function of specific internal energy and pressure in °C if u in kJ/kg and P in kPa

$\rho_g = c_0 + c_1u + c_2P + c_3u^2 + c_4uP + c_5P^2 + c_6u^3 + c_7u^2P + c_8uP^2 + c_9P^3 + c_{10}u^4$ $+ c_{11}u^3P + c_{12}u^2P^2 + c_{13}uP^3 + c_{14}P^4$ $0.061 < P < 4111.97 \text{ kPa and } 29.43 < u < 1090.27 \text{ kJ/kg}$			
C <sub>0</sub>	-0.070309218	c <sub>8</sub>	-3.21245E-06
c <sub>1</sub>	0.239100268	C <sub>9</sub>	-0.000603376
c <sub>2</sub>	-0.00359348	C <sub>10</sub>	-5.59257E-12
c <sub>3</sub>	1.23848E-06	C <sub>11</sub>	1.57677E-10
c <sub>4</sub>	0.000203382	C <sub>12</sub>	1.81883E-09
c <sub>5</sub>	0.0021858	C <sub>13</sub>	2.76191E-07
c <sub>6</sub>	-2.44212E-09	C <sub>14</sub>	5.39087E-05
c <sub>7</sub>	-1.39232E-07		

Table C-8 Superheated vapour temperature T as a function of specific internal energy and pressure in °C if u in kJ/kg and P in kPa

$T = c_1 + c_2u + c_3u^2 + c_4P + c_4P^2 + c_5P^2 + c_6uP + c_7u^2P + c_8uP^2 + c_9u^2P^2$ $T \text{ a}$ $0.061 < P < 4111.97 \text{ kPa and } 29.43 < u < 1090.27 \text{ kJ/kg}$			
c <sub>1</sub>	0.006536332	c <sub>6</sub>	-6.55818E-16
c <sub>2</sub>	-1.03322E-05	c <sub>7</sub>	7.40924E-19
c <sub>3</sub>	5.27676E-08	c <sub>8</sub>	-6.09745E-22
c <sub>4</sub>	-1.80680E-10	C <sub>9</sub>	3.70293E-25
c <sub>5</sub>	4.13859E-13		

Table C-9 Saturated liquid viscosity  $\mu_l$  as a function of temperature in kg/ms if T in °C

$\mu_l = c_0 + c_1T + c_2T^2 + c_3T^3 + c_4T^4 + c_5T^5 + c_6T^6$	
c <sub>0</sub>	1.7699E-03
c <sub>1</sub>	-5.2826E-05
c <sub>2</sub>	9.0025E-07
c <sub>3</sub>	- 8.8006E-09
c <sub>4</sub>	4.7856E-11
c <sub>5</sub>	- 1.3362E-13
c <sub>6</sub>	1.4878E-16

Table C-10 Saturated vapour viscosity  $\mu_v$  as a function of temperature in kg/ms if T in °C

$\mu_v = c_0 + c_1T + c_2T^2 + c_3T^3 + c_4T^4 + c_5T^5 + c_6T^6$	
$c_0$	9.2183123915E-06
$c_1$	2.3420814222E-08
$c_2$	1.1703011893E-10
$c_3$	-6.1522826231E-13
$c_4$	1.9412394723E-15
$c_5$	-4.7712670093E-18
$c_6$	7.3541121302E-21

Table C-11 Liquid-vapour surface tension for water, SIGMA in N/m if T in C

$\sigma = c_0 + c_1T + c_2T^2$	
$c_0$	7.573636E-02
$c_1$	-1.458939E-04
$c_2$	-2.234848E-07

## C.2 Properties of stainless

The values for the thermal conductivity, density, specific heat and emissivity of stainless steel was found in textbook of (Mills & Ganesan, 2015).

$$\rho = 7900 \text{ kg/m}^3; c = 480 \text{ J/kg K}; \varepsilon = 0.3 \quad k = 14 \text{ W/m K}$$

## C.3 Properties of Nickel-chrome heating element

The values for the thermal conductivity, density and specific heat of nickel-chrome was found in textbook of (Mills & Ganesan, 2015).

$$\rho = 8314 \text{ kg/m}^3; c = 460 \text{ J/kg K}; k = 13 \text{ W/m K}$$

## C.4 Properties of insulation material

The values for the thermal conductivity, density and specific heat of nickel-chrome was found in textbook of (Mills & Ganesan, 2015).

$$c = 835 \text{ J/kg K}; k = 0.064 \text{ W/m K}$$

## APPENDIX D CALIBRATIONS

In this section the calibrations of the measurement instruments and sensor is given. The calibration were done to ensure that the instruments measure accurately which increases the validity of the experiments. The calibration for the pressure transducers, thermocouples and orifice plate are shown. The calibration indicated that the instruments and sensors are within an accuracy of 0 to 2 % .

### Pressure transducers

The 4 bar Endress-Hauser Cerabar S PMC71 pressure transducer (Serial: L600862109D) and the 500 mbar Endress-Hauser Deltabar S PMD75 differential pressure transducer (Serial: L600562109D) were calibrated against a Wike Master Gauge (Serial MEG-NO-01 and MEG-NO-02) and the calibrated values can be seen in table D1 and D2. The current vs pressure shows a linear correlation. The error was calculated using the equation D.1, where the calibrated pressure is the pressure from the master gauge.

$$error\% = \frac{|P_{calibrated} - P_{transducer}|}{|P_{calibrated}|} * 100 \quad (D.1)$$

Table D-1 Differential pressure transducer calibration

Master pressure(mBar)	Current (mA)	Transducer (mBar)	% Error
500	19.91	493.0	1.40
450	19.09	442.8	1.60
400	18.29	393.3	1.68
350	17.55	346.5	1.00
300	16.73	296.2	1.27
250	15.99	249.0	0.40
200	15.18	199.2	0.40
150	14.39	148.7	0.87
100	13.66	102.2	2.20
50	12.84	52.00	4.00
0	12.01	0	0
-50	11.17	-51.20	2.40
-100	10.36	-101.5	1.50
-150	9.62	-149.0	0.67
-200	8.83	-198.6	0.70
-250	8.04	-247.0	1.20
-300	7.29	-295.0	1.67
-350	6.48	-345.9	1.17
-400	5.69	-394.0	1.50
-450	4.89	-444.2	1.29
-500	4.07	-495.2	0.96

Table D-2 Static pressure transducer calibration

Master gauge(Bar)	Current (mA)	Transducer (Bar)	%Error
4.0	20.02	4.006	0.15
3.5	18.02	3.51	0.29
3.0	16.02	3.004	0.13
2.5	13.97	2.501	0.04
2.0	12.06	2.017	0.85
1.5	10.03	1.505	0.33
1.0	8.06	1.011	1.1
0.5	6.05	0.507	1.4
0.0	0	0	0

### Orifice plate

The orifice plate was calibrated in place in the experimental assembly. The orifice has  $\beta = 0.315$  with pressure tappings at one inch to either side of the plate. The flow rate was measured with a bucket, stop watch and a 30 kg NA-GATA scale with 0.02 kg measurement increments. The pressure difference across the plate was measured with the Endress-Hauser DeltabarS differential pressure transducer measuring 0-500 mbar pressure differences in both the clockwise and anti-clockwise directions. Fifth order logarithmic functions were plotted to the data points for both the clockwise and anti-clockwise directions, see equations D.2 and (D.3).

$$-60 \text{ mBar} < \text{Differential Pressure } (x) < -0.355 \text{ mbar}$$

$$\dot{m} = a + b \ln(-x) + c * \ln(-x)^2 + d * \ln(-x)^3 + e * \ln(-x)^4 + f * \ln(-x)^5 \quad (\text{D.2})$$

with

$$\begin{aligned} a &= -4.56518007008564\text{E-}02 & b &= -3.40589407485589\text{E-}02 \\ c &= -8.00007487813076\text{E-}03 & d &= 3.56993010206643\text{E-}03 \\ e &= -8.08098015137113\text{E-}04 & f &= -3.22666940928165\text{E-}05 \end{aligned}$$

and  $R^2 = 0.993$

$$-0.335 \text{ mBar} < \text{Differential Pressure } (x) < 0.355 \text{ mbar}$$

$$\dot{m} = 0 \text{ kg/s}$$

$$60\text{mBa} > \text{Differential Pressure } (x) > 0.355 \text{ mbar}$$

$$\dot{m} = a + b \ln(x) + c * \ln(x)^2 + d * \ln(x)^3 + e * \ln(x)^4 + f * \ln(x)^5 \quad (\text{D.3})$$

with

$$a = 3.32235327210218E-02 \quad b = 2.60087533142461E-02$$

$$c = -3.74343939882368E-04 \quad d = 2.8773157061347E-03$$

$$e = -3.40693061394903E-04 \quad f = 5.80448871765527E-05$$

and  $R^2 = 0.998$

Figure D-1 shows the experimentally determined data points as well as the curve for both forward and reverse directions. Note: These equations are only valid for the indicated pressure ranges.

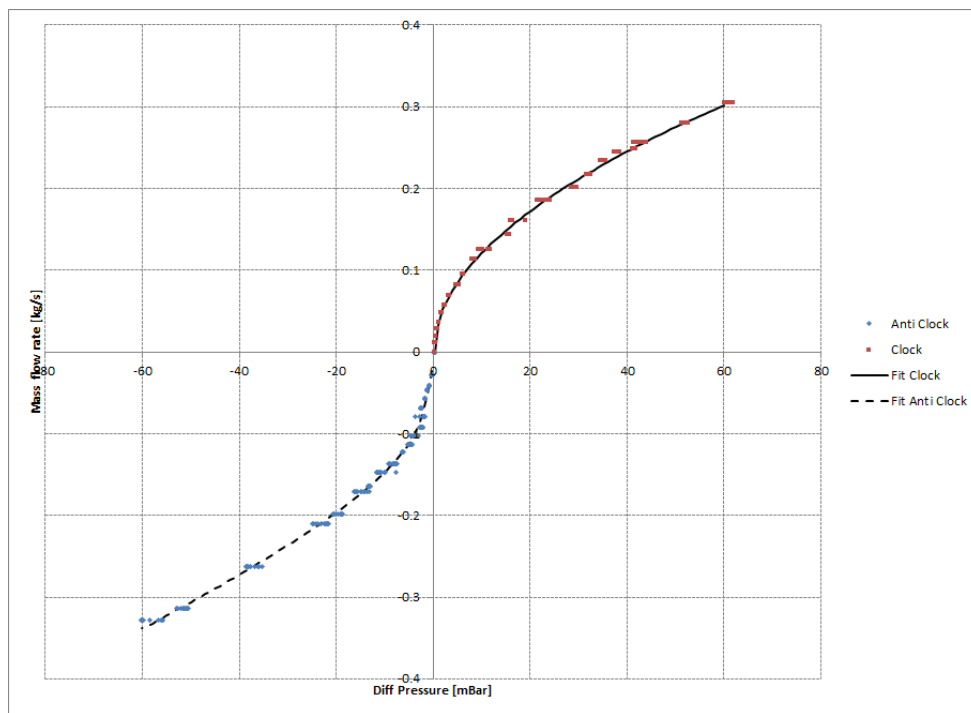


Figure D-1 Orifice plate mass flow rate as a function of the differential pressure across the orifice calibration

## Thermocouples

The four working fluid thermocouples were calibrated using a FLUKE 9142 dry well calibrator (Serial number: B29291). Equation D.1 was used to determine the error of the thermocouples at each calibration temperature, where the calibration value is the fluke value and the transducer is the thermocouple measured temperature, see Table D-3.

Table D-3 Working fluid thermocouple calibration

FLUKE (C°)	Thermocouples (C°)				Error (%)			
	TE	TC	BC	BE	TE	TC	BC	BE
10	9.75	9.99	0.95	9.9	2.5	0.1	1	0.9
20	19.58	19.70	9.9	19.54	2.105	1.49	2.3	1.365
30	29.56	29.19	19.54	29.21	1.463	2.683	2.65	1.2
40	39.42	39.66	29.21	39.36	1.4575	0.84	1.59	1.2175
50	49.48	49.53	39.36	49.61	1.042	0.94	0.784	0.656
60	59.5	59.44	49.61	59.44	0.833	0.923	0.933	0.971
70	69.57	69.54	59.44	69.514	0.615	0.647	0.694	0.981
80	79.60	79.57	69.51	79.55	0.497	0.537	0.562	0.062
90	89.63	89.59	79.55	89.604	0.411	0.45	0.44	0.237
100	99.68	99.63	89.60	99.643	0.321	0.361	0.357	0.3
110	109.71	109.70	99.64	109.7	0.263	0.270	0.277	0.3
120	119.82	119.82	109.7	119.77	0.15	0.152	0.18	0.120